UNIVERSITY OF CALIFORNIA, MERCED

Investigation of local strain, symmetry, and elastic properties of methylammonium lead iodide (MAPI) hybrid perovskite using density functional theory

A dissertation submitted in partial satisfaction of the
requirements for the degree
Doctor of Philosophy

in

Physics

by

Kuntal Talit

Committee in charge:

Professor Sayantani Ghosh, Chair
Professor Christine Isborn
Professor David A. Strubbe

2022

The dissertation of Kuntal Talit is approved, and
it is acceptable in quality and form for publication
on microfilm and electronically:

(Professor Christine Isborn)

(Professor David A. Strubbe)

(Professor Sayantani Ghosh, Chair)

University of California, Merced

2022

DEDICATION

For my father Basudeb, mother Manorama,
wife Priyanka and my little daughter Srishti,
for their continuous encouragement,
support, and love that make it possible.

EPIGRAPH

Karmanye vadhikaraste Ma Phaleshu Kadachana,
Ma Karmaphalaheturbhurma Te Sangostvakarmani
—Bhagavad Gita, 2-47.

TABLE OF CONTENTS

LIST OF FIGURES

LIST OF TABLES

ACKNOWLEDGEMENTS

I would like to thank my PhD advisor David Strubbe for his continuous encouragement, support, and guidance for last five and a half years; all my lab mates Enrique Guerrero, Rijan Karkee, Md. Mehdi Masud, Arabi Seshappan, Uday Panta, Mojdeh Banafsheh, Brad Barker, Tobias Zier, and Rafael Rodrigues Del Grande for valuable research discussions, help, and support. I would also like to thank my PhD committee members Prof. Sayantani Ghosh and Prof. Christine Isborn for their valuable comments and suggestions throughout the entire course of my PhD. I am very grateful to Prof. Ashlie Martini for accepting me as a PhD student at Martini Lab in the beginning of my PhD, without which probably, it would not have been possible for me to start my PhD. I thank the Merced nAnomaterials Center for Energy and Sensing (MACES) for proving me summer fellowships for research. I thank the supercomputing facilities at National Energy research Scientific Computing Center (NERSC) and MERCED Cluster at University of California, Merced for the computational resources.

A good encouraging support system is very important, and it motivates most during tough times in PhD. I am grateful to my parents who did not get chance to complete their schooling, but always have encouraged me to study. I am thankful to my wife Priyanka for being supportive in every way. I also thank Mr. Lenard Rhodes, uncle whom I met after reaching Merced 6 years back, for all his support, love, guidance and for showing me a different perspective of life, and considering me as a family member in his house. I thank Somnath Sinha for guiding me as an elder brother and friend during my happy and sad times in my PhD life.

I thank my previous teachers Prof. Mallar Ray, Prof. Nil Ratan Bandyopadhyay, Prof. G. P. Das, Prof. Syed Minhaz Hosssain for their constant encouragement and motivation that inspired me to pursue a PhD. I would also like to thank Manoj Saha, my physics teacher during my bachelors; who taught me not to give up, while almost all pathways seemed closed for me for doing my master's. Last but not least, I thank all my friends (too many to list here) for their unconditional love and support in critical times.

VITA

2006	B. Sc. in Physics, The University of Burdwan, India
2009	M. Sc. in Applied Physics, Indian Institute of Engineering Science and Technology, Shibpur, India
2011	M. Tech. in Materials Engineering, Indian Institute of Engineering Science and Technology, Shibpur, India
2019	M. S. in Physics, University of California, Merced
2022	Ph. D. in Physics, University of California, Merced

FELLOWSHIPS AND AWARDS

NASA-funded Merced Nanomaterials Center for Energy and Sensing (MACES) Summer Research Fellowship (2018, 2021, 2022)

Dan David Solar Fellowship, University of California, Merced (2018).

2^{nd} prize for poster competition at American Physical Society bridge program, Stanford University & Google HQ (2018).

PUBLICATIONS

Kuntal Talit and David A. Strubbe, "Stress effects on Raman spectroscopy of cubic hybrid perovskite: A probe of local strain," J. Phys. Chem. C, 124, 50, 2020

PRESENTATIONS

Kuntal Talit and David A. Strubbe, "Resolving discrepancies in mechanical properties of hybrid perovskites: a DFT study", American Physical Society March Meeting (2022), **contributed talk**

Kuntal Talit and David A. Strubbe, "Interplay of structural changes, symmetry and vibrations in orthorhombic and tetragonal hybrid perovskites under stress", Molecular Foundry User Meeting at Lawrence Berkeley National Laboratory (2021), **contributed talk**

Kuntal Talit and David A. Strubbe, "Interplay of structural changes, symmetry and vibrations in orthorhombic and tetragonal hybrid perovskites under stress", American Physical Society March Meeting (2021,online due to COVID-19), **contributed talk**

Nicholas Lopez, Kuntal Talit, and David A. Strubbe, "The effect of strain on vibrations in cubic $CsPbI_3$ perovskite", American Physical Society March Meeting (2021) **poster**

Kuntal Talit and David A. Strubbe, "Stress effects on vibrational spectra of orthorhombic and tetragonal hybrid perovskites", Molecular Foundry User Meeting at Lawrence Berkeley National Laboratory (2020), **poster**

Kuntal Talit and David A. Strubbe, "Stress effects on vibrational spectra of orthorhombic and tetragonal hybrid perovskites", Workshop in Electronic Structure Methods, University of California Merced (2020) **poster**

Kuntal Talit and David A. Strubbe, "Stress effects on vibrational spectra of orthorhombic and tetragonal hybrid perovskites", American Physical Society March Meeting (2020, cancelled due to COVID-19), **contributed talk**

Kuntal Talit and David A. Strubbe, "Raman spectroscopy as a probe of local strain in perovskite solar cells", American Physical Society March Meeting (2019), **contributed talk**

Kuntal Talit and David A. Strubbe, "Stress effects on vibrational spectra of cubic hybrid perovskite: A probe of local strain", Molecular Foundry User Meeting at Lawrence Berkeley National Laboratory (2019) **poster**

Kuntal Talit and David A. Strubbe, "Raman spectra as a probe of localized strain in perovskite solar cells", American Physical Society Bridge Program, Stanford University and Google HQ. (2018) **poster, 2^{nd} prize**

Kuntal Talit and David A. Strubbe, "Density functional theory calculations of hybrid perovskites for photovoltaics", American Physical Society Far West Section meeting (2017) **poster**

WORKSHOPS

Data Science Challenge, Lawrence Livermore National Laboratory (LLNL) 23^{rd} May - 6^{th} June 2022.

X, the moonshot factory - University of California, Merced Virtual Bootcamp: Machine Learning 19^{th} Oct. - 22^{nd}, 2020.

32^{nd} Workshop on Recent Developments in Electronic Structure Methods (virtual), University of California, Merced, 1^{st} - 4^{th} Jun. 2020.

San Diego Supercomputer Center Summer Institute: Machine Learning, visualization, git, jupyter notebook and HPC applications 3^{rd} - 7^{th} Aug. 2020.

BerkeleyGW - A Massively Parallel GW/BSE Code, Hands on training and workshop which includes lectures on theory, application and computational details of GW and Bethe-Salpeter calculation for quasiparticles and optical properties of solids, molecules and nanosystems, 10^{th} - 12^{th} Jan. 2018.

ABSTRACT OF THE DISSERTATION

Investigation of local strain, symmetry, and elastic properties of methylammonium lead iodide (MAPI) hybrid perovskite using density functional theory

by

Kuntal Talit
Doctor of Philosophy in Physics
University of California Merced, 2022
Professor Sayantani Ghosh, Chair

Hybrid organic metal-halide perovskites are promising materials for next generation solar cell application. Methylammonium lead iodide ($CH_3NH_3PbI_3$), sometimes called MAPI, is one of the favorable perovskites for making solar cells. Most of the research in the last decade about this material is aimed towards improving its photoconversion efficiency (PCE) and stability. In this work, I have done a detailed study on the three phases (orthorhombic, tetragonal, and cubic) of MAPI to understand how these different phases behave under stress. The total work is divided into 5 chapters. In chapter 1, I give an overview on perovskites for solar cell applications and discuss briefly about the theories that are involved in my calculations. In chapter 2, I investigate the effect of uniaxial strain on the pseudo-cubic structure and identify the most favorable vibrational modes to measure local strain using IR and Raman spectroscopy. In chapter 3, I investigate the same for low-temperature orthorhombic and room-temperature tetragonal phases. In addition to this, I explained about an improvement I made to the Quantum ESPRESSO code to enable these calculations. In chapter 4, I discussed how an analytical method we developed can help to understand hidden symmetries in the tetragonal perovskite and can be useful for any approximately symmetric structure to use symmetry for spectroscopic studies. In chapter 5, the last chapter, I studied the elastic properties of all three phases in detail and tried to determine the root cause behind the discrepancies in earlier published results. We also provide accurate reference values and an appropriate general methodology for elastic properties of metal halide perovskites. This work opens

a way for a standard non-destructive bench-top characterization method to be usable for analyzing the critical role of local strain in hybrid perovskite photovoltaics. It provides an analytical method to calculate irreducible representations of vibrational modes for any approximately symmetric crystal structure which can be helpful for spectroscopic studies. Calculated detailed elastic properties of metal-halide perovskite will be useful for future reference for commercial application of perovskites for solar cell and flexible electronics.

Chapter 1

Introduction

After the discovery of perovskite ($CaTiO_3$) by Lev Perovski in mid 19^{th} century, it took a lot of time to realize its importance as solar cell material. It wasn't until 2009 that Tsutoma Miyasaka first showed that it can be used as light absorber material[70]. Since then, a tremendous amount of work has been done[125] on different perovskites to improve the photo conversion efficiency of this class of materials and it improved from 3.8% to 25.7% in lab scale[97]. Due to low cost and ease of manufacturing, it attracted a great attention of the scientific and business community to commercialize it as solar cell[88]. As per a recent report from NASA, they are trying to build solar panel in space using electrospraying technique that would be possible to generate a megawatt of solar power which is more than enough to satisfy a space station's energy need with just one liter of perovskite solution[93, 87]. Apart from photo-voltaics, perovskites also have applications in flexible electronics[39, 81], light emitting diodes[139], lasers[137], spin-optoelectronic devices[148], luminescent solar concentrators[162] etc. So, the possibilities are endless, but they have some serious roadblocks. The degradation of these perovskite materials in ambient conditions makes it harder to use in commercial application. Now the focus of all the communities is to stabilize these material of a considerable time range.

1.1 Background and Motivation

The basic mechanism behind a solar cell is simple to understand. The absorption of incident photons can create electron hole pairs within the material, pro-

vided that the incident photon energy is greater than that of the bandgap. When these carriers diffuse towards the depletion region it separates the electrons and holes by the action of the electric field existing at the P-N junction. The concentration of electron and hole increase in N-type and P-type region and create a forward voltage. This mechanism is called photovoltaic effect. When a load is connected between these two terminals, electrons flow from the N-type to P-type side which generates a current in the opposite direction as shown in the schematic diagram Fig 1.1. Defects plays a major role in photovoltaic efficiency. Presence of crystal defects in semiconductors affects the recombination mechanism and lifetime of carriers by creating defects states within the bandgap. Some defect states lie near band edge, but some may also lie deep within the forbidden gap and can enable a two-step recombination process called Shockley-Read-Hall recombination. The recombination rate depends on the volume density of defects and the energy of the trapping level. This type of recombination is mainly non-radiative and can affect the photo-voltage of the solar cell and reduce it's efficiency. So, understanding of defect within the material is important[67]. Commonly used solar cell materials are silicon, which we normally see in our roof top, and III-V semiconductors (GaAs) for space applications[68]. Besides these two, we also have CdTe, CIGS, a-Si etc. as solar cell materials. III-V semiconductors are very expensive and have good photo conversion efficiency (PCE). Amorphous silicon cells are comparatively cheap, but have low PCE. Si is moderate in both cost and efficiency and hence most widely used. There are recent studies about a newly invented material, called perovskite, which can lower the cost a considerable amount, and still provide the equivalent efficiency as Si solar cells does.

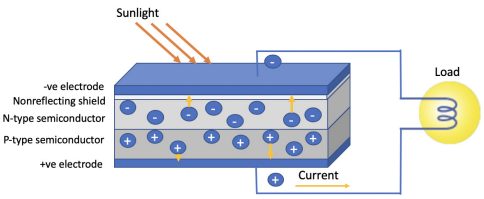

Figure 1.1: Basic solar cell mechanism.

One of the best studied hybrid perovskites is methylammonium lead iodide (MAPI, $CH_3NH_3PbI_3$)[59, 60]. Depending on temperature, it exists in three different phases: cubic (generally reported as pseudo-cubic [27]), orthorhombic and tetragonal [6] as shown in figure 1.2. At room temperature ($\sim$ 300 K) the crystal structure is tetragonal, and at high temperature ($\sim$ 330 K and above) the structure turns into cubic. Theoretical and experimental work has studied the bandgap, bandstructure, and effective mass [36, 46, 70, 34] and the result suggests local symmetry breaking in the structure[152,

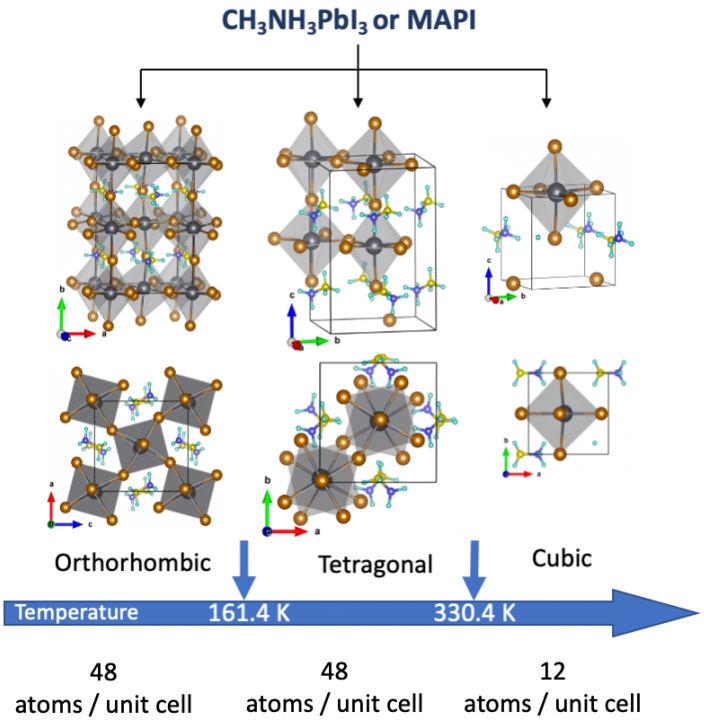

Figure 1.2: Three different phases of methylammonium lead iodide perovskite (MAPI): low temperature orthorhombic phase, room temperature tetragonal phase, and high temperature cubic phase.

85]. Vibrational properties of all three phases have been extensively studied [82, 111, 72, 92, 105, 15, 106, 48]. The IR and Raman spectra of all three phases shows three distinct regimes of the vibrational frequencies, due to the Pb-I cage at low frequency, the methylammonium ion at high frequency, and coupled cage-ion modes in between[106]. There are only a few experimental results on vibrational spectroscopy available for the cubic [82, 92, 111] and tetragonal structures. Qiong Chen *et al.* has reported that it is extremely difficult to find Raman spectra for the pristine MAPI as it is very prone to degradation under the laser illumination, and previously reported results in the low-energy regime may actually represent degradation products [18].

1.2 Theoretical Methods

1.2.1 Density Functional Theory

Every material is made out of a large number of atoms, which means more like 10^{23} of nuclei and electrons. To get the correct description of the material we need to solve a quantum many-body problem that is Schrodinger equation ($H\psi = E\psi$) for interacting electrons and nuclei. The many-body system is described as a collection of electrons and nuclei and the many-body hamiltonian can be written as[110, 47]

$$H = -\sum_i \frac{\hbar^2}{2m_e}\nabla^2_{r_i} - \sum_I \frac{\hbar^2}{2M_I}\nabla^2_{R_I} - \sum_{i,I} \frac{Z_I e^2}{|R_I - r_i|} + \frac{1}{2}\sum_{i\neq j} \frac{e^2}{|r_i - r_j|} + \frac{1}{2}\sum_{I\neq J} \frac{Z_I Z_J e^2}{|R_I - R_J|} \tag{1.1}$$

The mass of the nucleus at R_I is M_I, the electrons have mass m_e at r_i.The first term is the kinetic energy operator for the electrons, the seconds for the nuclei. The last three terms described the Coulomb interaction between electron and nuclei, between electrons and other electrons, and between nuclei and other nuclei. The many-body wave function in the Schrodinger equation involves coordinates of all the electrons. For N number of electrons it is a function of 3N variables. Therefore, this approach is complex and tedious and very difficult to solve. In order to find acceptable approximate eigenstates, some approximations were made at different levels.

The first steps towards the simplification of the above equation is the **Born-Oppenheimer (B-O) approximation**. As ions are much heavier than electrons ($(m_e/M_I \approx 1/1836)$ for H atoms), they move much slower compared to electrons and the electrons respond instantaneously to any ionic motion. Hence, the electronic and the ionic degrees of freedom can be decoupled and the electronic properties can be calculated for a given configuration of ions. Hartree and Fock both tried to solve this problem through wave function approach but in Hartree method exchange and correlation is completely ignored while in Hartree-Fock method exchange interaction is taken into account but there is no correlation energy.

Hohenberg and Kohn proposed Density Functional Theory[57] (DFT) to deal with many-body system problems more efficiently. Instead of dealing with wave functions they considered electron density $n(\vec{r})$ which is a function of only three variables (e.g. x, y, z) to describe the system. Density functional theory is mainly based on two theorems.

1 The external potential $v(\vec{r})$ is a unique functional of electron density $n(\vec{r})$. As a consequence, the total ground state energy E is also a functional of electron density $n(\vec{r})$.

2 The density $n(\vec{r})$ which minimizes the total energy $E[n]$ is the ground-state density and the corresponding energy is the ground-state energy $E[n]$.

In this frame work the total energy functional can be written as

$$\begin{aligned} E[n(\vec{r})] &= \langle\psi|\, V\, |\psi\rangle + \langle\psi|\, T + V_{EE}\, |\psi\rangle \\ &= \int v(\vec{r})n(\vec{r})d^3r + T_s[n] + \frac{e^2}{2}\iint \frac{1}{4\pi\epsilon_0}\frac{n(\vec{r})n(\vec{r'})}{|\vec{r}-\vec{r'}|}d^3r d^3r' + E_{xc}[n] \end{aligned} \tag{1.2}$$

Kohn and Sham tried to solve this equation by introducing the electron density in terms of single particle wave functions as

$$n(\vec{r}) = \sum_{i=1}^{N} |\psi_i(\vec{r})|^2 \tag{1.3}$$

then we have to solve the below equation

$$\left[-\frac{\hbar^2}{2m_e}\nabla^2 + v_{\text{eff}}(\vec{r})\right]\psi_i(\vec{r}) = \epsilon_i\psi_i(\vec{r}) \tag{1.4}$$

where $v_{\text{eff}}(\vec{r}) = v(\vec{r}) + v_H(\vec{r}) + v_{xc}(\vec{r})$. $v(\vec{r})$ is the external potential, $v_H(\vec{r})$ is the Hartree potential and $v_{xc}(\vec{r})$ is the exchange correlation potential as mentioned below.

$$v_H(\vec{r}) = \int \frac{e^2}{4\pi\epsilon_0}\frac{n(\vec{r'})}{|\vec{r}-\vec{r'}|}d^3r' \tag{1.5}$$

$$v_{xc}[n] = \frac{\delta E_{xc}[n]}{\delta n(\vec{r})} \tag{1.6}$$

Equation (1.4) is known as Kohn-Sham (KS) equation[69] and $\psi_i(\vec{r})$, ϵ_i and v_{eff} are the KS orbitals, KS energies and KS potential, respectively and the corresponding Hamiltonian is called the KS Hamiltonian. The KS equation needs to be solved self consistently. Here in KS equation, the exchange-correlation potential $v_{cx}(\vec{r})$ is still unknown. We need to make some approximation to solve this problem.

1.2.2 Exchange-Correlation Functionals

Another difficulty with the application of DFT is that the exact form of $E_{xc}[n]$ is unknown. It is to be noted that this exchange-correlation energy contains (i) kinetic

correlation energy, which is the difference in the kinetic energy functional between the real and the non-interacting system, (ii) the exchange energy, which arises from the requirement of anti-symmetric nature of fermions, (iii) Coulombic correlation energy, which arises from the inter-electronic repulsion and (iv) a self-interaction correction.
The first approximation to this exchange-correlation energy was developed by Kohn and Sham and is known as Local Density Approximation (LDA)[69]. In this approximation it is assumed that the electron density $n(\vec{r})$ varies very slowly in space such that for very small volume element d^3r it can be considered locally uniform. Mathematically it can be expressed as

$$E_{xc}^{LDA}[n] = \int \epsilon_{xc}(n(\vec{r}))n(\vec{r})d^3r \tag{1.7}$$

where ϵ_{xc} is the exchange-correlation energy per particle of the homogeneous electron gas of density $n(\vec{r})$.
Another approximation to the exchange-correlation energy is Generalized Gradient Approximation (GGA)[102]. In this approximation, local variation of density is also accounted by incorporation of the gradient of density $\nabla n(\vec{r})$. Mathematically it is expressed as

$$E_{xc}^{GGA}[n] = \int \epsilon_{xc}(n(\vec{r}), \nabla n(\vec{r}))n(\vec{r})d^3r \tag{1.8}$$

For structural optimization we have used both LDA and GGA but for phonon calculation we have used LDA as it gives fairly good results and also there is a limitation in Quantum-Espresso for doing Raman calculation using GGA.

1.2.3 Pseudopotentials

Another approximation that makes computation less expensive is the use of pseudopotentials[47]. In solids, the valence electrons mainly take any part in the properties like bonding, transport etc. The core electrons barely play any role in these properties, thus the core electrons can be assumed to remain fully occupied and unchanged in all atomic environments as if they are frozen and the focus should be on the valence electrons only. This frozen core approximation enormously reduces the computation cost as the pseudowave function requires a smaller number of plane waves in its expansion than it would have taken for all electron case. For example, in the case of lead (Pb) we need to describe only 14 electrons [$5d^{10}6s^26p^2$] instead of 82 electrons in total. In Fig.1.3 we can see a pseudo wave function for and the corresponding pseudopotential. In figure 1.3 the dotted lines represents 3s all-electron wave function and potential. A pseudization

region is defined based on the cut-off radius, r_c and within this region the original wave function is replaced by a smooth wave function, called pseudo-wave function (in solid grey line) which does not account any variation near the nucleus and out side the cut off radius always coincide with the actual wave function. In figure 1.3 the lower portion of the graph within pseudization region represents the pseudopotential for that region and beyond cut off radius it coincides with the nuclear Coulomb potential corresponding to the valence electronic charge.

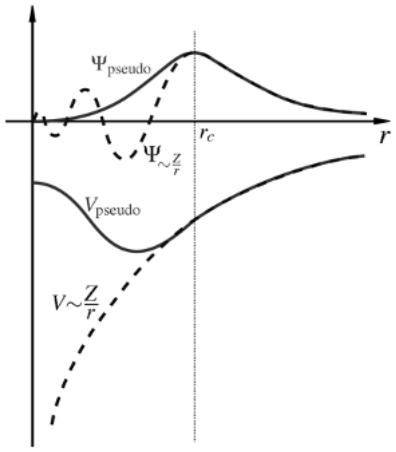

Figure 1.3: Pseudopotential and pseudo wavefunction. r_c represents the cut off radius beyond which pseudopotential matches with the coulomb potential.

1.2.4 Structural Optimization

To understand structural optimization we need to understand Hellman-Feynman force[33] and how it gets calculated. According to Hellman-Feynman theorem, the derivative of the total energy with respect to any parameter is equal to the expectation value of the Hamiltonian with respect to the same parameter.

$$\frac{\partial E_\lambda}{\partial \lambda} = \langle \psi_\lambda | \frac{\partial H_\lambda}{\partial \lambda} | \psi_\lambda \rangle \tag{1.9}$$

The only assumption here is that $|\psi_\lambda\rangle$ is an eigenket of the Hamiltonian H_λ and this makes the theorem general and independent of any specific system. When λ corresponds to the nuclear coordinates R_I, then we get the Hellman-Feynman force. To calculate this force we need to calculate total energy, and for that we need to get correct density. We can start with an initial guess for the density and solve KS equation self consistently

to get the correct density and total energy of the system as shown in the flowchart (Fig. 1.4) by the internal loop. Once we have the correct density and total energy we can easily calculate Hellman-Feynman force and make another SCF cycle as mentioned by the outer loop in the flowchart (Fig. 1.4) to calculate optimized structure.

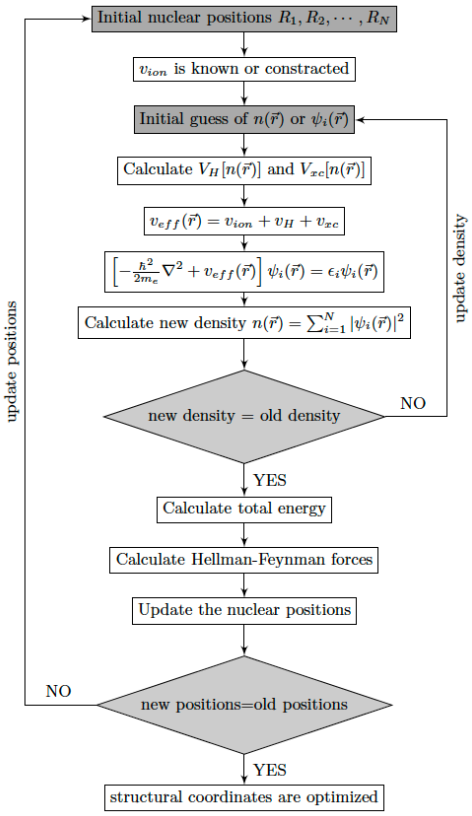

Figure 1.4: Structural optimization flowchart

1.2.5 Calculation of Normal Modes

Due to atomic vibrations the nuclei get displaced from their equilibrium positions. The time-dependent position of each nucleus can be expressed as $R_I(t) = R_I^0 + u_I(t)$ where R_I^0 is the equilibrium position and $u_I(t)$ is the displacement. The equation of motion for each atomic displacement can be written using Newton's law

$$M_I\ddot{u}_I = -\frac{\partial E}{\partial u_I} \tag{1.10}$$

We can do the Taylor series expansion of the total energy E as

$$E(R_1,\cdots,R_N) = E(R_1^0,\cdots,R_N^0) + \frac{1}{1!}\sum_{I,\alpha}\frac{\partial E}{\partial R_{I,\alpha}}\Big|_{R^0_{I,\alpha}} u_{I,\alpha} + \frac{1}{2!}\sum_{I,j,\alpha,\beta}\frac{\partial^2 E}{\partial R_{I,\alpha}\partial R_{J,\beta}}\Big|_{R^0_{I,\alpha}R^0_{I,\alpha}} u_{I,\alpha}u_{J,\beta} \tag{1.11}$$

where $R_{I,\alpha}$ denotes the coordinate of the I_{th} nucleus along α. The first derivative in this equation gives force on the nuclei at equilibrium position which should be zero. Therefore we get,

$$E = E_0 + \frac{1}{2}\sum_{I,j,\alpha,\beta}\frac{\partial^2 E}{\partial R_{I,\alpha}\partial R_{J,\beta}}\Big|_{R^0_{I,\alpha}R^0_{I,\alpha}} u_{I,\alpha}u_{J,\beta} \tag{1.12}$$

The second partial derivative of this equation is known as Born-Von Karman force constant and can be written as

$$K_{I\alpha,J\beta} = \frac{\partial^2 E}{\partial R_{I,\alpha}\partial R_{J,\beta}} \tag{1.13}$$

which is also known as dynamical matrix when normalized with nuclear masses. To get the normal mode frequencies and eigen vectors we need to solve the secular equation

$$\sum_{J,\beta} D_{I\alpha,J\beta}(q)u_{j\beta}(q) = \omega_q^2 u_{I\alpha}(q) \tag{1.14}$$

By diagonalizing the dynamical matrix, we can get the phonon modes at q. Quantum espresso uses DFPT to calculate this dynamical matrix[47].

1.2.6 IR and Raman Calculation

Infra-red spectroscopy

Infra-red spectroscopy is a powerful technique to characterize materials. It is extensively used to characterize molecular functional groups and different kinds of molecular vibrations like bond stretching, wagging etc. When an infra-red light incident on a material, part of it get absorbed by the material and part of it get transmitted. Incident frequencies that matches with the vibrational frequencies (IR active) of the material get absorbed. For a vibrational mode to be IR active it must be associated with changes in dipole moment.

Molecular dipole moment is a function of nuclear coordinates. Therefore, we can Taylor expand the dipole moment as

$$\mu_\alpha = \mu_0\alpha + \sum_{\alpha m}\left(\frac{\delta\mu_\alpha}{\delta Q_m}\right)_0 Q_m + higher\ order\ terms \tag{1.15}$$

where the second term is responsible for IR absorption. Here subscript 0 denotes that the quantity is evaluated at equilibrium condition, Q_m is the normal coordinate associated with the m^{th} mode and α represents Cartesian coordinate. The IR intensity for the m^{th} mode is given by

$$I_m^{IR} \propto \sum_\alpha |\frac{\delta \mu_\alpha}{\delta Q_m}|^2 \tag{1.16}$$

Using the definition of Born effective charge, the intensity can be calculated as[110]

$$I_m^{IR} = \sum_\alpha \Big| \sum_{I\beta} Z_I^{*\alpha\beta} U_I^\beta(m) \Big|^2 \tag{1.17}$$

Here α and β are the x, y, z coordinates, I is the atom index, and Z^* is the Born effective charge.

Raman spectroscopy

Raman spectroscopy has very useful and diverse applications. It can be used as a fingerprinting technique for molecules and helps to characterize materials in solid state by identifying the phonon modes. It is used in the pharmaceutical industry to identify active pharmaceutical ingredients and their polymorphic forms. It has a wide variety of application in biology and medicine. It is aslo used in non-destructive testing, for example, to analyze old painting and chemical composition of historical documents. It is used to detect explosive from a safe distance and can also be used for cancer detection. In addition, it can be used to measure strain in materials[22, 134].

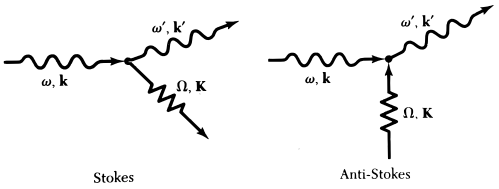

Figure 1.5: Raman scattering[67]

When a monochromatic light (photon) with frequency ω is incident on a system, most of it gets transmitted without much change, in addition to that, some of the radiation get scattered with change in frequencies (ω'). Such scattering with a change in frequency is called Raman scattering. It is mainly a two photon process where one photon comes in and the other goes out. In this case, the incident photon scatter inelastically by the crystal with creation or annihilation of a phonon as shown in the schematic diagram (Fig.1.5).

Raman effect depends on change of polarizability of the system with respect to atomic vibration. If we consider the polarizability to be a function of nuclear coordinates,

then the variation of the component in polarizability tensor with vibrational coordinates can be written as a Taylor series

$$\alpha_{ij} = (\alpha_{ij})_0 + \sum_k \left(\frac{\partial \alpha_{ij}}{\partial Q_k}\right)_0 Q_k + \frac{1}{2}\sum_{k,l}\left(\frac{\partial^2 \alpha_{ij}}{\partial Q_k \partial Q_l}\right) Q_k Q_l + \cdots \tag{1.18}$$

where $(\alpha_{ij})_0$ denotes the value of α_{ij} at equilibrium configuration. Q_k and Q_l are normal coordinates of vibration at frequencies ω_k and ω_l. To get the first order Raman spectra we can neglect the $2^n d$ order term in Taylor expansion. If we consider a harmonic vibration for some K^{th} mode as $Q_k = Q_{k0}\cos(\omega_k t + \delta k)$ and the incident radiation as $E_0 \cos \omega t$ then the induced electric dipole moment can be written as

$$\begin{aligned}\mu^{(1)} = \alpha_0 E_0 \cos\omega t + \frac{1}{2}\left(\frac{\partial \alpha_k}{\partial Q_k}\right)_0 E_0 Q_{k0}\cos(\omega t + \omega_k t + \delta k) + \\ \frac{1}{2}\left(\frac{\partial \alpha_k}{\partial Q_k}\right)_0 E_0 Q_{k0}\cos(\omega t - \omega_k t - \delta k)\end{aligned} \tag{1.19}$$

Here we can see that the linear induced dipole moment $\mu^{(1)}$ has three components with different frequencies. The first term with same frequency ω as the incident radiation is for Rayleigh scattering. The second term with frequency $\omega + \omega_k$ represents anti-Stokes line and third term with frequency $\omega - \omega_k$ represents the Stokes line.

Quantum Espresso calculates the normal modes through DFPT as discussed earlier and then it make use of group theory to find out which modes will be Raman active based on the symmetry. As we know that, if the irreducible representation of a certain vibrational mode have a basis in x^2, y^2, z^2, xy, yz, xz or any linear combination of them then those modes are Raman active. To calculate the Raman intensity, it use the Plackzek approximation[16, 71].

$$I^\nu \propto \left| e_i \cdot \overleftrightarrow{A^\nu} \cdot e_s \right|^2 \frac{1}{\omega_\nu}(n_\nu + 1) \tag{1.20}$$

where e_i and e_s are the polarization of the incident and scattered radiation. $n_\nu = [exp(\hbar\omega_\nu / k_B T) - 1]^{-1}$, T is the temperature.

$$A^\nu_{lm} = \sum_{k\gamma} \frac{\partial^3 \epsilon^{el}}{\partial E_l \partial E_m \partial u_{k\gamma}} \frac{W^\nu_{k\gamma}}{\sqrt{M_\gamma}} \tag{1.21}$$

Here ϵ^{el} is the total electronic energy of the system. E_l and E_m are the l^{th} and m^{th} Cartesian components of the uniform electric field, $u_{k\gamma}$ is the displacement of the γ^{th} atom in the k^{th} direction, M_γ is the atomic mass and $W^\nu_{k\gamma}$ is the orthonormal vibrational eigenmode ν. The third order derivative[71] is calculated by taking the second order

derivative of the DFT density matrix with respect to electric field and then by using Hellmann-Feynman theorem

$$\frac{\partial^3 \epsilon^{el}}{\partial E_l \partial E_m \partial u_{k\gamma}} = 2Tr\left\{\left(\frac{\partial^2 \rho}{\partial E_l \partial E_m}\right)\frac{\partial v^{ext}}{\partial u_{k\gamma}}\right\} \tag{1.22}$$

Here v^{ext} is the external ionic potential and ρ is the DFT density matrix.

1.2.7 Grüneisen Parameter

Grüneisen parameter is an important property of a material that characterizes the anharmonic nature of a solid. For several reasons, such as, strain, temperature etc., volume of a material may change and as a consequence the dynamics of the crystal lattice may change. Grüneisen parameter describes the change in the materials vibrational properties due to the change in its volume. Each vibrational mode behaves differently to external perturbations like strain or temperature. When Grüneisen parameter is considered for each mode of vibration it is known as mode-Grüneisen parameter. It can be expressed as $\gamma_i = -\frac{V}{\omega_i}\frac{\partial \omega_i}{\partial V}$ where γ_i is the mode-Grüneisen parameter for mode i with frequency ω_i and V is the equilibrium volume. for small strains it can also be expressed as[134]

$$\gamma_i = -\frac{1}{\omega_i}\frac{\partial \omega_i}{\partial \epsilon} \tag{1.23}$$

where ϵ is the strain. The macroscopic Grüneisen parameter is the weighted average of all the mode-Grüneisen parameters and also related to the thermal expansion via the below equation

$$\gamma = \frac{\sum_i \gamma_i c_{v,i}}{\sum_i c_{v,i}} = \frac{\alpha K_T}{c_v \rho} \tag{1.24}$$

where $c_{v,i}$ represents the heat capacity for i^{th} mode, α is the volume thermal expansion coefficient, K_T is the isothermal bulk modulus and ρ is the density.

1.2.8 Group Theory and Character Table

Symmetry is a very important property of any material such as molecule or crystal and group theory is the tool that helps to determine the symmetry. Vibrational and electronic spectroscopy use the molecular symmetry extensively. Although majority of the large molecules and solids does not have any symmetry but they might have local symmetries which may be useful. I am not going to discuss the details of group theory or character tables as they are available is any good text book related to symmetry.[54, 25]

I will clarify some of the terms and equations that are used in this work which will serve as a quick reference to follow this work.

A **symmetry operation** is an operation that moves a molecule or crystal structure into a new orientation which is equivalent to its original one and a **symmetry element** is a point, line or a plane with respect to which the symmetry operation is performed. There are five kind of symmetry operations; (1) Proper rotation (C_n), (2) reflection (σ), (3) improper rotation (S_n), (4) inversion (i), and (5) identity (E). C_n is a counter clockwise rotation of $\frac{2\pi}{n}$ about an axis. The rotation axis with the largest n is called the principle axis. An object that has a C_n axis must have 0 or n perpendicular C_2 axis. A mirror plane that is perpendicular to the principle axis is called a horizontal mirror plane and the reflection through this plane is called σ_h. Similarly, vertical (σ_v) and dihedral (σ_d) reflections are through planes that are parallel to the principle axis. An inversion (i) is an operation that transform the (x, y, z) to $(-x, -y, -z)$. An object can have either 0 or 1 inversion center. Improper rotation (S_n) is a rotation followed by a reflection through the plane perpendicular to the axis of rotation. A C_4 rotation followed by a σ^n reflection will create an improper S_4 rotation, example CH_4 molecule.

A **point group** describes all the valid symmetry operations for a molecule that makes the the conformation unchanged after the operation. It also has to obey all the rules of a mathematical **group** as described in the books.[54, 25] Each symmetry operation can be represented by a 3×3 matrix that can transform a set of (x, y, z) coordinates of a molecule or crystal system and is called **transformation matrix**. The symmetry operations are explained for C_{2h} point group in figure 1.6. The **reducible representation (Γ)** is nothing but the trace of these transformation matrices as shown in figure 1.6.

The reducible representation can be further decomposed into its corresponding **irreducible representations** using group theory and the result can be shown in a tabular form which is called **character table**. The character table has its own properties and rules to follow. If two symmetry operations are identical they form a **class**. The total number of symmetry operations are called **order (h)** of the point group. The number of irreducible representations should be equal to the number of classes in the character table. There must be one representation that is totally symmetric (all character are +1). The mathematics of decomposition of reducible representation in to its corresponding irreducible representations are explained in chapter 4. The character table for C_{2h} point

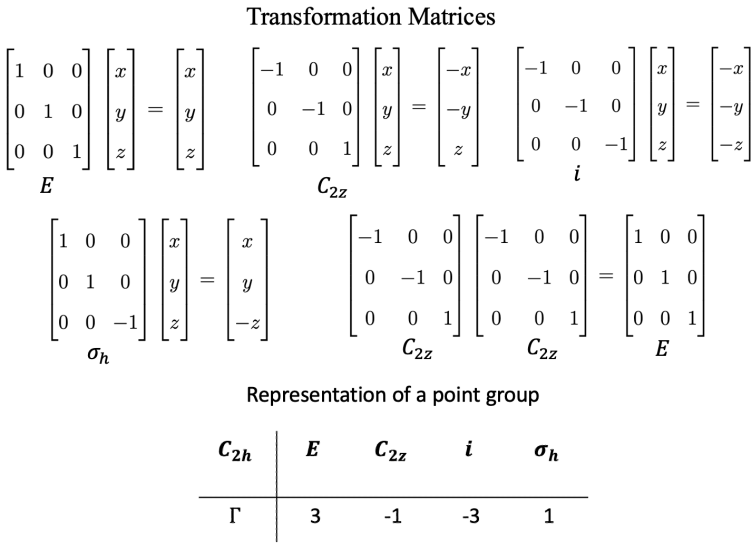

Figure 1.6: Transformation matrices (E, C_{2z}, i, and σ_h) involved in C_{2h} point group and its reducible representation.

group is given in figure 1.7.

C_{2h}	E	C_{2z}	i	σ_h	linear functions, rotations	quadratic functions	cubic functions
A_g	+1	+1	+1	+1	R_z	x^2, y2, z^2, xy	-
B_g	+1	-1	+1	-1	R_x, R_y	xz, yz	-
A_u	+1	+1	-1	-1	z	-	z^3, xyz, x^2z, y^2z
B_u	+1	-1	-1	+1	x, y	-	xz^2, yz^2, x^2y, xy^2, x^3, y^3

Figure 1.7: Character table of C_{2h} point group

Looking at the symmetry of the wave functions and the irreducible representations it is easy to understand which modes will be IR active and which one will be Raman active. In the above case, A_u and B_u will be IR active and both A_g and B_g will be Raman active.

1.2.9 Calculation of Elastic Tensor

When an external force is applied on a material it deforms, but it regains its primary shape whenever the force is withdrawn. This phenomenon is called elasticity. The applied force per unit area is called stress and change in length per unit length is known as strain. Within elastic limit, stress is proportional to strain which is also known

as Hooke's law. Stress and strain are both tensor quantity. For an anisotropic material, if the crystal orientations are in different directions from one grain to another, when force is applied on such material, different amount of strain produced within each grain and we get strain inhomogenity or stress inhomogenity across the grain boundaries and also throughout the material. Sometimes these stress-strain inhomogenities can cause damage to the material. So, understanding of strain and elasticity is important. If σ_{ij} represents the stress tensor and ϵ_{kl} represents the strain tensor then as per Hooke's law we can write

$$\sigma_{ij} = C_{ijkl}\epsilon_{kl} \tag{1.25}$$

where C_{ijkl} is known as the stiffness tensor. It is a 4^{th} rank tensor. The indices i, j, k, l can take values from 1-3 or x,y,z which makes 81 components for C_{ijkl}. Due to symmetry in stress ($C_{ijkl} = C_{jikl}$) and in strain ($C_{ijkl} = C_{ijlk}$) these 81 components drop down to 36 independent components. In contracted notation we can write the stress-strain equation as

$$\begin{pmatrix} \sigma_1 \\ \sigma_2 \\ \sigma_3 \\ \sigma_4 \\ \sigma_5 \\ \sigma_6 \end{pmatrix} = \begin{pmatrix} C_{11} & C_{12} & C_{13} & C_{14} & C_{15} & C_{16} \\ C_{21} & C_{22} & C_{23} & C_{24} & C_{25} & C_{26} \\ C_{31} & C_{32} & C_{33} & C_{34} & C_{35} & C_{36} \\ C_{41} & C_{42} & C_{43} & C_{44} & C_{45} & C_{46} \\ C_{51} & C_{52} & C_{53} & C_{54} & C_{55} & C_{56} \\ C_{61} & C_{62} & C_{63} & C_{64} & C_{65} & C_{66} \end{pmatrix} \begin{pmatrix} \epsilon_1 \\ \epsilon_2 \\ \epsilon_3 \\ \epsilon_4 \\ \epsilon_5 \\ \epsilon_6 \end{pmatrix} \tag{1.26}$$

Since, $C_{ij} = C_{ji}$, it drops this 36 independent component down to 21 components. So, the stiffness matrix is symmetric around the diagonals. Based on the crystal symmetry, these 21 independent components can further be reduced. For example, cubic structure has 4 three-fold rotational symmetry, which brings it down to 3 independent stiffness constants C_{11}, C_{12} and C_{44}. For a crystal structure which does not have much symmetry, we need to calculate all 21 stiffness constants.

We know that elastic strain energy is the energy spent by the external force in deforming an elastic body. This energy divided by the volume is called energy density. It can be shown that the energy density is related to strain and stiffness constants through the equation[67]

$$U = \frac{1}{2}\sum_{\lambda=1}^{6}\sum_{\mu=1}^{6} C_{\lambda\mu}\epsilon_\lambda\epsilon_\mu \tag{1.27}$$

Here $1 = xx$, $2 = yy$, $3 = zz$, $4 = yz$, $5 = zx$ and $6 = zy$. Using equation (1.27) we will be able to calculate all the C_{ij}. Using any of the two equations (eqn-1.25 and eqn-1.27) the full stiffness tensor can be calculated.

Chapter 2

Stress Effects on Vibrational Spectra of a Cubic Hybrid Perovskite: A Probe of Local Strain

2.1 Abstract

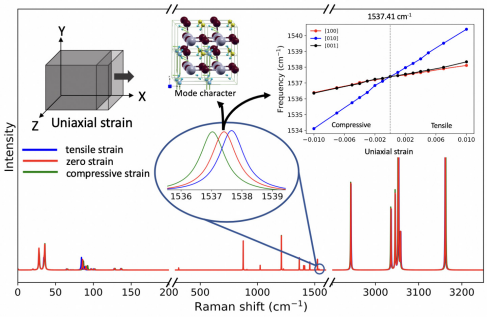

Inhomogeneous strain may develop in hybrid organic metal-halide perovskite thin films due to thermal expansion mismatch with a fabrication substrate, polycrystallinity or even light soaking. Measuring these spatially varying strains is difficult but of prime importance for understanding the effects on carrier mobility, non-radiative recombination, degradation and other optoelectronic properties. Local strain can be mapped using the shifts in vibrational frequencies using Raman or infrared microscopy. We use density functional theory to investigate the effect of uniaxial strain on the vibrations of pseudo-cubic

methylammonium lead iodide ($CH_3NH_3PbI_3$), and identify the vibrational modes most favorable for local strain mapping (86 cm^{-1}, 97 cm^{-1}, 1457 cm^{-1}, and 1537 cm^{-1}) and provide calibration curves. We explain the origin of the frequency changes with strain using dynamical matrix and mode eigenvector analysis and study strain-induced structural changes. We also calculate mode Grüneisen parameters, giving information about anharmonicity and anisotropic negative thermal expansion as recently reported for other phases. Our results provide a basis for strain mapping in hybrid perovskites to further the understanding and control of strain, and improve stability and photovoltaic performance.

2.2 Introduction

Organic-inorganic hybrid perovskites are promising materials for next-generation solar cell applications.[49] They have a direct bandgap, [36, 145] high absorption coefficient-[126] long diffusion length,[133, 156] and large carrier mobility[150] which make them favorable for PV applications. In the last 10 years the record photoconversion efficiency (PCE) has increased drastically from 3.8% [70] to 25.2%.[97] Owing to other benefits like ease of bandgap engineering,[26, 80] flexibility for use in portable electronic devices,[158] tunability of transparency to light for tandem cells,[7] and suitability for mass production[120] with a cheaper cost, perovskites have been the object of great interest in the solar cell industry recently. There are also other non-PV applications of perovskites, *e.g.* spin-optoelectronic applications,[107] luminescent solar concentrators,[95] and light-emitting diodes. [66]

Despite these favorable properties, hybrid perovskites suffer from serious instability due to moisture,[96] heat[21] and light,[62] which hinder their commercialization as solar cells. Although different encapsulation techniques can help to eliminate the moisture issue,[73, 78] degradation due to unavoidable exposure to heat and light is still a challenge that needs to be addressed. Different studies have suggested that strain plays an important role in both degradation and photovoltaic performance of perovskites.[99, 94, 163, 29, 161, 10, 143, 61, 164, 127] This strain arises in thin films via substrate thermal expansion mismatch, epitaxial lattice mismatch,[19] phase transitions, grain structure, and composition inhomogeneities, creating both global and local strain.[61] Strain within the lattice can affect the carrier dynamics,[164] defect concentration, non-radiative recombination,[61] bandgap[161] etc. and decrease the PCE of the

device. Strain can also decrease the activation energy of ion migration within the material which accelerates its degradation.[163] Slow photocurrent degradation caused by deep trap states has been attributed to polarons, consisting of strain and reorientation of the organic ion, which form under light soaking.[94] On the other hand, light soaking can also create lattice expansion which reduces residual strain within the lattice and help to increase efficiency.[143] High compressive strain (more than 1% for cubic $CH_3NH_3PbI_3$) can also be responsible for structural phase changes.[29, 161] To understand all these strain-induced behaviors, we need to understand the structural and vibrational changes due to strain.

In this work, we study as a benchmark system the pseudo-cubic phase of methylammonium lead iodide (MAPI, $CH_3NH_3PbI_3$),[59, 60] one of the best studied hybrid perovskites. Depending on temperature, MAPI exists in three different phases: orthorhombic at low temperature ($T < 161.4$ K), tetragonal at room temperature (161.4 K $< T <$ 330.4 K) and cubic (or pseudo-cubic)[27] at high temperature ($T > 330.4$ K). Both orthorhombic and tetragonal structures are based on $\sqrt{2} \times \sqrt{2} \times 2$ supercells of the cubic structure with four times the number of atoms in the unit cell.

We have chosen to begin with a study of the high-temperature cubic phase due to its simpler structure. Further work will study the orthorhombic and tetragonal structures, which clearly have their own individual characteristics. The cubic phase can be considered as a reference to describe the structures of the other phases.[27] It is not only significant at high temperatures, but also it can be stabilized at lower temperature in quantum dots via ligands on the surface,[122] use of other organic cations [153] such as formamidinium, or substitution of Br for I.[124] Generally cubic phases are found to have higher PCE than the other phases.[160] Due to the strong resemblance between the cubic, tetragonal, and orthorhombic phases' vibrational properties, particularly in the mid-frequency range,[15] we believe this work also gives insight into those phases.

Vibrational properties of all three phases have been extensively studied.[82, 111, 72, 92, 105, 15, 106, 48, 76] The infrared (IR) and Raman spectra of all three phases show three distinct regimes of the vibrational frequencies, due to the Pb-I cage and coupled cage/methylammonium (MA) ion modes at low frequency, and MA ion at medium and high frequency.[106] There are only a few experimental results on vibrational spectroscopy available for the cubic structure[82, 92, 111, 76]. Others have argued that there is no Raman activity of the low-frequency PbI cage modes for cubic

MAPI[18] or cubic $MAPbBr_3$,[84] based on the symmetry argument given for $CsPbCl_3$ and $SrTiO_3$.[27] Observation of small but nonzero Raman activity in this regime was attributed to disorder.[18] However, even in a perfectly ordered cubic MAPI crystal the fact that we have different atomic coordinates from $CsPbCl_3$ means that the PbI cage phonon modes (by hybridization with the MA ion modes) can have other irreducible representations that are Raman active, as indeed we demonstrate in this work. Measurement of low-frequency Raman has been attributed to light-induced degradation products,[18] but our results suggest the validity of at least some measurements in this regime, demonstrated by the agreement in frequencies in Fig. 2.2.

The detailed behavior of vibrational modes under applied tensile and compressive strain for these materials has not been studied. A high-pressure study of $MAPbBr_3$[84] showed only broad features in the cubic phase in the low-frequency region, and clear peaks occurring after phase transition to tetragonal. However the related macroscopic Grüneisen parameter γ, and the related thermal expansion, have been studied. For the tetragonal structure, a negative thermal expansion coefficient was measured along the [001] direction (c-axis).[40, 55] For the cubic structure, the Grüneisen parameter was calculated and measured in previous studies[40, 15] but not along all three crystallographic axes. γ (including the individual mode Grüneisen parameters, also known as phonon deformation potentials[3]) are of fundamental interest as a probe of anharmonicity, which is quite strong in perovskites[28, 165] and relates to phonon-phonon scattering and thermal transport.

Using strain effects on vibrations to measure local strain can help us to understand the material degradation and its performance instability. To measure local strain within a material, we want to focus on a length scale $\sim \mu$m or below. Most of the experiments done so far to measure strain in perovskites have used grazing incidence X-ray diffraction (GIXRD), normal XRD[121, 143, 164, 163] or the substrate curvature method [121] which probe large areas. Scanning XRD has been used for more local mapping, but requires a synchrotron.[61] Another standard non-destructive technique used to characterize perovskites and other semiconductor thin films is Raman spectroscopy.[108] Raman microscopy, in which small areas are probed, can be used to measure the stress distribution within a material. This is a well established technique for crystalline Si (c-Si) in the semiconductor industry,[22] and is used for 2D materials.[115] It can even be used in hydrogenated amorphous silicon, a disordered material with very

broad peaks, as we showed in a previous theory-experiment collaboration.[134] This method has resolution on the μm scale, or even down to nanometers with tip-enhanced Raman spectroscopy.[135] Synchrotron-based IR microscopy has also been used for local mapping of strain and related structural changes.[83, 128]

In this paper, we analyze vibrations under compressive and tensile strain for cubic $CH_3NH_3PbI_3$ and determine the calibration data needed to gauge local strain. The paper is organized as follows. In section II we detail our computational methods of structural optimization, calculation of normal mode frequencies and theoretical framework to understand frequency shifts in terms of perturbations of the dynamical matrix and mode eigenvectors. In section III, we discuss the behavior of phonon modes under uniaxial strain, understand the different behaviors in terms of structural changes and dynamical matrix analysis, find the best possible modes to probe local strain using Raman spectroscopy, and calculate the Grüneisen parameter and compare to other theory and experimental data. In section IV, we conclude and present the four best modes for measuring strain using Raman or IR spectra.

2.3 Methods

2.3.1 Computational Details

For structural optimization and phonon mode calculations we have used density functional theory (DFT) and density functional perturbation theory (DFPT) [9] as implemented in Quantum ESPRESSO (version 6.1)[43, 44, 8]. The Brillouin zone is sampled using a half-shifted 6×6×6 Monkhorst-Pack grid with an energy cutoff of 100 Ry for the wave-functions. Atomic positions are optimized until the total force per atom is smaller than 1 meV/Å; for the initial variable-cell relaxation, a 0.5 kbar stress convergence threshold is used. The Local Density Approximation[101] (LDA) with the Perdew-Wang (PW) parametrization[104] is used for the exchange-correlation potential for all the calculations. Scalar relativistic Optimized Norm-Conserving Vanderbilt (ONCV) pseudopotentials[53] are used which treat Pb $5d$ orbitals as valence. All the pseudopotentials are taken from Pseud$\bar{o}$ D$\bar{o}$j$\bar{o}$[146] (NC SR ONCVPSP v0.4) with standard accuracy. We have not considered spin-orbit coupling as it does not have much effect on interatomic interactions near equilibrium.[15]

The initial structure is taken from the work of Brivio *et al.*,[52, 15] with the

cation oriented close to the [100] direction, which was found to be slightly favored in molecular dynamics. It can be difficult to obtain an optimized exact cubic structure of MAPI without distortion to other phases.[36] Some experiments show the structure as cubic,[151] others pseudo-cubic.[6, 132] Experimental work reports the fast reorientation of the $CH_3NH_3^+$ ion and also the rotation of CH_3 and NH_3 groups along the C-N axis, and these rotations and reorientation are extremely fast ($\sim$14 ps).[75] These motions can make a cubic symmetry averaged over space and time, but obviously cannot be captured in a static DFT calculation, which instead represents a single local snapshot. A periodic calculation imposes an artificial long-range order, but our dynamical matrix calculations suggest that this does not have an important effect on the vibrational properties (Sec. 3.3), consistent with the conclusion of Leguy *et al.*[76] that dynamical disorder broadens peaks in MAPI but does not shift them significantly. Local asymmetry in the structure along with spin-orbit coupling has been calculated to cause splitting and an indirect gap.[152, 85] A theoretical study showed that changes in the c/a ratio are coupled to the orientation of the $CH_3NH_3^+$ ion.[99] Our structural optimization makes the structure pseudo-cubic, in agreement with other calculations.[99, 15] As in standard DFT calculations, our lattice is at zero temperature, and the high temperature at which the cubic phase is observed does not enter into the calculations.

The equilibrium structural parameters are reported in Table 2.1. More detailed information, including results with different functionals, are reported in Table 2.5, along with bandgaps in Table 2.4 and the LDA bandstructure in Fig. 2.12 in agreement with previous work.[46] Optimized crystallographic angles α, β and γ are 90°, 88.8° and 90° respectively. Pb-I-Pb angles are 164.65°, 163.46° and 173.92° along a, b and c axes, respectively. The C-N bond-length is found to be 1.47 Å with average C-H and N-H bond lengths of 1.1 Å and 1.05 Å. Due to the pseudocubic lattice, off-centering of the Pb atom, cation orientation, and distortion of the Pb-I cage, the structure has no symmetry,[27] even when we checked the structure without the $CH_3NH_3^+$ ion or with the H atoms removed. Our final relaxed cation orientation has the C-N bond lying in the (010) plane, at an angle of 23.3° to the a-axis ([100] direction).

Before applying strain to the structure, the convergence of the phonon frequencies with respect to the k-grid and phonon self-consistency threshold are checked, and all the calculations are done using phonon self-consistency threshold 10^{-16} to avoid imaginary frequencies at the Γ point. We compared different functionals (PBE,[102]

Table 2.1: Optimized cell parameters for cubic $CH_3NH_3PbI_3$ from DFT energy minimization and comparison with previous studies using DFT/PBEsol, [15, 52] powder neutron diffraction (PND)[151] and single crystal XRD methods [132].

	a (Å)	**b (Å)**	**c (Å)**	α (deg.)	β (deg.)	γ (deg.)
DFT/LDA	6.163	6.115	6.267	90.00	88.80	90.00
DFT/PBE	6.499	6.410	6.532	90.00	88.66	90.00
DFT/PBEsol	6.291	6.248	6.378	90.00	88.64	90.00
DFT/PBEsol[15, 52]	6.289	6.229	6.374	90.00	88.74	89.99
PND (352 K)[151]	6.317	6.317	6.317	90.00	90.00	90.00
XRD (400 K)[132]	6.311	6.311	6.316	90.00	90.00	90.00

PBEsol[103] and LDA[101]) and found only small changes in mode frequencies at $q = 0$. For low-frequency phonons, the pattern is LDA>PBEsol>PBE whereas for medium (800–1600 cm^{-1}) and high (2900–3200 cm^{-1}) frequencies it is LDA<PBEsol<PBE with most deviation at high frequencies, as shown in Fig. 2.1. For this comparison, we have performed the variable-cell relaxation using the same functional used to calculate the phonon frequencies.

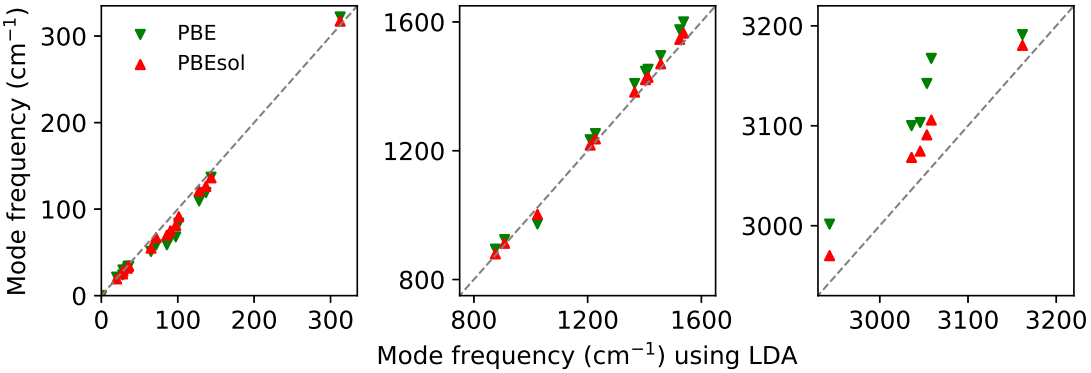

Figure 2.1: Comparison of $q = 0$ phonon frequencies calculated with different functionals showing good agreement across the low- and mid-frequency ranges, and some deviations at high frequencies.

For reference, we performed similar calculations for the well studied case of c-Si (Fig. 2.11) and the result follows the same low frequency pattern LDA>PBEsol>PBE that we have found in cubic MAPI. We apply uniaxial strain in the [100] direction and plot frequency changes, as the three degenerate optical phonons are split into a doublet and singlet. Results are shown in Table 2.6 and Fig. 2.11. LDA in fact has the best

agreement with experiment[100, 2] for both frequency and slope, in this case; PBEsol is similar, but PBE is more different.

Moving now to the effect of strain on cubic MAPI, we applied up to 1% uniaxial compressive (negative, in our convention) and tensile (positive) strain along the three crystallographic directions [100], [010] and [001] to the optimized zero-strain structure. Shear strains were not calculated as they generally have a smaller effect on the frequencies[22], and are less commonly found in thin films. We considered results up to ±0.4% strain where the changes in frequency with the applied strain are typically at least 1 cm^{-1}, which is generally measurable in Raman spectroscopy.[92] Strain more than ±0.4% gives more signal-to-noise ratio, but more modes also become nonlinear. To make sure that this strain range is appropriate for studying linear responses, we have also computed the elastic constants by applying isotropic, tetragonal, and trigonal strain to the cubic MAPI lattice and thereby calculating elastic constants C_{11}, C_{12} and C_{44} following the procedure based on a quadratic fit of total energy[47]. Within the range of ±0.4%, our result with LDA shows reasonable agreement with previously published results (Table 2.2). Note that we have separately calculated each diagonal element of the elastic constant tensor, and found some differences between them due to the pseudocubic lattice and lack of symmetry, whereas previous reports appeared to assume perfect cubic symmetry and calculated only C_{11} and C_{44}.[29, 31]

Table 2.2: Calculated values of elastic constants in GPa for cubic $CH_3NH_3PbI_3$.

	$\mathbf{C}_{11}$	$\mathbf{C}_{22}$	$\mathbf{C}_{33}$	$\mathbf{C}_{44}$	$\mathbf{C}_{55}$	$\mathbf{C}_{66}$
LDA (this work)	38.1	40.5	38.7	2.8	2.5	3.7
PBE[31]	27.1	-	-	9.2	-	-
PBEsol+vdW[29]	35.4	-	-	6.1	-	-
PBEsol[29]	30.9	-	-	3.2	-	-

Having confirmed reasonable results for LDA on phonon frequencies and elastic constants, we are using LDA for all our strain and phonon calculations as Quantum ESPRESSO can only provide Raman intensities for LDA.[71] The code's `ASR=crystal` setting is used to enforce the acoustic sum rule (ASR) and make the acoustic modes ex-

actly zero.[90] For each mode, we have calculated the uniaxial mode Grüneisen parameter for [100], [010] and [001] crystallographic directions using the slope of the frequency versus strain graph, with the formula $\gamma_i = -\frac{1}{\omega_i}\frac{d\omega_i}{d\epsilon}$, where ϵ is the applied strain and ω_i is the frequency of mode i[134]. By taking the weighted average over all the modes, we have calculated the temperature-dependent Grüneisen parameter $\gamma = \frac{\Sigma_i \gamma_i C_{v,i}}{\Sigma_i C_{v,i}}$. This is connected to the macroscopic property of the material by the relation $\gamma = \frac{\alpha K_T}{C_v \rho}$ where α is volume thermal expansion coefficient, K_T is isothermal bulk modulus, C_v is heat capacity at constant volume and ρ is the density.[147] Raman intensities are calculated using the approach of Lazzeri *et al.*[71] and IR intensities computed from Born effective charge tensors which are calculated as the variation of macroscopic polarization with the atomic displacement using the modern theory of polarization[32, 9].

2.3.2 Theoretical frame-work for the frequency change

To obtain the normal mode frequencies, we solve the secular equation[9] given below:

$$\sum_{J,\beta} D_{I\alpha,J\beta} u_{J\beta} = \omega^2 u_{I\alpha} \tag{2.1}$$

where I, J denote atoms within the unit cell; α, β represent x, y and z directions; $D_{I\alpha,J\beta}$ is the dynamical matrix of the system; and $u_{I\alpha}$ represents the mode eigenvector. The dynamical matrix can be expressed as

$$D_{I\alpha,J\beta} = \frac{1}{\sqrt{M_I M_J}}\Big(\frac{\partial^2 E}{\partial R_{I\alpha} \partial R_{J\beta}}\Big) \tag{2.2}$$

where E is the total energy of the system, R_I denotes the position vector of atom I, and M_I denotes mass of atom I. For non-strained condition, the normal-mode frequency ω will be represented as ω_0. To treat the variation of ω with strain, we write ω^2 as

$$\omega^2 = \sum_{I\alpha,J\beta} u^*_{I\alpha} D_{I\alpha,J\beta} u_{J\beta} \tag{2.3}$$

Strain can be treated as a perturbation to the vibrational properties of the material. The perturbation changes the dynamical matrix as well as the mode eigenvectors of the system, as given in equations (2.4) and (2.5) (up to quadratic order):

$$D^{\epsilon}_{I\alpha,J\beta} = D^0_{I\alpha,J\beta} + \sum_{l,m} \frac{\partial D_{I\alpha,J\beta}}{\partial \epsilon_{lm}} \epsilon_{lm} + \frac{1}{2} \sum_{l,m,l',m'} \frac{\partial^2 D_{I\alpha,J\beta}}{\partial \epsilon_{lm} \partial \epsilon_{l'm'}} \epsilon_{lm} \epsilon_{l'm'} + \cdots \tag{2.4}$$

$$u^{\epsilon}_{J\beta} = u^{0}_{J\beta} + \sum_{l,m} \frac{\partial u_{J\beta}}{\partial \epsilon_{lm}} \epsilon_{lm} + \frac{1}{2} \sum_{l,m,l',m'} \frac{\partial^2 u_{J\beta}}{\partial \epsilon_{lm} \partial \epsilon_{l'm'}} \epsilon_{lm} \epsilon_{l'm'} + \cdots \tag{2.5}$$

Since the mode eigenvectors are real in our case at $q = 0$, we can use $u^{*}_{I\alpha} = u_{I\alpha}$. If we apply the perturbed dynamical matrix with perturbed eigenvector to equation (2.3), we can calculate the change in frequency as

$$\begin{aligned} \omega^2_{\epsilon} - \omega^2_0 = \sum_{I\alpha,J\beta} \sum_{l,m} \left\{ u^{0}_{I\alpha} \left(\frac{\partial D_{I\alpha,J\beta}}{\partial \epsilon_{lm}} \right) u^{0}_{J\beta} \right\} \epsilon_{lm} + \\ \sum_{I\alpha,J\beta} \sum_{l,m,l',m'} \left\{ \frac{1}{2} u^{0}_{I\alpha} \left(\frac{\partial^2 D_{I\alpha,J\beta}}{\partial \epsilon_{lm} \partial \epsilon_{l'm'}} \right) u^{0}_{J\beta} + \left(\frac{\partial u_{I\alpha}}{\partial \epsilon_{lm}} \right) D^{0}_{I\alpha,J\beta} \left(\frac{\partial u_{J\beta}}{\partial \epsilon_{l'm'}} \right) + \right. \\ \left. 2 u^{0}_{I\alpha} \left(\frac{\partial D_{I\alpha,J\beta}}{\partial \epsilon_{lm}} \right) \left(\frac{\partial u_{J\beta}}{\partial \epsilon_{l'm'}} \right) + u^{0}_{I\alpha} D^{0}_{I\alpha,J\beta} \left(\frac{\partial^2 u_{I\alpha}}{\partial \epsilon_{lm} \partial \epsilon_{l'm'}} \right) \right\} \epsilon_{lm} \epsilon_{l'm'} + \cdots \end{aligned} \tag{2.6}$$

The above equation can be used to find the change in frequency[22] due to strain ϵ as

$$\Delta\omega \approx \frac{\omega^2_{\epsilon} - \omega^2_0}{2\omega_0} \tag{2.7}$$

For silicon, a simple matrix equation for the Raman-active transverse optical (TO) modes has been theoretically derived[3, 38] and experimentally verified,[38] but for the pseudo-cubic perovskite the secular equation is more complicated as it has five different types of atoms and has no symmetry or degeneracy. Instead, to analyze this situation, we have considered changes in eigenvectors with strain, as well as the changes in the dynamical matrices to clearly understand which atomic interactions contribute significantly to the changes in phonon frequencies, as detailed in section 3.3.

2.4 Results and Discussion

2.4.1 Behavior of phonon modes under uniaxial strain

Calculated normal modes at $q = 0$ of cubic $CH_3NH_3PbI_3$ show three distinct frequency regions – low (20-350 cm^{-1}), medium (850-1600 cm^{-1}) and high (2900-3200 cm^{-1}) – as described for cubic as well as orthorhombic and tetragonal structures in previous studies.[15] Low-frequency modes are mainly due to the vibration of PbI_6 octahedra and some coupling between the PbI_6 octahedra and $CH_3NH_3^+$ ion, while the medium and high frequency modes involve the vibration of the $CH_3NH_3^+$ ion. Since pseudo-cubic $MAPbI_3$ does not have any symmetry,[27] it is not possible to assign spectral activity to

any particular mode using group theory. All modes show both IR and Raman activity to some degree.

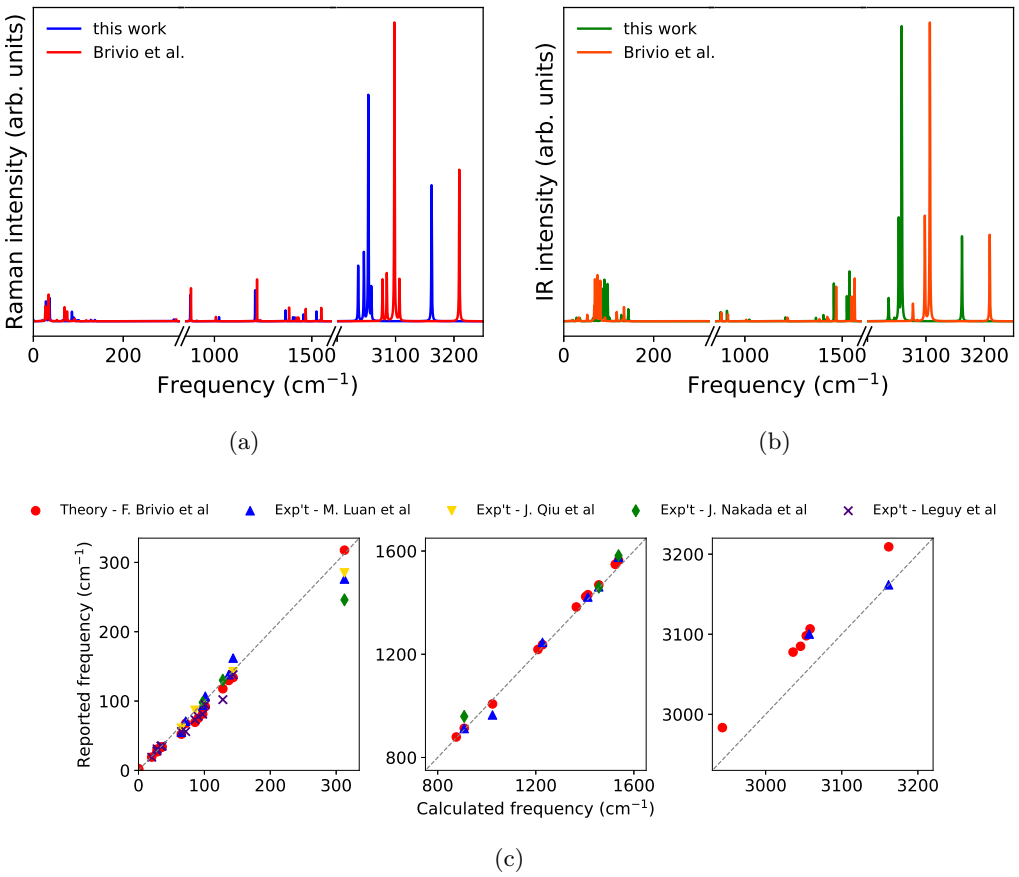

Figure 2.2: Comparison of calculated Raman and infrared frequencies. (a) Comparison of Raman spectrum convolved with 1 cm^{-1} Lorentzian broadening, with calculation of F. Brivio *et al.* [15] (b) Similar comparison for IR spectra. (c) Comparison of our calculated frequencies with published theoretical[15] and experimental results: IR in Luan *et al.*,[82] Raman in Qiu *et al.*[111] and Nakada *et al.*,[92] and THz in Leguy *et al.*[76]

Our *ab initio* IR and Raman results are shown in Fig. 2.2. Calculated Γ-point phonon modes are convolved with 1 cm^{-1} Lorentzian broadening and compared with the calculations of F. Brivio *et al.*.[15] The difference in results are primarily due to our use of LDA and their use of PBEsol, as expected from Fig. 2.1. Calculated frequencies match well with published theoretical results,[15] and experimental measurements from THz at low frequencies [76] and Raman[92, 111] and IR[82] at medium to high frequencies.

We have 12 atoms in our unit cell for cubic $CH_3NH_3PbI_3$, which gives 36 phonon

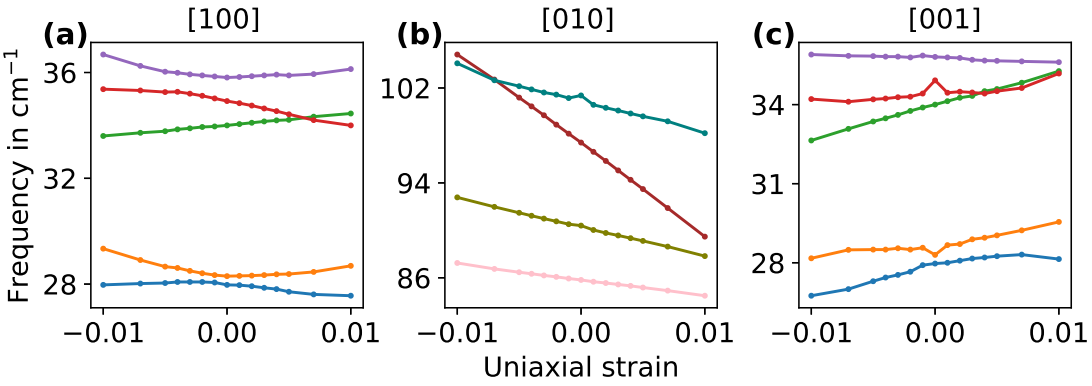

Figure 2.3: Frequencies of modes which approach or cross under strain, giving rise to parabolic or irregular behavior in frequency *vs.* strain.

modes, of which 3 have exactly zero frequency according to the ASR. For the other 33 modes we plotted frequency *vs.* applied strain (both compressive and tensile). Different patterns are noticed for different modes. Some of them are linear, some are parabolic, and some are neither (Fig. 2.4). For comparison, c-Si shows linear changes for small strain, and a splitting of degeneracy (Fig. 2.11). Given the much more complicated structure of the perovskite and lack of symmetry (hence no degeneracy), more complex behavior is observed. Low-frequency modes (27.97 cm^{-1}, 28.3 cm^{-1}, 34.92 cm^{-1} and 35.81 cm^{-1}), which closely approach other modes under strain, show the parabolic pattern expected for an avoided crossing in phonons (or electronic bands), along with mixing and exchange of eigenvector character on either side of the crossing. The modes which approach or cross under strain are shown in Fig. 2.3. Using the eigenvectors as a guide, in a few cases we found crossing of modes under strain, and therefore relabeled the modes to maintain a continuous character. Other modes with irregular behavior show even more mixing between modes, in a non-perturbative way, which we attribute to strong coupling to structural changes as discussed in Sec 3.2. Those modes where the frequency change is mostly linear can be categorized into four different categories: i) slopes of [100] and [010] strain are of same sign while slope of [001] is opposite sign (*e.g.* 143.6 cm^{-1}, 3053.38 cm^{-1}), ii) slopes of [010] and [001] strain are of same sign while slope of [100] is of opposite sign (*e.g.* 908.09 cm^{-1}, 1403.54 cm^{-1}), iii) slopes of [100] and [001] strain are of same sign while slope of [010] is of opposite sign (*e.g.* 20 cm^{-1}, 34 cm^{-1}) and iv) all slopes have same sign for [100], [010] and [001] strains (*e.g.* 97.4 cm^{-1}, 312.59 cm^{-1}). The number of modes falling under different slope categories are given in Table

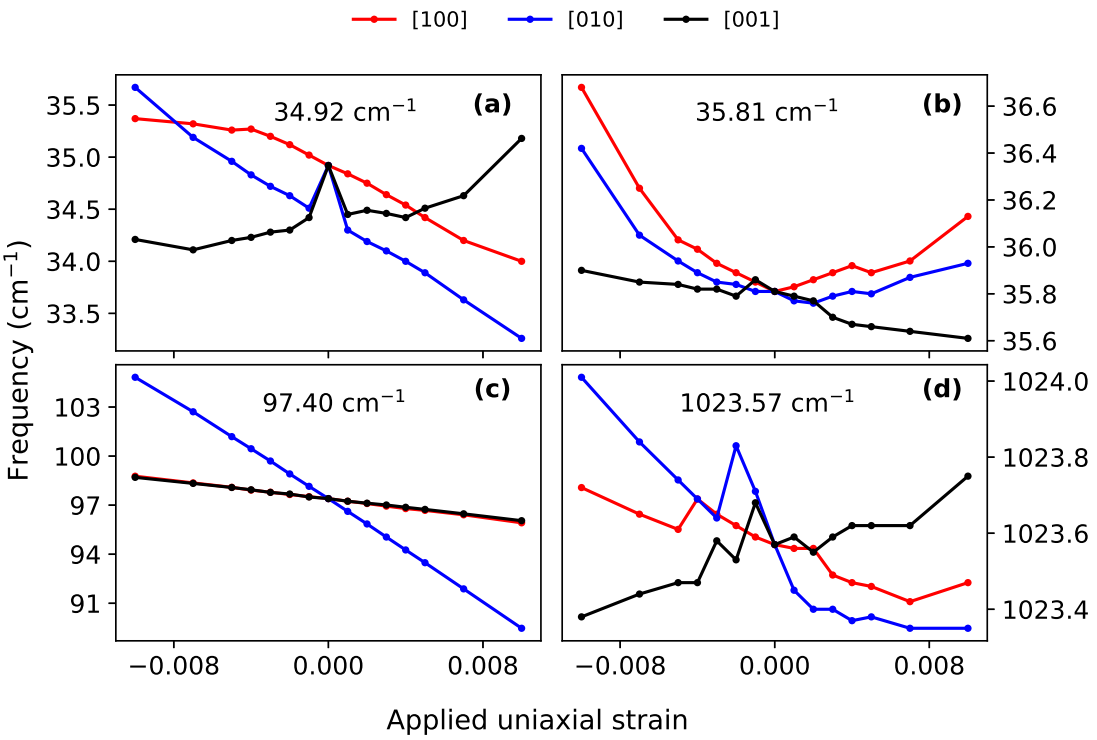

Figure 2.4: Typical patterns for frequency changes with applied compressive and tensile strain in three crystallographic directions [100], [010] and [001]. (a) Deep kink at zero strain for [010] and [001] but otherwise almost linear. (b) Parabolic pattern for [100] and [010] uniaxial strain. (c) Linear pattern. (d) Erratic pattern, neither linear nor parabolic.

2.9 and the frequency change pattern for most of the modes is linear. There are some modes for which the slopes are almost the same for two different directions. For example, 97.4 cm^{-1} has Pb-I-Pb bending perpendicular to both [100] and [001], giving rise to the same slopes for these strain directions. For 1365.3 cm^{-1}, symmetric umbrella type C-H bending has components in all directions and has comparable behavior for [100] and [010] strain directions. These behaviors indicate approximate symmetries of particular modes despite the lack of overall symmetry. In Fig. 2.4, we provide four representative modes' frequency *vs.* strain patterns.

To understand these behaviors, we plotted eigenvectors (displacement patterns) for each mode, contributed by each atom in the unit cell as $|u_I| = \sqrt{(u_{Ix}^2 + u_{Iy}^2 + u_{Iz}^2)}$; those for the chosen four representative modes are given in Fig. 2.5. We noticed

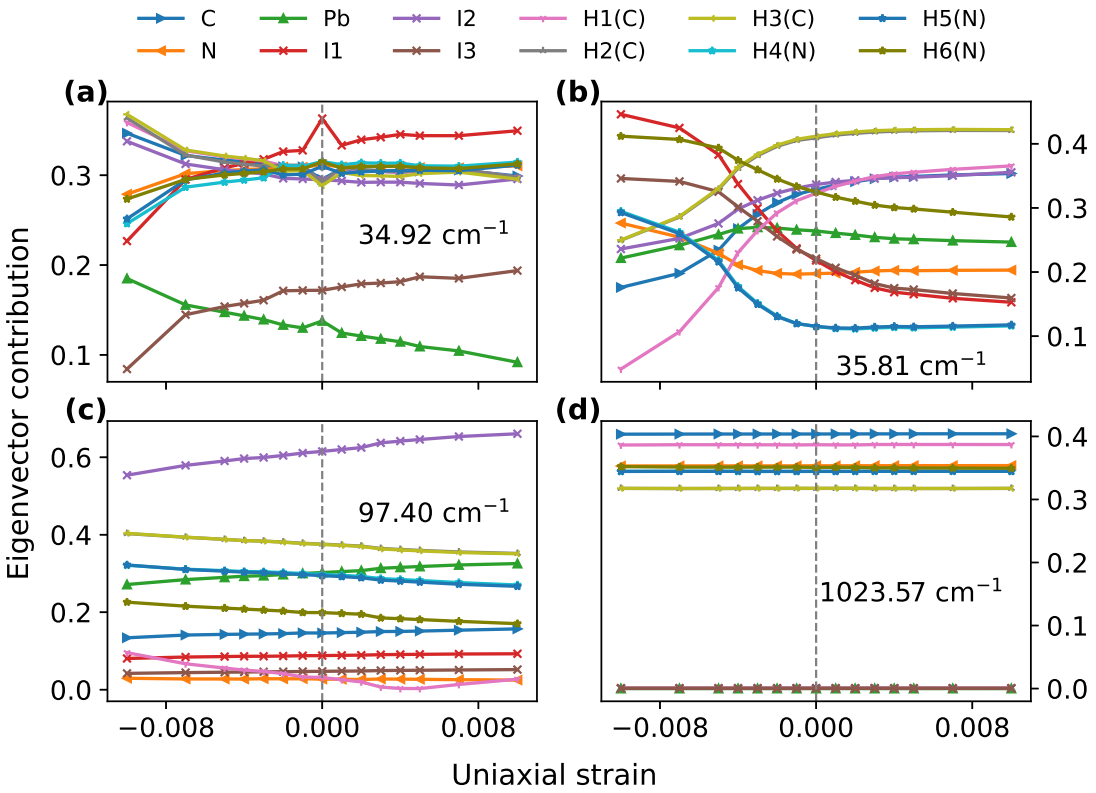

Figure 2.5: Contributions of each atom in the eigenvectors for each of the representative modes presented in Fig. 2.4. Uniaxial strains are in the (a) [010], (b) [100], (c) [001], and (d) [001] directions, showing connections between parabolic or other nonlinear frequency behavior in (a) and (b) with significant changes in mode character, while (c) has little character change and linear frequency behavior, and (d) anomalously has little character change but erratic frequency behavior which will be explained in 2.4.2.

that the change in frequency with strain is linear when the eigenvector does not change appreciably but the dynamical matrix does, as the effect of 2^{nd} order change in dynamical matrix comes in only at 2^{nd} order (Eqn. 2.6). Due to the lack of symmetry, the dynamical matrix elements always have a change with strain in this system. On the other hand, if the eigenvector does change, we can have some non-linear effect in the frequency change which can be understood from the second-order part of Eqn. 2.6. In most cases, the dynamical matrix change is large enough to produce effects beyond quadratic. For example, Fig. 2.4(a) shows a kink at zero for the frequency for both [010] and [001] strain while for [100] strain it is almost linear (parabolic under compressive strain). We

can see that the change in mode eigenvector for the corresponding mode shows a drastic change at zero for strain along [010] direction (Fig. 2.5(a)) and the mode's character is a combination of translation of the $CH_3NH_3^+$ ion along [001] direction and Pb-I-Pb rocking mode. Fig. 2.4(b) shows parabolic frequency changes for [100] and [010] strain which can be understood from the changes of the eigenvector and close approach with another mode (Fig. 2.5(b)). This mode is a combination of $CH_3NH_3^+$ ion libration in the [010] direction and a Pb-I-Pb rocking mode. In Fig. 2.4(c) we can see that the frequency change is linear and if we check the corresponding change in eigenvector (Fig. 2.5(c)) we can see that there are very little change with strain which as per Eqn. 2.6 will produce a linear pattern. The mode character for this mode is libration and spin (all the H atoms attached to C and N are rotating in the same direction) of $CH_3NH_3^+$ ion, and Pb-I-Pb bending. Finally, in Fig. 2.4(d) we found that the frequency change pattern is irregular despite the very little change in atomic contributions to the eigenvector (Fig. 2.5(d)). This is because the x, y and z components for C, N and H are changing irregularly with strain even though the sum of squares over the Cartesian directions is constant for each atom. This is a pure molecular mode with symmetric C-H and N-H bending with C-N stretch. We find that generally C-H and N-H vibrations are associated with nonlinear changes in the mode character under strain. We will see by structural and dynamical analysis that C-H, N-H vibrations are important for most of the frequency change under strain. Corresponding plots for all modes are given in Fig. 2.27-2.33.

2.4.2 Structural Changes under uniaxial strain

While highly symmetric structures such as c-Si do not have internal parameters that can change with strain, in hybrid perovskites, the structure evolves under applied strain, which can play a role in vibrational changes. The significant changes are a sign of the anharmonicity of MAPI. Lengths of bonds parallel to strain are changed most, but those perpendicular to the direction of strain are also affected. For example, the Pb-I bond length along [100] changes most for strain along [100] but Pb-I bond lengths along other two perpendicular directions, such as along [010] and [001] are also changing as shown in Fig. 2.6(a). This change in bond lengths in the perpendicular direction to the strain is more prominent when the strain is acting perpendicular to the direction of the methylammonium ion which is close to [100] (Fig. 2.24). The Pb-I-Pb bond angles also change with applied strain: they decrease with compressive strain acting parallel to

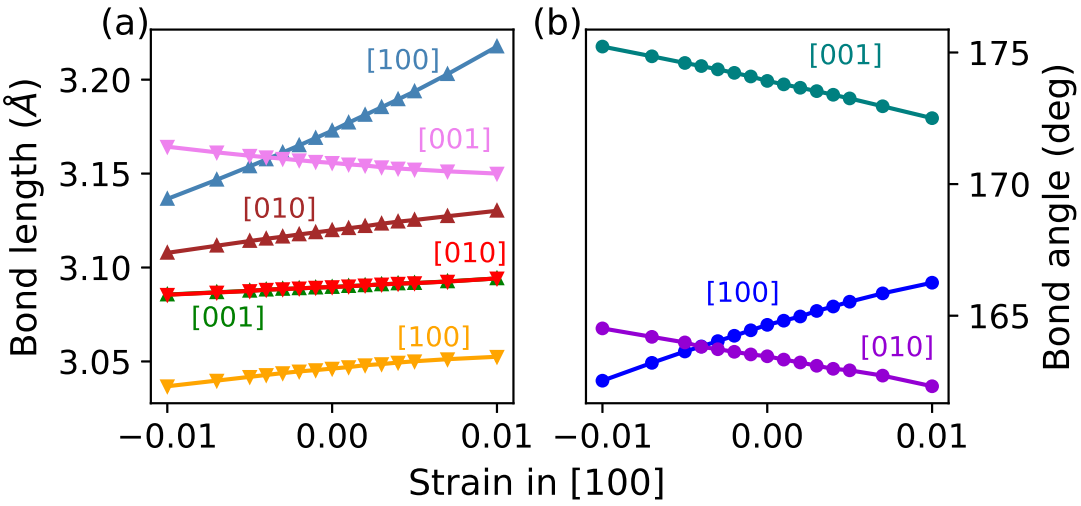

Figure 2.6: Change in Pb-I bond length and Pb-I-Pb bond angle in cubic MAPI for uniaxial [100] strain, showing fairly linear relationships, and a buckling of the Pb-I cage. These are the six Pb-I bonds, labeled by the crystal direction of the bond, and three Pb-I-Pb angles along [100], [010] and [001] directions respectively.

the bond angle and increase when it is acting perpendicular to the bond angle as can be seen in Fig. 2.6(b). Pb-I-Pb bond angle which is along [100] decrease, and those along [010] and [001] directions increase for compressive strain along the [100] direction. Similar behavior is found in a theoretical study for tetragonal structure where the Pb-I-Pb bond angle which is parallel to the strain direction increases for tensile strain and decreases for compressive strain, but the Pb-I-Pb bond angle perpendicular to the strain direction increases for compressive strain and decreases for tensile strain.[161] There are almost no changes (<0.007%) in the C-N bond length but the N-H bond length (along [001]) decreases with compressive strain (Fig. 2.20). This reduction in N-H bond length supports the idea that compressive strain may be useful to stabilize the material.[157, 116]

The $CH_3NH_3^+$ ion, which lies in the (010) or xz-plane also rotates with an increasing angle with respect to the [100] direction or a-axis under compressive strain and a decreasing angle under tensile strain (Fig. 2.17), with changes of up to 1.5° over our strain range which is related to the change in c/a ratio[99] as mentioned in Sec. 2.1. Rotation is largest for [010] strain. This may be due to the fact that the $CH_3NH_3^+$ ion lies in the (010) plane perpendicular to [010]. Rotation of $CH_3NH_3^+$ is also reported for

tetragonal structure under compressive strain.[161] The distances of C and N with their nearest Pb and I change with strains and the discontinuity in the I-N, I-C, N-Pb and C-Pb distances gives an indication why we see certain kinks or irregularities in the Raman shift vs strain graphs. For example, mode 128.01 cm^{-1} shows kinks in the frequency change pattern (Fig. 2.27-2.33) where C-H and N-H are showing asymmetric bending modes with libration of the MA ion within the Pb-I cage, which is affecting the C-Pb and I-N distances most. Similarly, for 1023.57 cm^{-1}, we see that the irregularity is greater for [010] and [001] strain than [100]. We have further analyzed these changes in terms of the dynamical matrix in the next section. Full plots of structural parameters with each direction of strain are in Fig. 2.24-2.17, and all atomic coordinates and phonon eigenvectors of relaxed strained structures are provided in the Supporting Information.

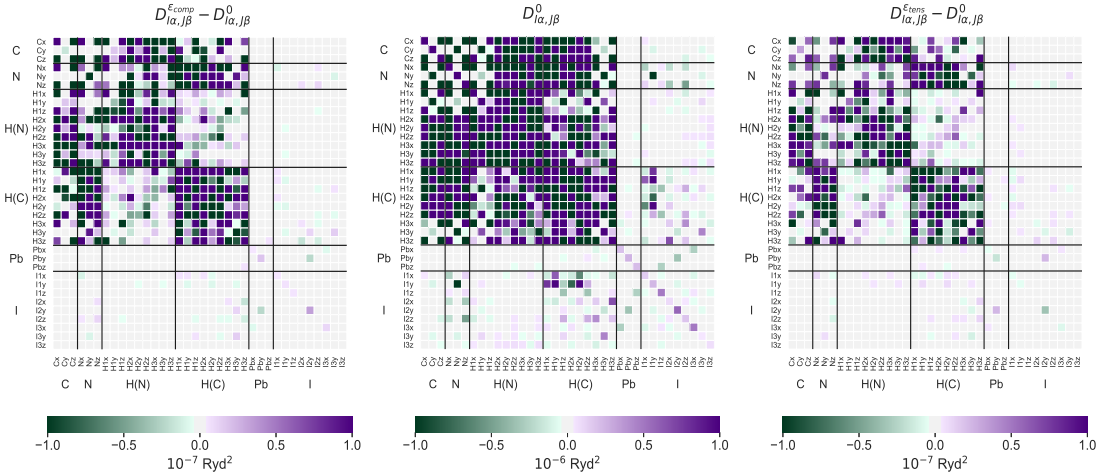

(a) (b) (c)

Figure 2.7: Dynamical matrix for strain along [010] direction. (a) Change in dynamical matrix for compressive strain ($\epsilon = -0.004$). (b) Dynamical matrix at zero strain. (c) Change in dynamical matrix at tensile strain ($\epsilon = 0.004$). Symbols in both the axes represent atoms and their coordinates. For example, within H(N) block, H3z denotes the z coordinate of the third H attached to N.

2.4.3 Change in dynamical matrix due to uniaxial strain.

To understand the different behaviors of the phonon modes under strain, we have analysed the dynamical matrix of each strained structure according to Section 2.2.

We have calculated the changes in dynamical matrices and plotted the results as heat-maps in Fig. 2.7(a) and 2.7(c) to understand which changes in interatomic interactions are most significant for the vibrational frequency changes under strain and how they relate to the different linear/parabolic/irregular pattern observed. Fig. 2.7(b) shows the dynamical matrix for the unstrained lattice. Note that these plots are symmetric about the diagonal and the scales are different for the strained and non-strained cases. The largest elements are in the C, N, H block due to lighter masses (see Eqn. 2.2). Diagonal elements are generally larger than off-diagonal elements, as can be seen at Fig. 2.7(b). It can be also seen that changes due to compressive strain are more than those of tensile strain, which can be understood based on the typical curve of energy *vs.* bond length, *e.g.* the Morse potential. Since Pb and I are heavier than C, N and H, Pb-I interactions will be significant most for low frequency modes. It can be noticed that there are very small interactions between H atoms and their nearest Pb or I atoms (Fig. 2.7(b)) which gives an indication that van der Waals interactions are of minor importance for vibrations of the cubic structure which is also supported by a previous study.[64] We have calculated also the dynamical matrix for a $2 \times 2 \times 2$ supercell, and found that the matrix elements are significantly smaller when the two atoms are in different primitive cells. This indicates that the artificial long-range order in our periodic structure does not make much difference in the vibrational properties compared to the true dynamical disorder.

From the change in dynamical matrix in Fig. 2.7(a) and Fig. 2.7(c), we can see that the component of Pb-I interactions change most when it is parallel to the direction of strain. For example, the Pb_y-I_y interaction changes most for [010] strain whereas Pb_x-I_x and Pb_z-I_z interactions change most for [100] and [001] strains respectively (Fig. 2.13-2.14). We have already seen in the structural changes that Pb-I bond length is affected most when the stretches are along the direction of polarization of the bond. It is clear from Fig. 2.7(a) and Fig. 2.7(c) that Pb-I modes are significantly affected due to strain. It can also be seen that I-N coupling (lower left and upper right) is important and greater than I-C coupling which is due to the electrostatic interaction between the MA ion and the cage. These interactions play a significant role in the frequency shifts and are important for the medium and high frequency regions.

Given the success of analyzing vibration separately[106] (lattice and ion), one might think that the lattice strain will not affect the MA ion, but this turns out not to

be true. Among the hydrogens attached to C, or the hydrogens attached to N, there are significant changes with strain in the interactions, which explain the behaviors of some of the high frequency modes. Modes that have a large component of C-H, N-H stretch have higher slopes in the high frequency region, whereas in the low frequency region large Pb-I stretch or bend with C-H, N-H stretch is associated with large slope. C-H, N-H asymmetric stretch or CH_3NH_3 spin and torsion are found to have high slopes. It is found that slope values are high in the low and high frequency region and small in the medium frequency region. It is also found that the slope values are typically higher when the strain is perpendicular to the direction of the MA ion (along [010] and [001]) and lower when its along the direction of the MA ion *i.e.* along [100]. We attribute this asymmetry to the orientation of the C-H bonds: two of the C-H and N-H bonds lie closer to [010] than to [100], giving greater effects from [010]; one C-H and one N-H bond lie parallel to [001], and these bond lengths are affected most by [010], and also show the greatest effects of any C-H or N-H bonds in any strain direction (Fig. 2.20, 2.19). Therefore the strain effects on the MA ion, and its interactions with the cage, are greatest when we apply strain along [010] and [001].

IR and Raman intensities are much higher in the high frequency region than in the low or mid-frequency regions, and are mainly contributed by C-H and N-H stretches. From our full phonon analysis, shown in Table 2.7, we found that low-frequency modes are mainly due to Pb-I-Pb vibration with translation or libration mode of the MA ion. The mid-frequency modes mainly consist of C-H and N-H asymmetric bending with some spin or twist. The high-frequency modes are mainly symmetric and asymmetric stretch of C-H and N-H bonds of the methylammonium ion. For all the modes, IR intensity vectors are lying in the plane, either in xz (100) or in xy (001) plane. Modes which have high slopes in all three directions – among them, high frequency modes (3053.38 cm^{-1}, 3058.42 cm^{-1}, 3161.71 cm^{-1}) – are both highly IR- and Raman-active while low frequency modes (27.97 cm^{-1}, 65.02 cm^{-1}, 85.82 cm^{-1}) are less IR- and Raman-active. Modes involving libration and translation of the $CH_3NH_3^+$ ion and Pb-I-Pb bending have high slopes along [100] direction while modes having high slope in [010] show C-H and N-H stretch in $CH_3NH_3^+$ ion.

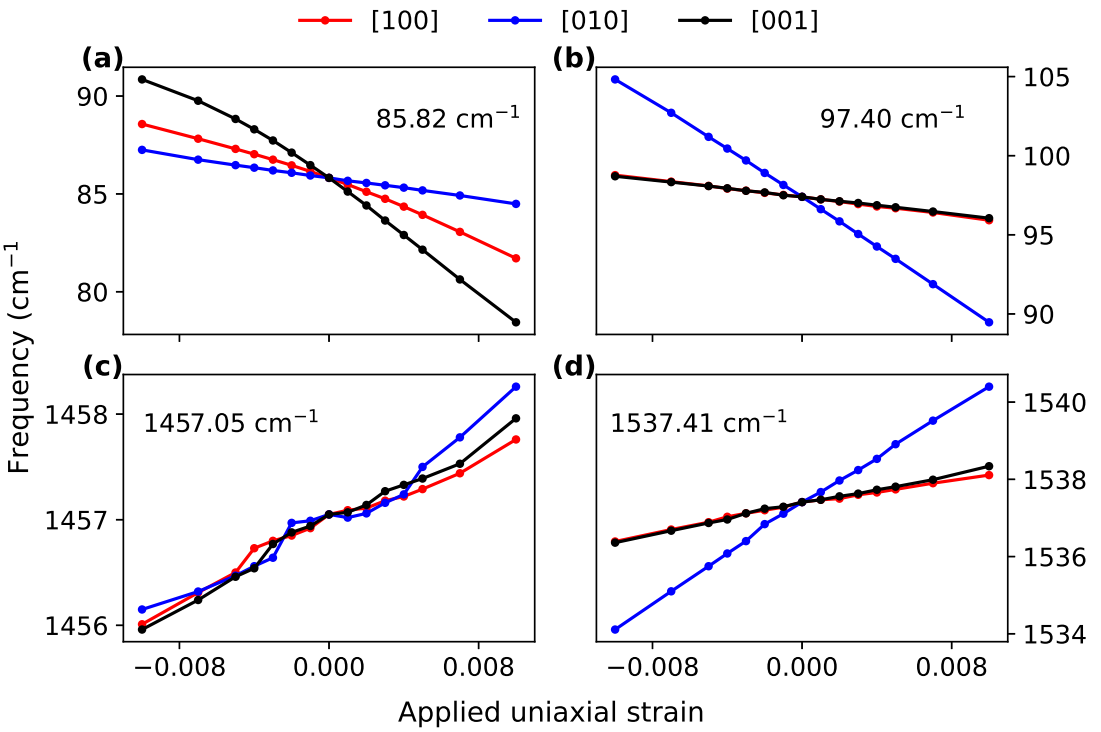

Figure 2.8: Frequency *vs.* strain for the best modes for IR/Raman microscopy to probe local strain, showing linear changes for robust calibration.

2.4.4 Best modes to probe local strain in cubic $CH_3NH_3PbI_3$

An appropriate mode for strain mapping with IR/Raman microscopy should have i) a large IR or Raman intensity, for ease of detection; ii) a linear frequency change with strain, for simple and unique relation of frequency to strain; iii) a large slope for frequency *vs.* strain, for sufficient signal-to-noise ratio in measuring frequency shifts; and finally, iv) a small change in frequency with respect to cation orientation, ensuring the validity of our results in the presence of cation rotations at elevated temperature.[27]

A difficulty in checking these frequency changes with cation orientation is that phonon calculations are not very meaningful except from a relaxed structure, and only a few cation orientations are stable.[15, 152] We took our zero-strain structure and rotated the cation close to the [111] direction, and relaxed the structure. The result is 0.01 eV higher in energy, and has the cation in the xz plane, with the C-N bond at an angle of 113.9° (compared to 23.3° for our main data set) with respect to [100] direction. From a phonon calculation, we find some mode frequency changes due to the $CH_3NH_3^+$ rotation,

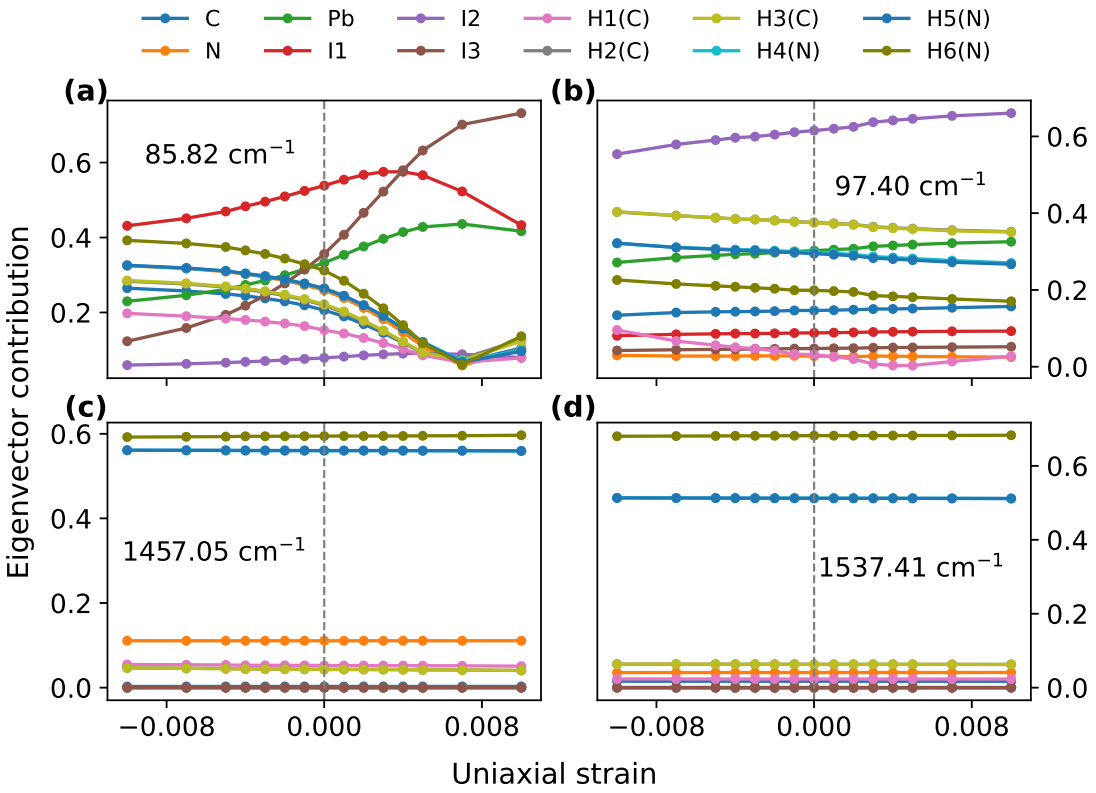

Figure 2.9: Mode eigenvector *vs.* strain for the best modes for IR/Raman microscopy to probe local strain, showing little change in mode character (except for (a)), associated with robust linear changes *vs.* strain.

typically by a few wavenumbers. We may expect this variation to be a contribution to heterogeneous broadening of Raman peaks as ions rotate thermally. Indeed Nakada *et al.* report larger peak widths for high- and low-frequency modes than for mid-frequency modes, for all 3 crystal phases,[92] in accordance with our results for frequency changes with ion rotation. The high- and low-frequency modes change most while the mid-frequency modes change less due to the $CH_3NH_3^+$ rotation. This is because the mid-frequency region is mainly symmetric/asymmetric bending modes of the MA ion which are not affected much by rotation of the MA ion, whereas stretching modes at high and low frequency are the ones that change more when the distances change between the MA ion and the Pb-I cage. For this reason, the same modes that have large frequency changes with ion rotation have large slopes with strain. Full results are shown in Table 2.7. If the mode frequency changes by a significant amount due to rotation of the molecule, our

static result may have a larger error, and the predicted frequency shifts due to strain will be less reliable. Therefore, we need to focus on those modes for which frequency change due to rotation of the MA ion is minimal.

After this analysis, we can identify the best modes for IR or Raman microscopy for probing local strain.[22, 134] We note 4 suitable modes, whose properties are detailed in Table 2.3 and whose displacement patterns are shown in Fig. 2.15. A combination of all 4 modes can be used together for better precision, or even to find a best fit to 3 directions of uniaxial strain. Two are low-frequency Pb-I modes and two are mid-frequency molecular modes. The frequency changes *vs.* strain are shown in Fig. 2.8 and the eigenvectors *vs.* strain are shown in Fig. 2.9, exhibiting little change in mode character and a robust linear frequency change. Each of these modes has all slopes positive or all slopes negative. In the case of triaxial strain or when cation rotations wash out directional dependence, the average of the three uniaxial slopes would be the appropriate slope according to Eq. 2.6. Having all uniaxial slopes with the same sign is convenient, because the three directions will reinforce each other rather than cancelling out, as could happen when the slopes have different signs. The IR and Raman intensity for these 4 modes show only moderate changes with strain (Fig. 2.16-2.18) as for c-Si optical modes,[22] which we expect would not cause any problem for experimental measurement. We find another mode at 1365.3 cm^{-1} that has favorable properties with reasonable Raman intensity to probe local strain (Fig. 2.27-2.33); however it is not observed in experiment. The reason may be limitations of our model. Our structure is pseudocubic rather than cubic, and our calculation is static and done at 0 K at which this is not the stable phase. As a result, this mode may in fact lose its Raman activity due to dynamic average symmetry in the real high-temperature structure.

There is a final point to consider in assessing experimental feasibility. To be able to measure strain by Raman shifts, we need to obtain a frequency shift that is higher than the experimental resolution. For typical strain[29, 161] of 1% we can expect to obtain shifts -3.8 cm^{-1}, -3.5 cm^{-1}, 0.75 cm^{-1} and 1.57 cm^{-1} for the favorable Raman modes at 85.8 cm^{-1}, 97.4 cm^{-1}, 1457.1 cm^{-1} and 1537.4 cm^{-1}, respectively based on the average slopes in Table 2.3. Experimentally measured full widths at half maximum (FWHMs) for Raman spectra[111, 82, 92] around the low-frequency modes are 8 cm^{-1}, 10 cm^{-1}, and 18 cm^{-1}, and for the mode at 1460 cm^{-1}, the FWHM is around 35 cm^{-1}. One contribution to FWHM can be strain itself – inhomogeneous strain distributions within

the Raman focus will result in broadening.[154] Although these FWHMs are high, peak shifts can be resolved less than 1 cm^{-1}, as seen for the temperature-dependent Raman shifts measured by Nakada *et al.*[92] and in Strubbe *et al.*[134] on a-Si:H, because fitting of Gaussian peaks allows determination of differences in peak centers to much greater precision than the FWHM. Temperature dependent frequency shifts were measured for MAPI by Nakada *et al.*[92] and they were able to measure shifts less than 1 cm^{-1} which is well within the expected shifts from 1% strain in case of our cubic structure. One contribution to the temperature-dependent frequency shift is thermal expansion which is a sign of significant effect of anharmonicity. Our results show that this is a relatively minor contribution because our predicted shifts due to thermal expansion are much less than the shifts reported by Nakada *et al.*,[92] in accordance with results of Bonini *et al.* for graphite.[13]

Finally, note that the deviation between calculated and measured frequencies for these modes is larger than expected strain shifts. Due to this unavoidable systematic difference, we would recommend use of our calculated slopes to infer relative strains in a sample, rather than by direct comparison of experimental frequencies to our calculated frequencies.[134]

2.4.5 Calculation of mode Grüneisen parameter

The uniaxial mode Grüneisen parameter is calculated using the slope of the frequency vs strain curve for each mode (Fig. 2.10), as done in a-Si.[134] Pb-I vibrations at lower frequency have significant values, whereas $CH_3NH_3^+$ ion vibrations at higher frequency have much smaller values. One of the reasons for the low values at high frequency is the high frequency itself, as we divide the slope with the mode frequency, although some high-frequency modes do have large absolute slopes. To connect to macroscopic properties, we calculate the Grüneisen parameter, as the weighted average over all the modes using the Bose-Einstein formula for heat capacity. In distinction to F. Brivio *et al.*,[15] we are using uniaxial strain, and we include only modes at $q = \Gamma$, because of the conceptual problem in the quasiharmonic approximation of how to handle the imaginary frequencies.[23] Also, due to dynamical disorder [76], which is not included in our calculation, the phonon bandstructure away from $q = \Gamma$ may be less accurate or lose some of its meaning without periodicity. The imaginary frequencies are indicative of the fact that the cubic structure is not the most stable phase at $T = 0$, and were observed

Table 2.3: Best modes for IR or Raman microscopy to probe local strain.[a]

Calc. Freq. (cm^{-1})	**Expt. Freq. (cm^{-1})**	**IR Int.**	**Raman Int.**	**Avg. slope (cm^{-1})**	**Slope [100] (cm^{-1})**	**Slope [010] (cm^{-1})**	**Slope [001] (cm^{-1})**	**Mode Characters**
85.8	86.68[111]	4.77	193.2	-379.87	-334.8	-127.8	-677.0	$CH_3NH_3^+$ libration $CH_3NH_3^+$ translation Pb-I-Pb bending Pb-I asym. stretch
97.4	94.0[82] 98.0[92]	5.53	20.2	-348.77	-140.8	-772.7	-132.8	$CH_3NH_3^+$ libration, spin Pb-I-Pb bending
1457.1	1460.0[92]	5.65	138.9	75.5	63.2	74.8	88.5	C-N stretch N-H sym. bending C-H asym. bending no Pb-I vibration
1537.4	1582.0[92]	7.48	15.6	157.33	79.2	302.3	90.5	C-H asym. bending N-H asym. bending no Pb-I vibration

[a] Absolute IR intensity is in $(D/Å)^2$/amu and Raman intensity in $Å^4$/amu.

in previous work.[15] They occur around q=R and q=M, and are not reduced by strain (Table 2.8). Our calculated values of the directional Grüneisen parameter at 330 K (the transition temperature to tetragonal) for strain along [100], [010], and [001] are 1.06, 2.10, and -0.51, respectively, for an average of 0.88. The isotropic value reported by F. Brivio *et al.*,[15] averaged over temperature, was 1.6. We expect the difference is due to the handling of Brillouin zone integration, as well as their calculation via quasiharmonic thermal expansion rather than mode Grüneisen parameters. This result shows a directional dependency of the Grüneisen parameter that suggests an unusual negative thermal expansion along [001] direction for cubic MAPI, due to the negative value. While the existence of cation rotations at 330 K experimentally complicate the physical interpretation of this result, it connects to previous studies reporting that tetragonal perovskites have a negative thermal expansion coefficient along the [001] or c-axis,[40, 55] which is perpendicular to the direction of polarization of the $CH_3NH_3^+$ ion and also the largest lattice vector, in both cubic and tetragonal structures.

2.5 Conclusion

We have comprehensively studied the structural and vibrational properties of cubic $CH_3NH_3PbI_3$ under uniaxial strain. By analysing the dynamical matrix of the

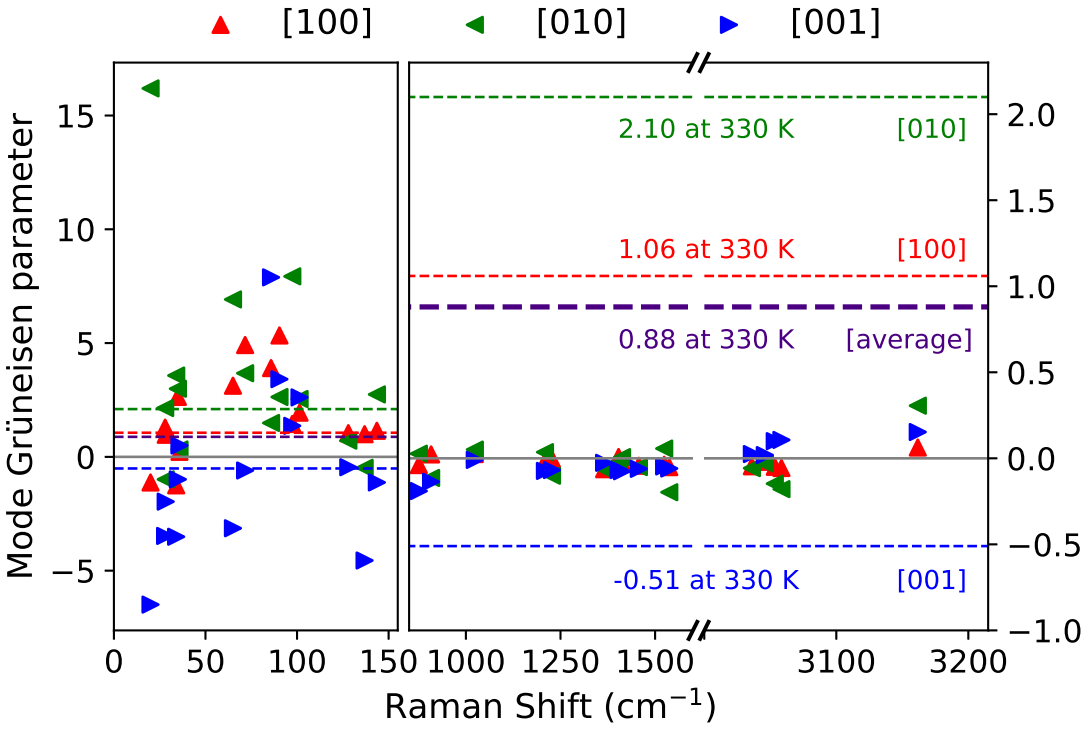

Figure 2.10: Calculated uniaxial mode Grüneisen parameters using slopes of the frequency vs strain graph for each mode in three different crystallographic directions. Dashed lines in red, green and blue represent Grüneisen parameter calculated at 330 K for different uniaxial directions. Thick dashed line in violet represents the average Grüneisen parameter.

system under each strain we are able to identify the interactions which contribute significantly to the frequency changes due to applied strain. The phonon modes have frequency changes under strain, which can show linear, parabolic, or irregular patterns. Linear is associated with change in dynamical matrix but no change in mode eigenvector with strain, while parabolic is associated with changes in both dynamical matrix and mode eigenvector, in accordance with a perturbative analysis. Irregular patterns are due to large changes in mode eigenvector due to discontinuous structural changes, which are a sign of anharmonicity. These changes give insight into the interplay between structure, strain, and vibrations, and show approximate symmetries for some modes. We find that not only the Pb-I bond lengths but also the Pb-I-Pb bond angles change under strain, showing a buckling of the Pb-I lattice. Decrease in N-H bond length under compressive

strain may be connected to the increased stability under compressive strain. We also find that the cation rotates with respect to the lattice under strain. We have identified 4 modes that are promising for IR or Raman microscopy measurement of local strain, as done in other semiconductors and even amorphous Si which has broad peaks. Results on the mode Grüneisen parameters and macroscopic Grüneisen parameters give insight into anharmonicity and directional negative thermal expansion. Our study of the cubic phase is relevant not only to high temperatures but also to cubic phases stabilized by ligands or other cations. Our results are expected to be similar in many respects to results for the tetragonal and orthorhombic phases, particularly in the mid-frequency range where the spectra are similar, and these phases will be the subject of future publications. We look forward to experimental work to confirm these results with uniform strain, and employ our calibration for strain mapping. Our work opens the way for a standard bench-top characterization method to be usable for analyzing the critical role of local strain in hybrid perovskite photovoltaics.

2.6 Acknowledgement

We acknowledge a helpful discussion with Yong Zhang. Work was supported by UC Merced start-up funds and the Merced nAnomaterials Center for Energy and Sensing (MACES), a NASA-funded research and education center, under award NNX15AQ01. This work used computational resources from the Multi-Environment Computer for Exploration and Discovery (MERCED) cluster at UC Merced, funded by National Science Foundation Grant No. ACI-1429783, and the National Energy Research Scientific Computing Center (NERSC), a U.S. Department of Energy Office of Science User Facility operated under Contract No. DE-AC02-05CH11231.

2.7 Supplementary Information

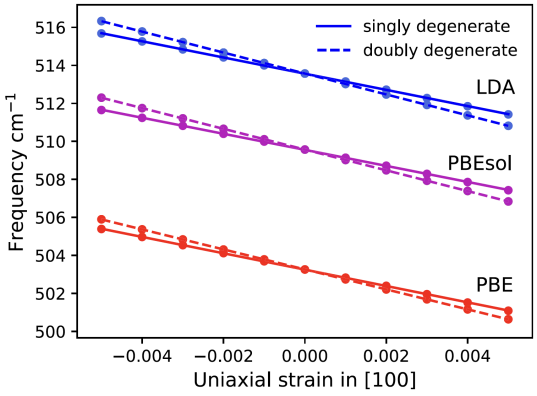

Figure 2.11: Benchmark calculation of the change in optical phonon frequency of c-Si under uniaxial strain along [100], with different DFT functionals. Applied strain breaks the degeneracy of the phonon mode making doubly degenerate (dotted) and singly degenerate (solid) modes.

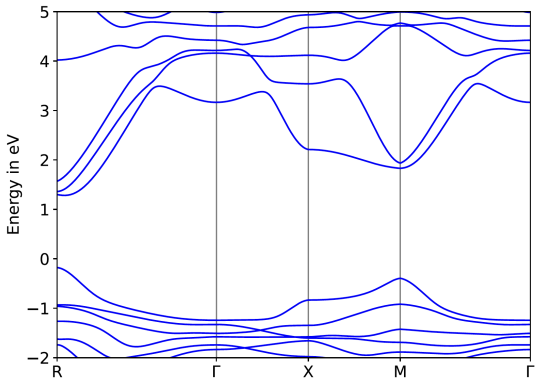

Figure 2.12: Bandstructure for cubic $CH_3NH_3PbI_3$ using LDA.

Table 2.4: Bandgap at different k-points using different functionals.

Functional Used	Bandgap in eV	
	R	M
LDA	1.478	2.225
PBE	1.769	2.353
PBEsol	1.525	2.217

Table 2.5: Relaxed structure parameters for cubic $CH_3NH_3PbI_3$ using different functionals. Lattice parameters and bond lengths in Å and angles in degrees

	a	b	c	α	β	γ	Pb-I	Pb-I-Pb	C-H	N-H	C-N
							3.250				
							3.078	165.151	1.099	1.047	
Initial Structure	6.288	6.228	6.374	90.003	88.744	89.986	3.215	167.237	1.100	1.047	1.481
							3.174	172.011	1.100	1.042	
							3.140				
Functional											
							3.090				
							3.120	163.458	1.101	1.048	
LDA	6.163	6.115	6.267	90.004	88.803	89.998	3.173	164.652	1.101	1.048	1.471
							3.156	173.920	1.100	1.043	
							3.090				
							3.046				
							3.444				
							3.227	166.715	1.093	1.038	
PBE	6.499	6.41	6.532	90	88.657	90.001	3.227	169.170	1.093	1.037	1.493
							3.075	171.133	1.093	1.038	
							3.328				
							3.234				
							3.146				
							3.146	166.527	1.099	1.044	
PBEsol	6.291	6.248	6.378	89.999	88.645	90	3.238	168.411	1.099	1.041	1.482
							3.085	172.732	1.098	1.044	
							3.220				
							3.171				

Table 2.6: Benchmark calculation of optical phonon mode frequencies at q = 0 for c-Si, and the split singlet and doublet slopes under uniaxial [100] strain using LDA, PBE and PBEsol. Calculated values are compared with published theoretical and experimental results. LDA has best agreement with experiment.

Method	lattice constant Å	ω cm^{-1}	singlet slope cm^{-1}	doublet slope cm^{-1}
LDA	5.394	514	-426	-551
PBE	5.469	503	-430	-526
PBEsol	5.431	510	-422	-546
LDA[134]	5.38	514	-424	-547
Exp't	-	520±0.584[100]	-481±20[2]	-601±20[2]

Table 2.7: Complete phonon mode analysis at q=0 for cubic CH3NH3PbI3. Here IR intensity is in (D/Å)2/amu units and Raman intensity is in $Å^4$/amu units as given by Quantum ESPRESSO. $\Delta\omega$ denotes change in frequency due to rotation of the CH_3NH_3 cation inside the Pb-I cage. Raman shift pattern includes all three directions [100], [010], and [001].

Mode	Freq. (cm^{-1})	IR Int.	Raman Int.	Depol. ratio	CH_3NH_3 vibration	Pb-I cage vibration
4	20	0.19	15.25	0.75	translation	Pb-I-Pb bending
5	27.97	0.16	303.36	0.15	libration	Pb-I-Pb rock
6	28.3	0.42	133.24	0.32	libration, translation	Pb-I-Pb bend
7	34	0.22	22.73	0.74	translation	Pb-I-Pb rock
8	34.92	0.1	142.34	0.13	translation	Pb-I-Pb rock
9	35.81	0.44	438.19	0.74	libration, translation	Pb-I-Pb rock
10	65.02	0.47	18.64	0.32	libration, asym bend	no vibration
11	71.65	0.87	3.42	0.75	libration, asym bend	Pb-I-Pb bending
12	85.82	4.77	193.24	0.75	libration, translation	Pb-I-Pb bending Pb-I asym stretch
13	90.4	6.13	72.27	0.58	libration, translation	Pb-I-Pb rock, Pb-I stretch
14	97.4	5.53	20.2	0.75	libration, spin	Pb-I-Pb bending
15	101.37	0.46	20.37	0.26	translation	Pb-I-Pb rock (only I)
16	128.01	0.94	28.75	0.64	libration, asym bend	no vibration
17	136.9	0.08	26.56	0.75	spin	no vibration
18	143.6	1.81	1.1	0.75	libration, asym bend	no vibration
19	312.59	0.01	38.31	0.75	twist, spin	no vibration
20	875.68	1.39	535.87	0.75	asym bend	no vibration
21	908.09	1.57	9.96	0.75	asym bend	no vibration
22	1023.57	0.25	85.7	0.45	symm bend, C-N stretch	no vibration
23	1208.95	0.59	629.1	0.73	Libration, asym bend	no vibration
24	1227.42	0.05	19.45	0.75	libration, asym bend	no vibration
25	1365.29	0.53	222.7	0.72	C-N stretch C-H symm bend	no vibration
26	1403.54	0.94	82.24	0.75	C-H, N-H asym bend	no vibration
27	1412.6	0.28	77.6	0.69	C-H, N-H asym bend	no vibration
28	1457.05	5.65	138.87	0.62	C-N stretch, N-H symm bend, C-H asym bend	no vibration
29	1523.94	3.74	198.71	0.57	C-H, N-H asym bend	no vibration
30	1537.41	7.48	15.64	0.75	C-H, N-H asym bend	no vibration
31	2943.14	0.11	1603.63	0.04	C-N stretch, C-H, N-H symm stretch	no vibration
32	3036.04	3.48	1128.95	0.75	C-H, N-H asym stretch	no vibration
33	3045.84	0.4	1394.65	0.73	C-H, N-H asym stretch	no vibration
34	3053.38	15.1	4577.19	0.59	C-H, N-H asym stretch	no vibration
35	3058.42	44.03	668.93	0.75	C-H, N-H asym stretch	no vibration
36	3161.71	12.7	2757.26	0.51	C-H, N-H asym stretch, large N-H stretch	no vibration

Table 2.7: (continued).

Mode	Freq. (cm^{-1})	Slope [100]	Slope [010]	Slope [001]	Raman Shift Pattern	$\Delta\omega$
4	20	22.5	-323.83	129.83	linear	1.66
5	27.97	-108	-141.33	215.83	parabolic, mixed	2.19
6	28.3	44.5	109.33	-63	parabolic, mixed	-1.06
7	34	42.5	-121.5	125.33	linear	1.26
8	34.92	-92	-104.5	28.5	parabolic, mixed	1.58
9	35.81	-8	-11.67	-17.83	parabolic, mixed	-0.68
10	65.02	-203.33	-449.83	204	mixed	6.15
11	71.65	-352.17	-263.33	42.83	linear	5.63
12	85.82	-334.83	-127.83	-677	linear	1.51
13	90.4	-482.33	-237.83	-308.67	linear	-4.42
14	97.4	-140.83	-772.67	-132.83	linear	0.43
15	101.37	-197	-257.83	-264.83	mixed	-3.27
16	128.01	-133.33	-91.33	58.17	mixed	4.5
17	136.9	-136.5	65.83	623.5	mixed	13.04
18	143.6	-164.67	-394	161.33	linear	3.72
19	312.59	31	160	440	linear	7.13
20	875.68	34	-23.67	166.17	mixed	2.19
21	908.09	-20.67	103.67	123.5	linear	2.43
22	1023.57	-25.17	-52	9.67	mixed	0.08
23	1208.95	22.67	-43.83	88.17	linear	0.98
24	1227.42	6.17	123.67	83.83	linear	1.39
25	1365.29	85.67	84	34.83	linear	-0.73
26	1403.54	-11.5	44.17	95.83	linear	1.86
27	1412.6	33.67	-10.5	105.5	linear	1.36
28	1457.05	63.17	74.83	88.5	linear	0.01
29	1523.94	56.33	-87.33	72	linear	0.82
30	1537.41	79.17	302.33	90.5	linear	0.43
31	2943.14	103.17	77.5	-29.33	linear	-2.3
32	3036.04	140	172.17	-76.67	linear	-3.24
33	3045.84	61.83	88.67	-57.5	linear	-1.94
34	3053.38	148.67	449	-304.5	linear	-6.05
35	3058.42	170.83	547.67	-328.5	linear	-6.43
36	3161.71	-199.33	-966.67	-482.67	mixed	-4.15

Table 2.8: Comparison of phonon modes at q=0, R, and M. Modes at R and M are imaginary at zero strain condition, as well as under compressive and tensile strain at this level.

Mode No.	q=0 zero strain cm^{-1}	q=M zero strain cm^{-1}	q=R zero strain cm^{-1}	q=R comp. strain 0.004 cm^{-1}	q=R tensile strain 0.004 cm^{-1}
1	0	-17	-18	-18	-17.7
2	0	23.1	-8.2	-8.6	-7.6
3	0	27.1	33.2	33.4	33.1
4	20	28.5	38.2	38.2	38.1
5	28	35.2	40.5	40.9	40.2
6	28.3	35.5	43.8	43.8	43.7
7	34	46.9	63.4	64.6	62.9
8	34.9	65.9	71.6	73	70.5
9	35.8	73.3	79.7	80.2	78.9
10	65	82.1	83	84.8	81.5
11	71.7	85	88.5	88.7	88.3
12	85.8	87.8	103.1	103.9	102.5
13	90.4	105.9	106.5	107	105.9
14	97.4	117.9	117.2	118.3	116.1
15	101.4	124.9	127.2	127.8	126.7
16	128	126.7	128.3	129.1	127.6
17	136.9	138.2	140.6	141.1	140
18	143.6	150.3	149.4	150.1	148.9
19	312.6	315.7	313.5	313.3	313.6
20	875.7	877.5	872	871.9	872.1
21	908.1	911.5	909.4	909.4	909.4
22	1023.6	1022.9	1023.6	1023.7	1023.4
23	1209	1205.6	1205.9	1205.8	1206
24	1227.4	1232.1	1232.5	1232.5	1232.4
25	1365.3	1363	1365.1	1364.7	1365.3
26	1403.5	1403.7	1405.8	1405.8	1405.8
27	1412.6	1411.1	1412.1	1412	1412.2
28	1457.1	1454.7	1458.1	1457.9	1458.2
29	1523.9	1520.8	1525.5	1525.3	1525.7
30	1537.4	1540	1541.7	1541.4	1542
31	2943.1	2942.9	2942.9	2942.5	2943.4
32	3036	3038.5	3038.5	3038	3039
33	3045.8	3042.6	3042	3041.4	3042.3
34	3053.4	3048.5	3048.4	3047.9	3048.8
35	3058.4	3076.5	3074.8	3074	3075.2
36	3161.7	3161.1	3161.1	3162.2	3160.7

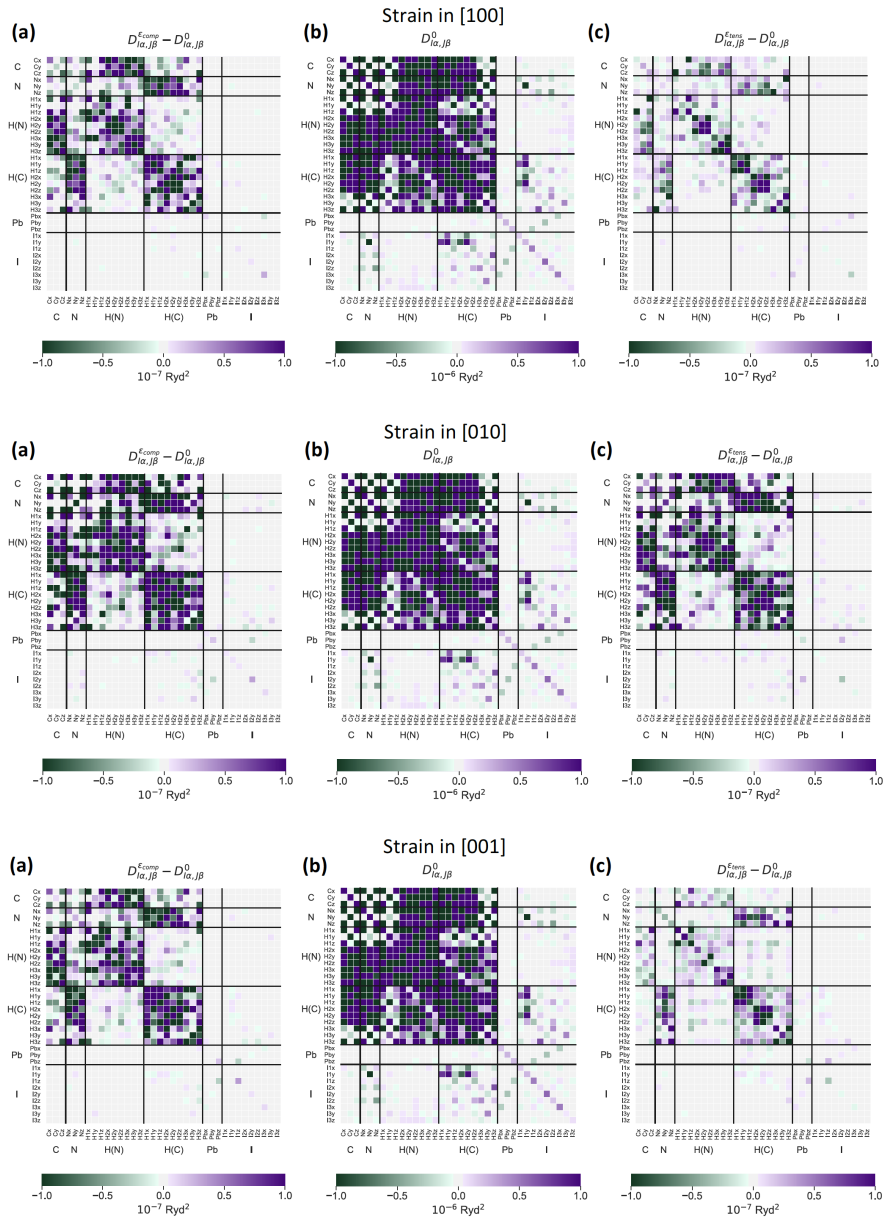

Figure 2.13: Dynamical matrix for strain along [100], [010] and [001] directions. (a) Change for compressive strain ($\epsilon = -0.004$). (b) Dynamical matrix at zero strain. (c) Change for tensile strain ($\epsilon = 0.004$). Symbols in both the axes represent atoms and their coordinates. For example, within H(N) block, $H3_z$ denotes the z coordinate of the third H attached to N.

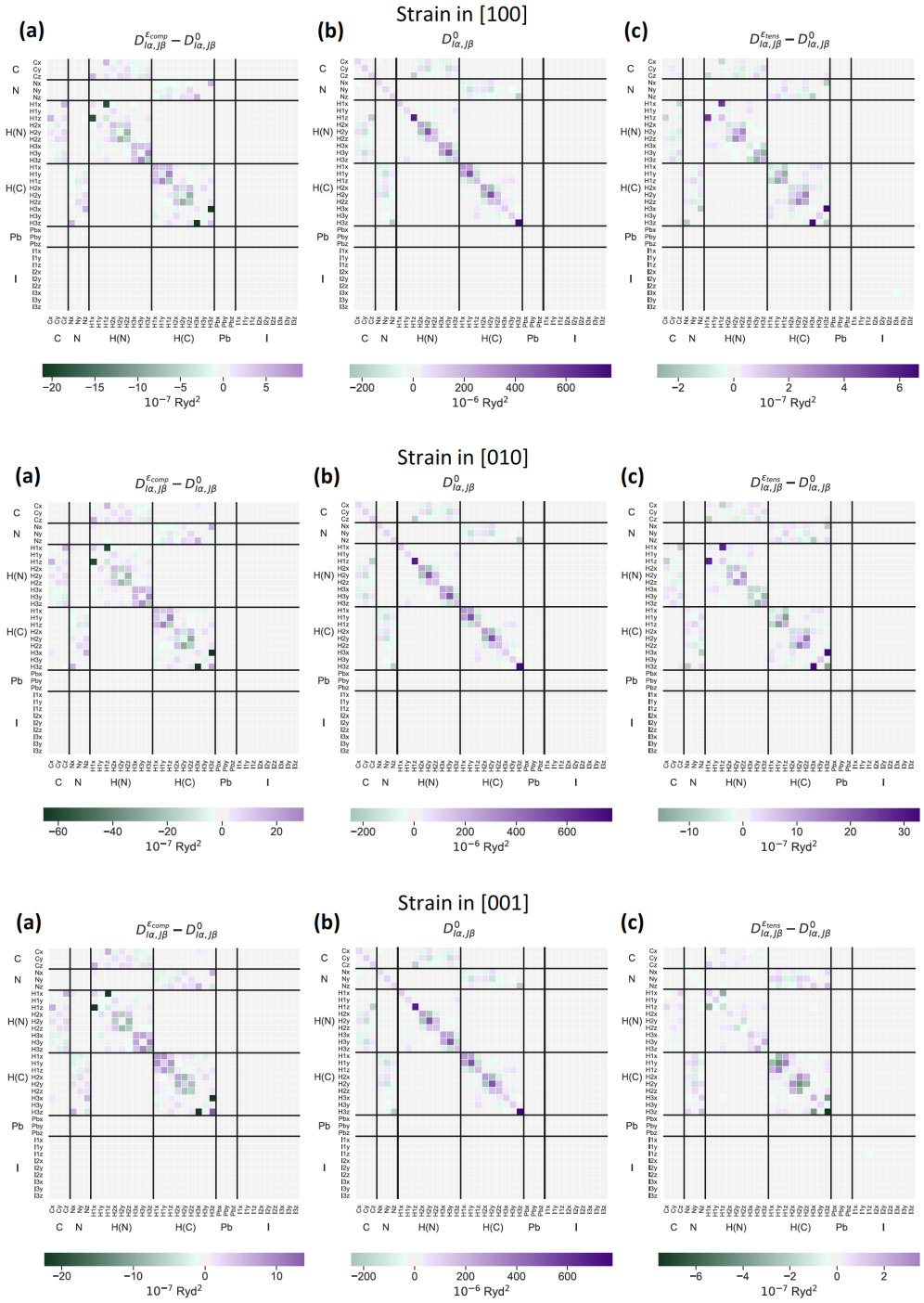

Figure 2.14: Same as Fig. 2.13 but with different scales to understand the changes in atomic interaction within the ion itself.

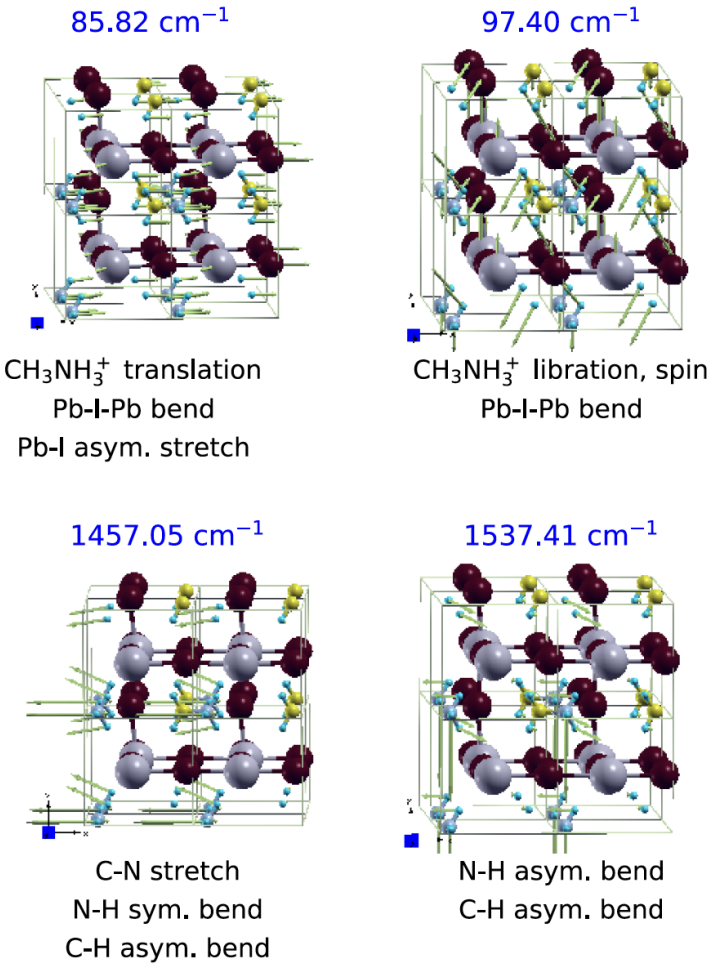

Figure 2.15: Displacement patterns for four most suitable modes to probe local strain with IR/Raman microscopy.

Table 2.9: Number of modes falling under different slope patterns for uniaxial strain along [100], [010] and [001].

slope character	non linear	step linear	linear with kinks	linear	parabolic
strain along [100]	0	0	8	21	4
strain along [010]	4	4	7	17	1
strain along [001]	2	1	9	21	0

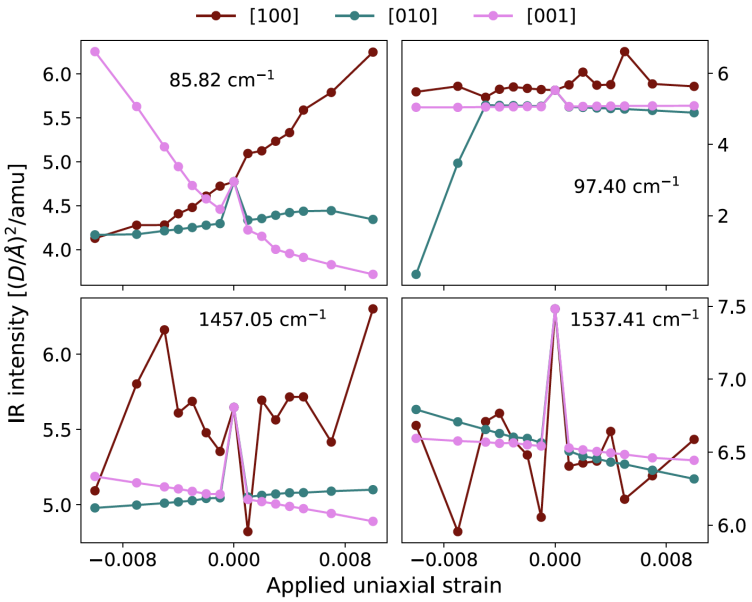

Figure 2.16: Change of IR intensity with uniaxial strain, for 4 best possible modes for experimental measurement.

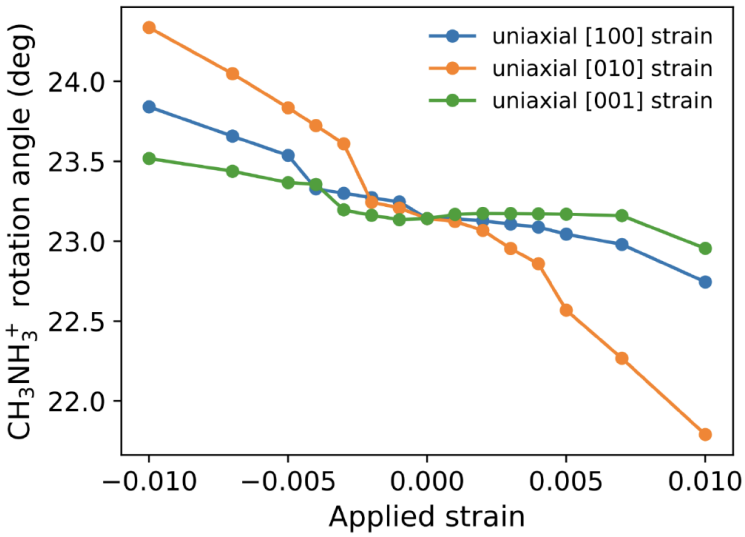

Figure 2.17: Change in orientation of the methylammonium ion. Angle is that between the C-N bond and the x-axis, [100] direction.

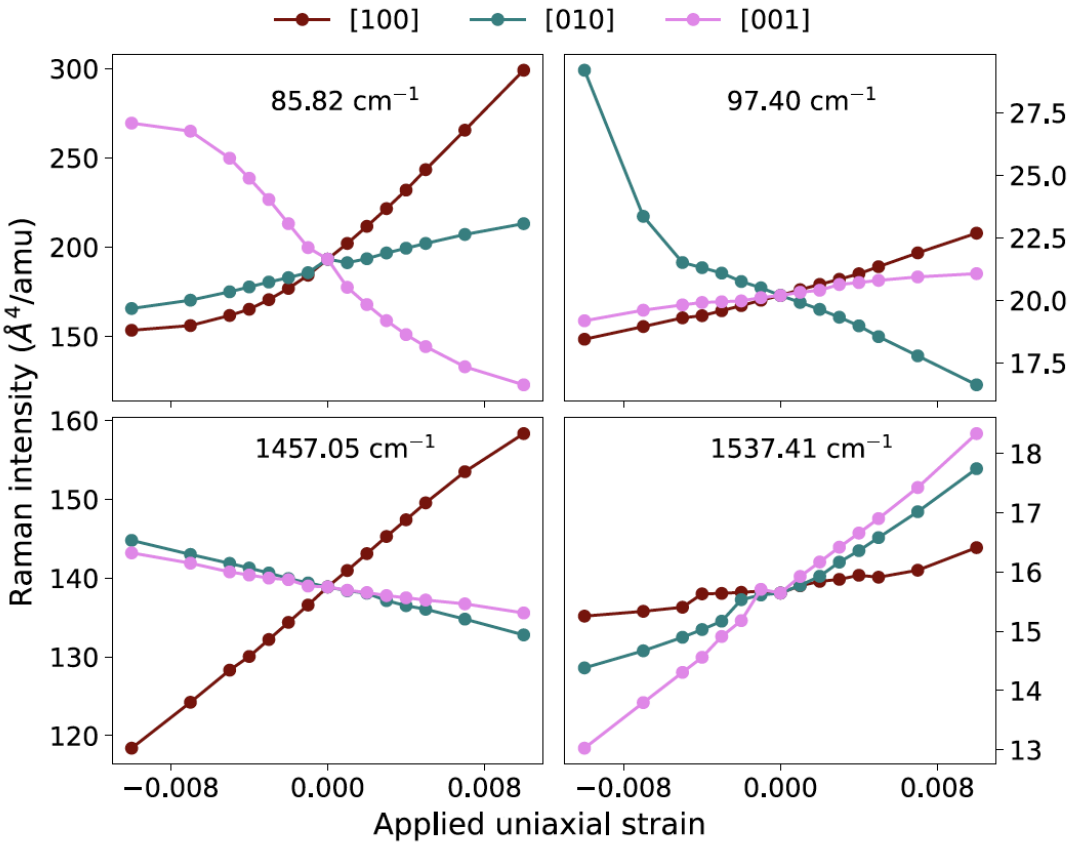

Figure 2.18: Change of Raman intensity with uniaxial strain for 4 best possible modes for experimental measurement.

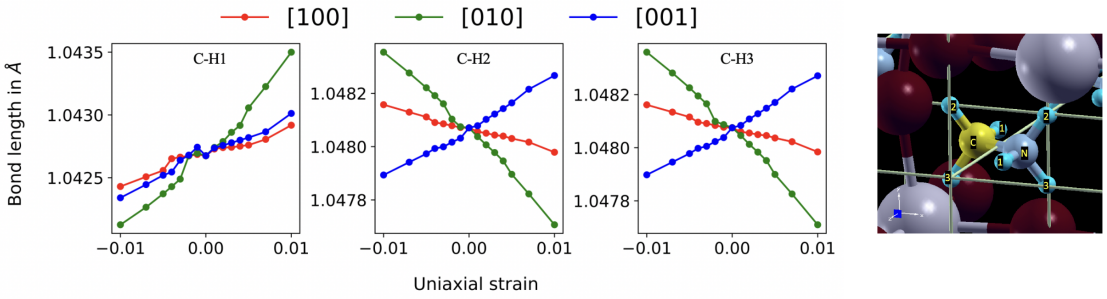

Figure 2.19: Change in C-H bond length due to uniaxial strain.

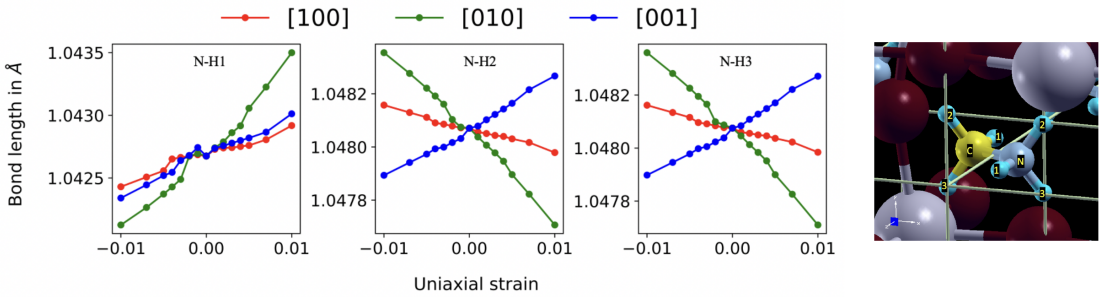

Figure 2.20: Change in N-H bond length due to uniaxial strain.

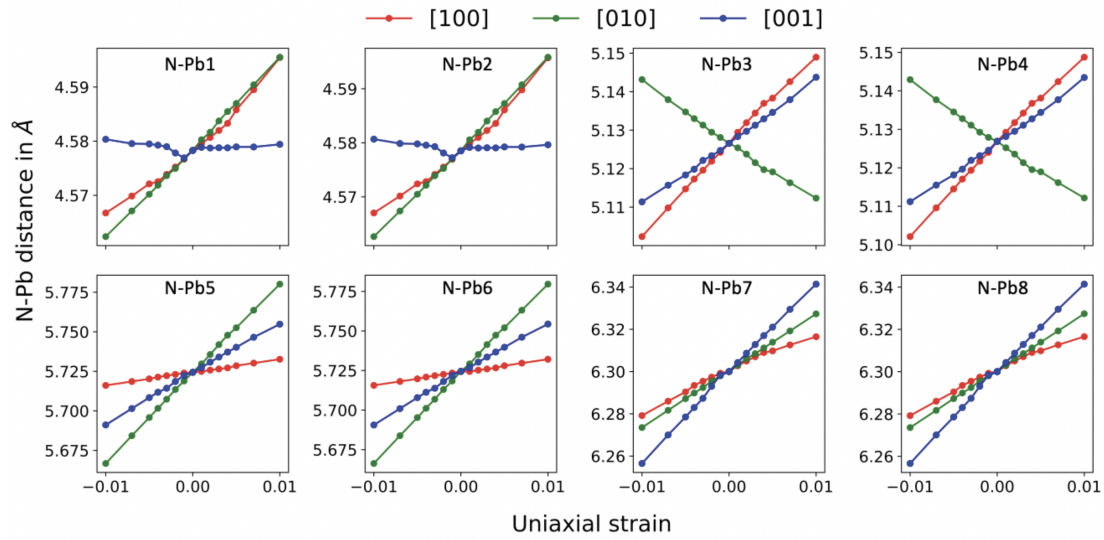

Figure 2.21: N-Pb distance changes due to uniaxial strain. Iodine atoms are numbered in ascending order of N-I distances.

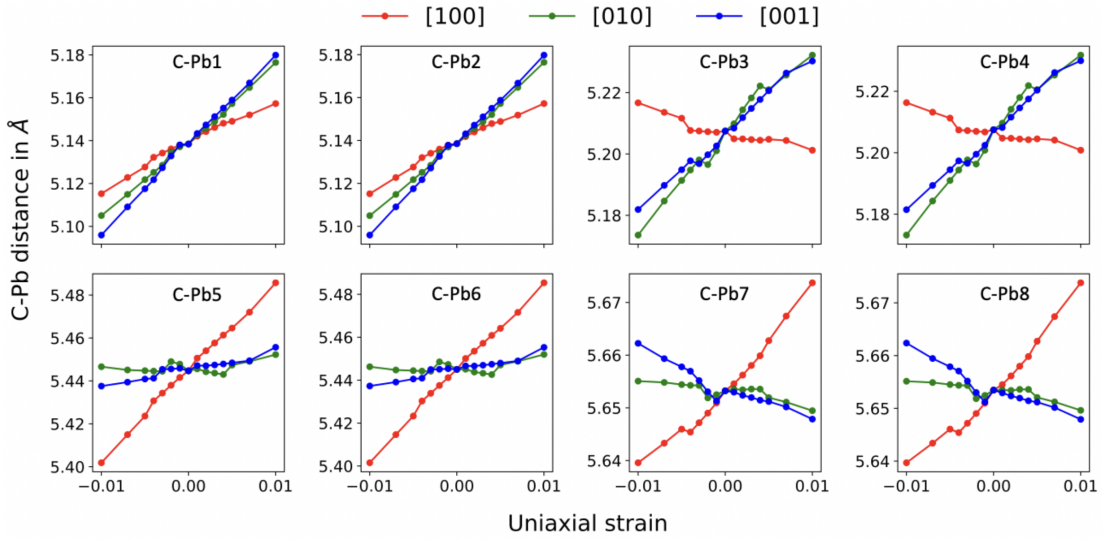

Figure 2.22: C-Pb distance changes due to uniaxial strain. Pb atoms are numbered in ascending order of C-Pb distances.

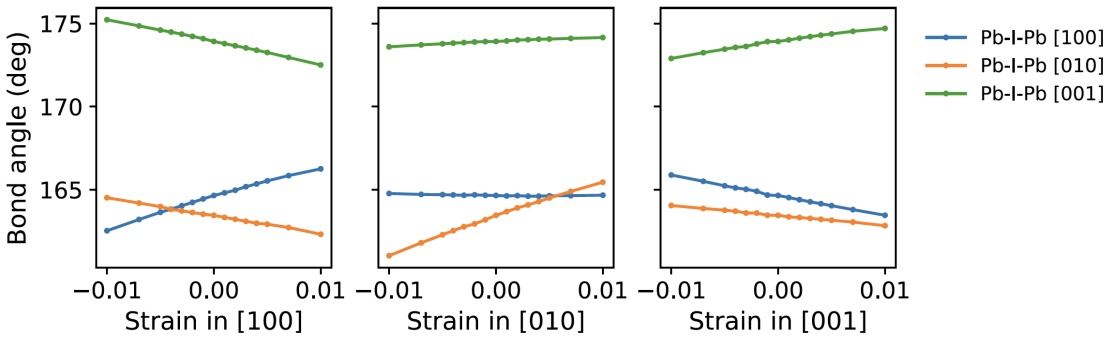

Figure 2.23: Pb-I-Pb bond angle changes due to uniaxial strain.

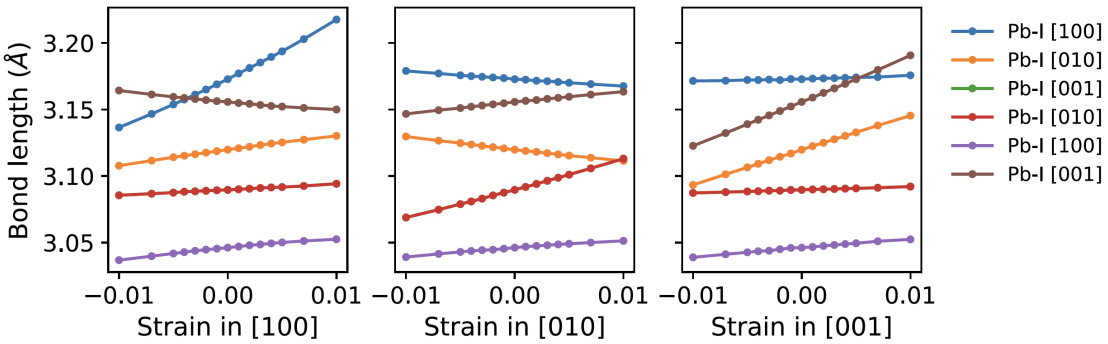

Figure 2.24: Pb-I bond length changes in each direction of uniaxial strain.

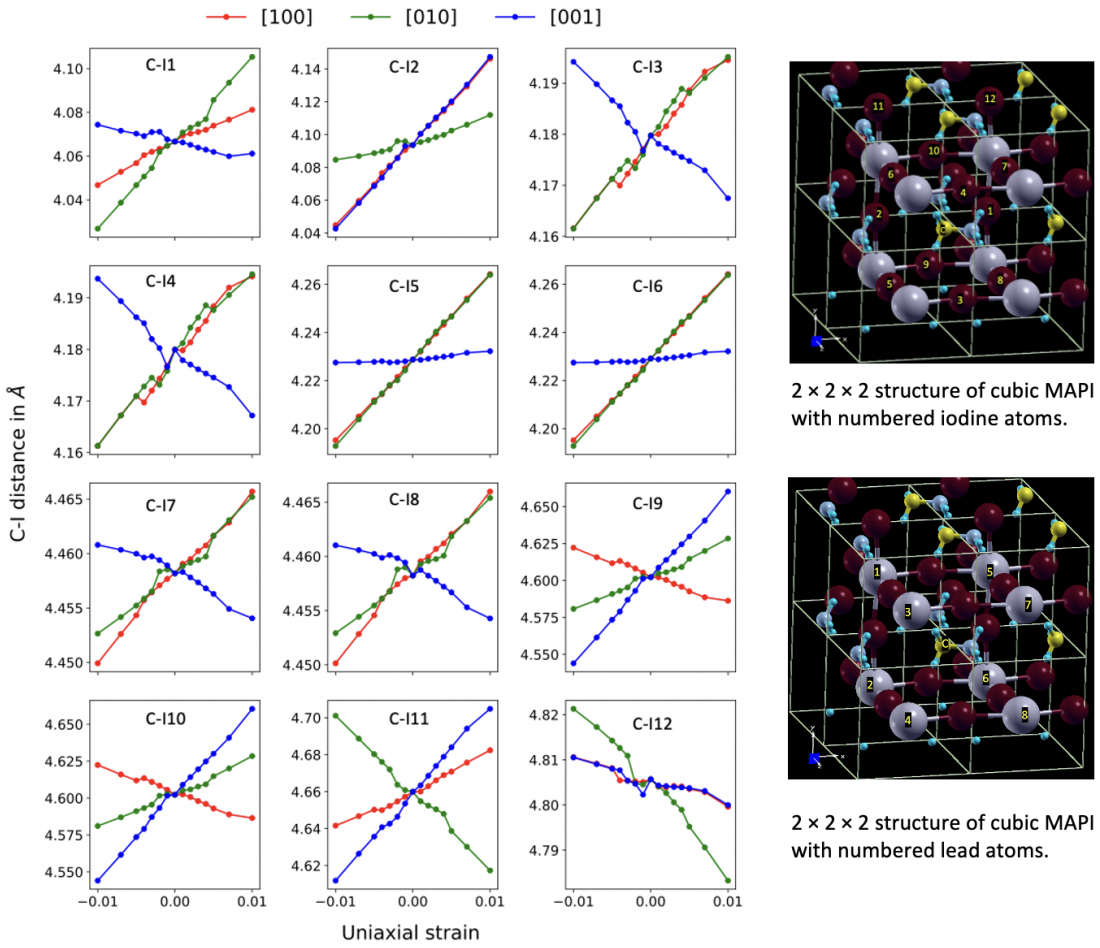

Figure 2.25: C-I distance changes due to uniaxial strain. Iodine atoms are numbered in ascending order of C-I distances.

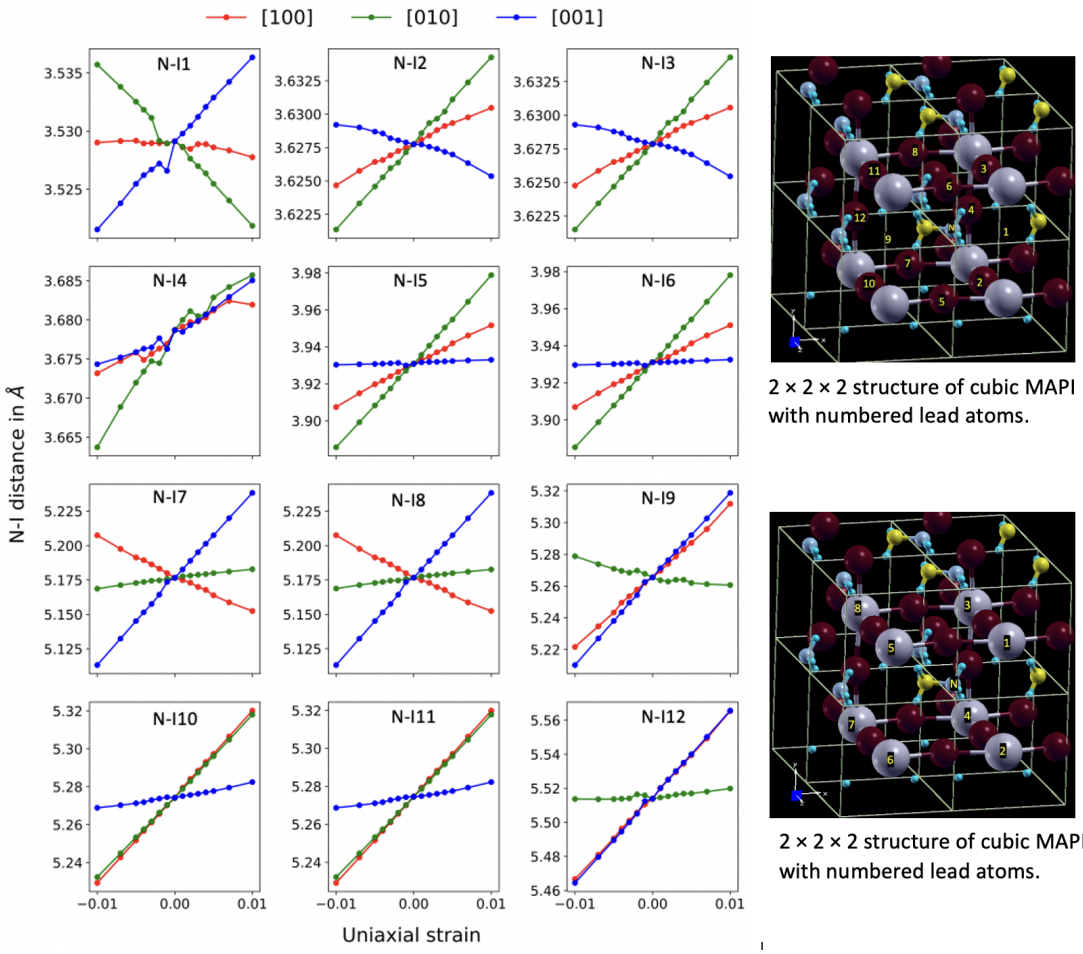

Figure 2.26: N-I distance changes due to uniaxial strain. Iodine atoms are numbered in ascending order of N-I distances.

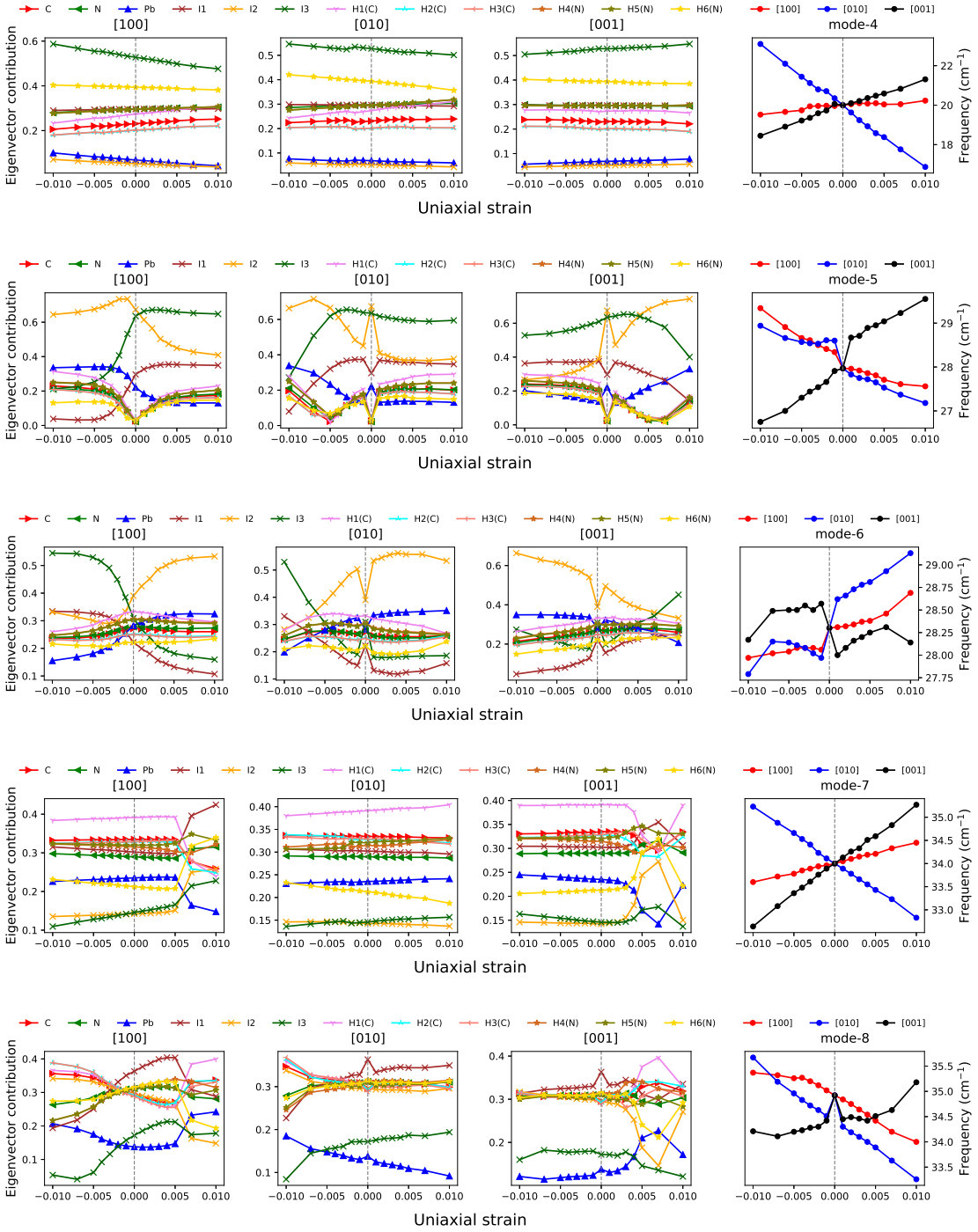

Figure 2.27: Mode eigenvector vs. strain, and frequency vs. strain, for each of the three crystallographic directions.

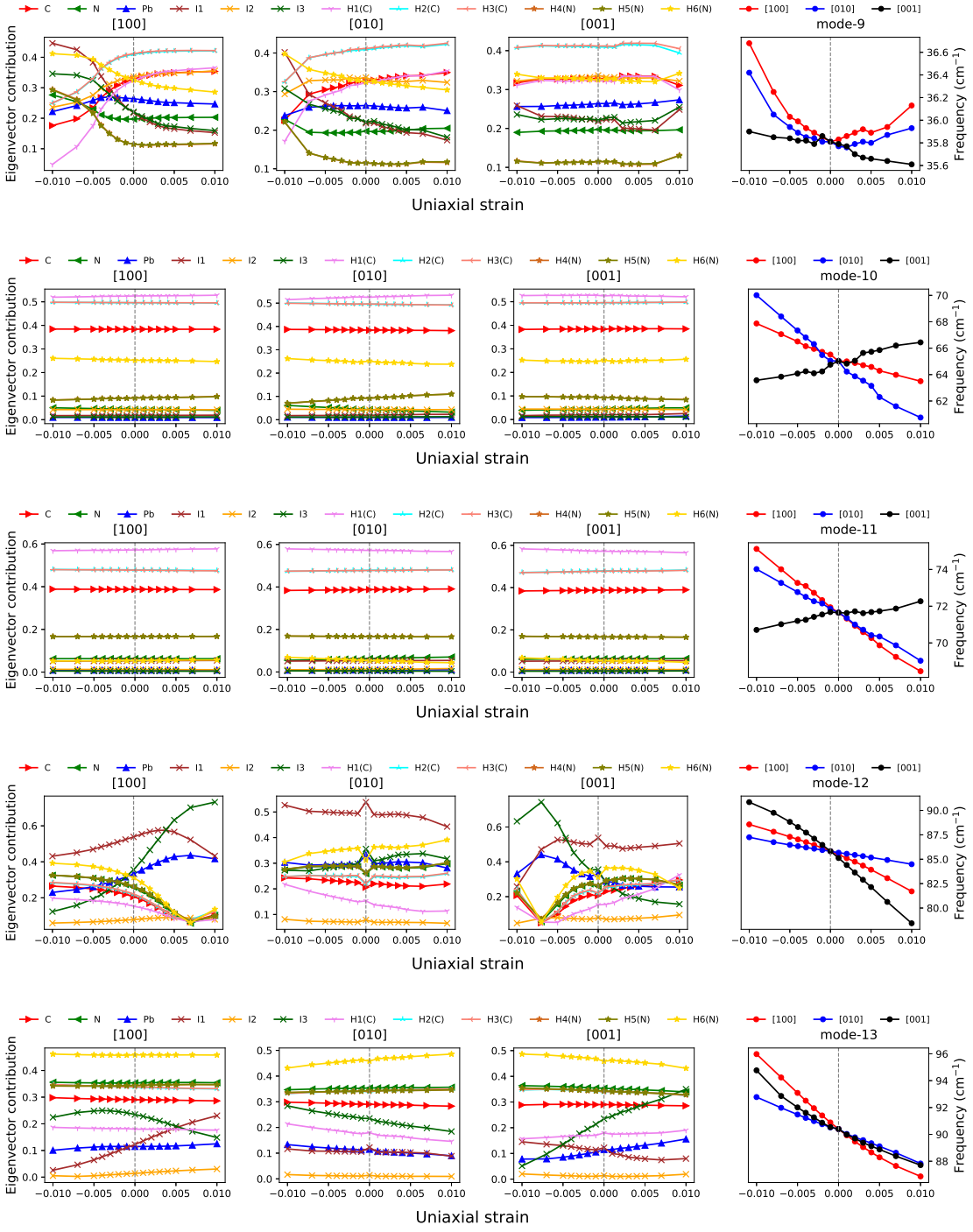

Figure 2.28: Mode eigenvector vs. strain, and frequency vs. strain, for each of the three crystallographic directions.

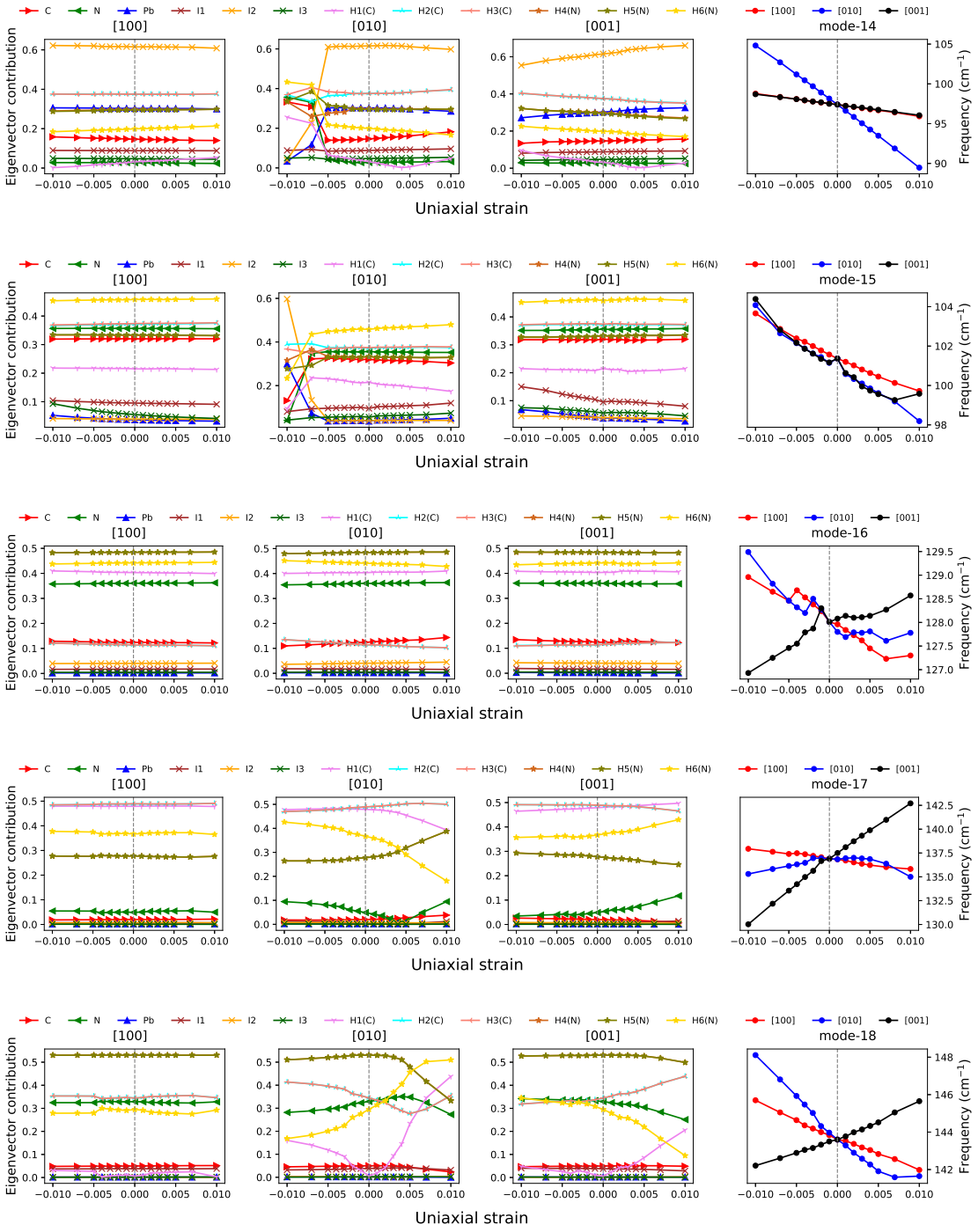

Figure 2.29: Mode eigenvector vs. strain, and frequency vs. strain, for each of the three crystallographic directions.

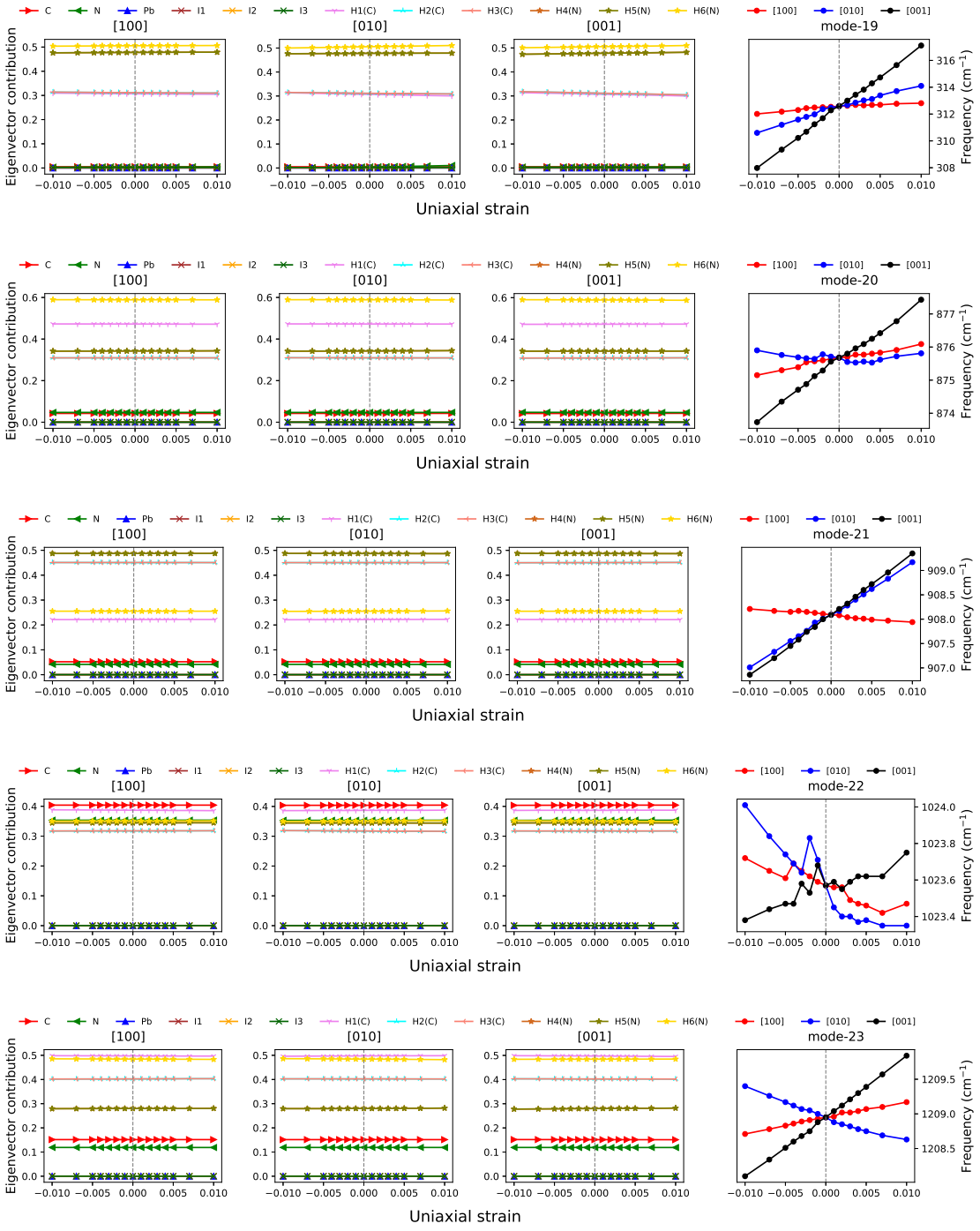

Figure 2.30: Mode eigenvector vs. strain, and frequency vs. strain, for each of the three crystallographic directions.

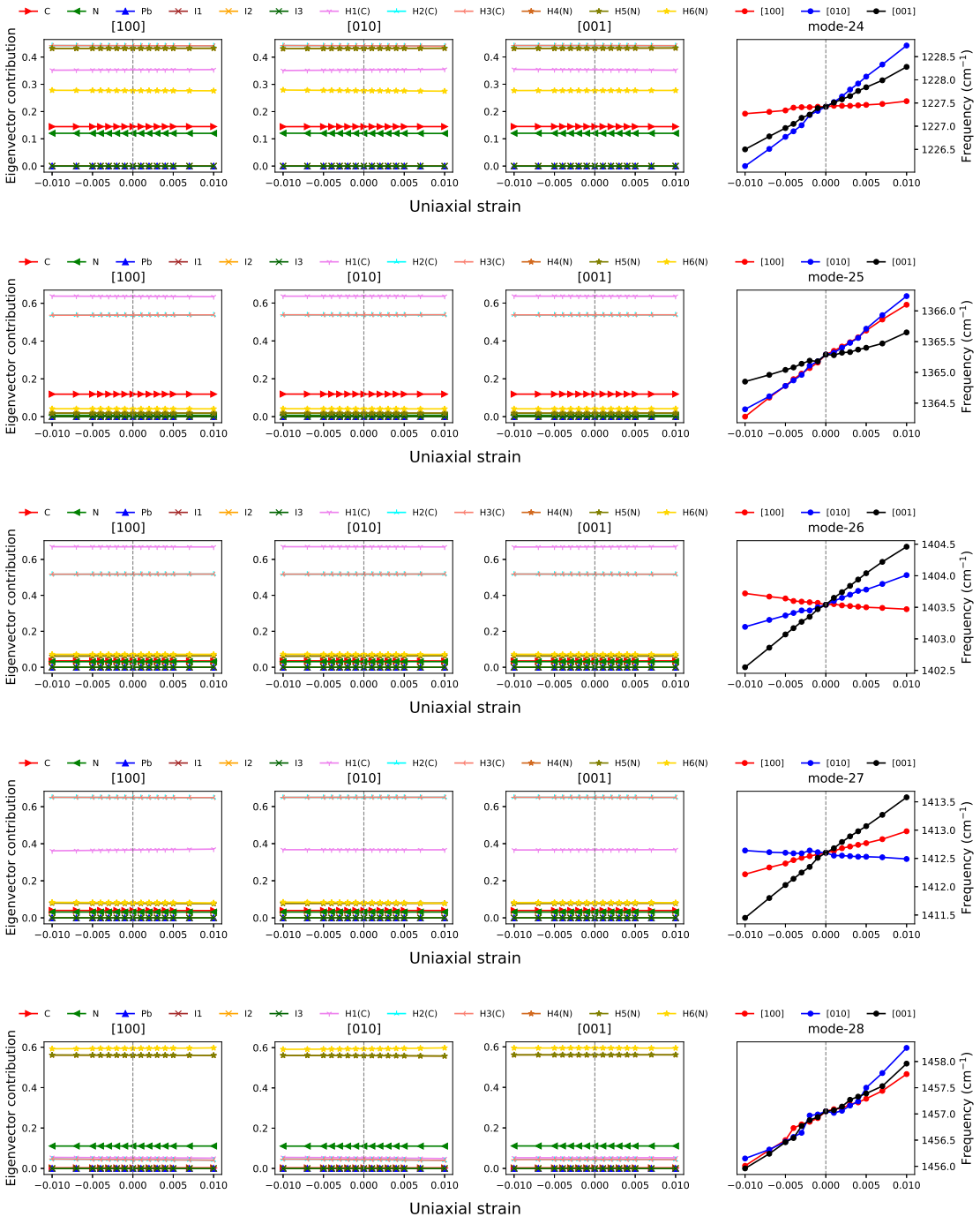

Figure 2.31: Mode eigenvector vs. strain, and frequency vs. strain, for each of the three crystallographic directions.

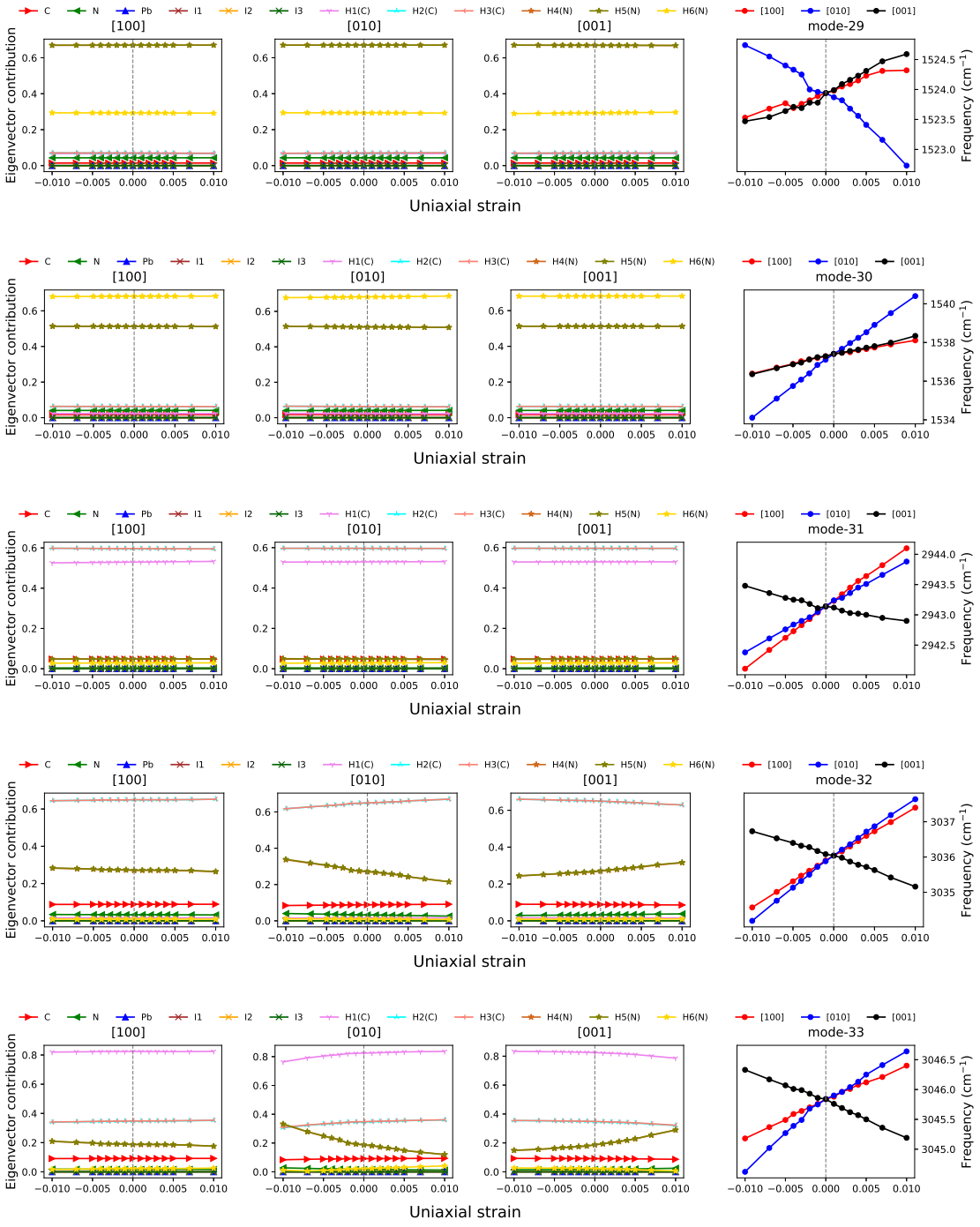

Figure 2.32: Mode eigenvector vs. strain, and frequency vs. strain, for each of the three crystallographic directions.

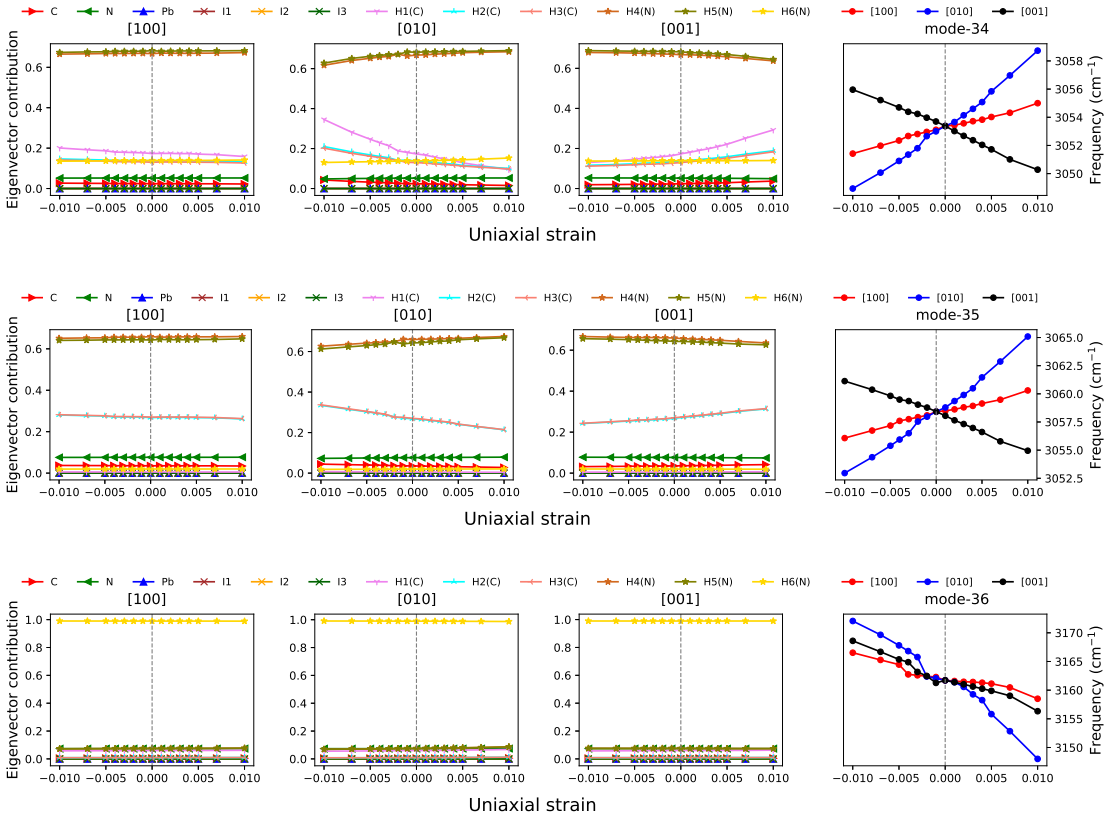

Figure 2.33: Mode eigenvector vs. strain, and frequency vs. strain, for each of the three crystallographic directions.

Chapter 3

Interplay of structural changes, symmetry and vibrations in orthorhombic and tetragonal hybrid perovskites under stress

3.1 Abstract

Despite perovskite solar cells' rapid rise in photoconversion efficiency, their commercialization is facing issues due to stability problems. Factors such as moisture, heat and illumination, cause degradation which can be mitigated by encapsulation techniques. Another important factor is local stress which may develop in organic metal-halide perovskites, affecting optoelectronic properties and playing a major role in their performance and stability. Previously we have studied the high-temperature pseudo-cubic phase of $CH_3NH_3PbI_3$. In this work, we studied the low-temperature orthorhombic and room-temperature tetragonal phases, analyzing vibrations under uniaxial strain with density functional perturbation theory. We have classified modes which show linear, quadratic and non-linear shifts with strain and also found the best modes for inferring strain using IR and Raman spectroscopy. Considering exact and approximate symmetries, we have analyzed changes in the structural parameters, phonon displacement patterns, and dynamical matrices, to understand changes in frequency from a perturbative approach. We found I-N interactions play a significant role in the change of vibrational modes under

strain. Our study gives insight into the interaction between strain, structural changes and vibrational modes to help understand photovoltaic performance and degradation.

3.2 Introduction

In the last decade, the photo conversion efficiency of hybrid organic-inorganic perovskites has skyrocketed (from 3.8%[70] to 25.2%.[97]). This improvement in PCE makes them a promising material for next generation solar cell application.[49] Apart from that they also have some of the good qualities that are required for a solar cell[36, 145, 126, 133, 156, 150]. The main drawback that is hindering its large scale commercial application is their instability[96, 21, 62] which also improved a lot over the years.[73, 78] One of the reasons of its instability is light itself[62] and another reason is strain.[99, 94, 163, 29, 161, 10, 143, 61, 164, 127] The strain may develop in the material by many ways such as epitaxial lattice mismatch[19], thermal expansion mismatch with the substrate, phase transitions, grain boundaries, compositional inhomogenities, light soaking etc.[29, 161, 61, 143] We need to understand the interplay between structural changes, symmetry and vibrations under strain to understand the root cause behind degradation of these materials.

In previous work we have studied in detail the high-temperature pseudo-cubic phase[138]. In this work we study the room temperature tetragonal phase and the low temperature orthorhombic phase.[27] There is similarity in phonon density of states between these three structures (Figure 3.1). In the low frequency range we can see the coupled vibrations of the PbI_6 octahedra and $CH_3NH_3^+$ ions whereas in the mid and high frequency range the vibrations are mainly due to the MA^+ ion. This similarity in the mid and high frequency regions in the phonon density of states suggests that the behaviour of the ortho and tetra MAPI phonon modes under strain will be similar to that of the cubic one as the main contribution to the pnonon modes in these two regions are from the MA^+ ions. As there are 4 MA^+ ions in orthorhombic and tetragonal MAPIs whereas one MA^+ ion in cubic, In the mid and high frequency regions we expect the phonon modes to come in a set of 4 for each phonon mode of the cubic one. Strain in the material can cause a shift in the phonon mode frequencies and these shifts can be helpful to measure localized strain in MAPI perovskites using Raman and IR spectroscopy.[138] To calibrate these frequency shifts with respect to strain we need to plot frequency Vs strain graphs. We have calculated the Raman and IR spectra for both orthorhombic

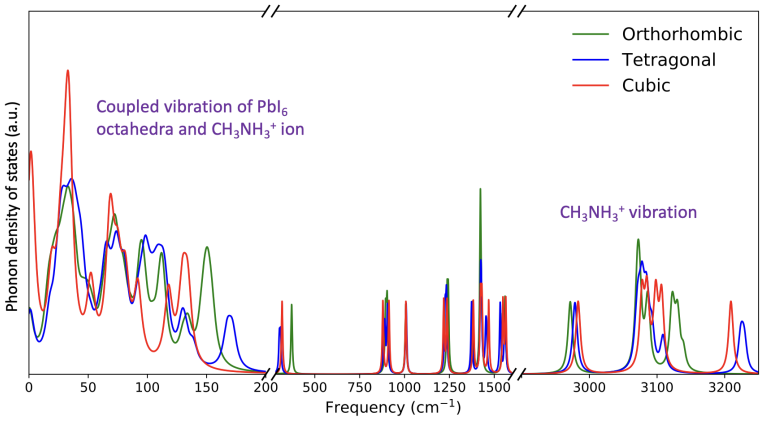

Figure 3.1: Comparison of phonon density of states for cubic, tetragonal and orthorhombic MAPIs. Phonon density of states is multiplied by 4 for cubic structure to compare with the equivalent orthorhombic and tetragonal MAPIs.

and tetragonal phases and profile all the phonon mode shifts under uniaxial strain. We have analyzed the strain induced structural changes and also analyzed the dynamical matrix to understand which inter-atomic interactions are playing major roles in the phonon mode shifts under uniaxial strain. We have calculated and compared the mode Grüneisen parameter for these two modes and compared the result with cubic phase. Finally, we provide the best Raman and IR modes that will be helpful to measure local stress in orthorhombic and tetragonal MAPIs using Raman and IR spectroscopy.

3.3 Methods

3.3.1 Computational details

Density functional perturbation theory (DFPT)[9] as implemented in Quantum ESPRESSO (version 6.4.1)[43, 44, 8] is used for phonon mode calculations. The Local Density Approximation[101] (LDA) with the Perdew-Wang (PW) parametrization[104] is used for the exchange-correlation potential for all the calculations. Scalar relativistic Optimized Norm-Conserving Vanderbilt (ONCV) pseudopotentials[53] are used which treat Pb 5*d* orbitals as valence. All the pseudopotentials are taken from Pseud$\bar{o}$ D$\bar{o}$j$\bar{o}$[146] (NC SR ONCVPSP v0.4) with standard accuracy. Spin-orbit coupling is not considered for the calculation as it does not have much effect on interatomic interactions near equilibrium.[15]. The Brillouin zone is sampled using a half-shifted 5×4×5 (for or-

thorhombic) and 5×5×4 (for tetragonal) Monkhorst-Pack grid with an energy cutoff of 100 Ry for the wave-functions. Atomic positions are optimized until the total force per atom is smaller than 1 meV/Å; for the initial variable-cell relaxation, a 0.5 kbar stress convergence threshold is used. We compared different functionals (PBE, PBEsol and LDA) and also checked the effect of Grimme-D2 van der Waals correction for structural optimization of both the structures. The equilibrium structure parameters are reported in table 3.1. PBEsol and PBE+vdW and LDA gives fairly good estimates compared to experimental lattice parameters. A few more things that we have noticed are 1) Pb-I bond length is over estimated in PBE whereas it is underestimated in LDA. PBEsol and PBE+vdW gives fair results compared to experiment. The overall Pb-I bond length is higher in orthorhombic and tetragonal then cubic structure. 2) PBE and PBEsol behaves similarly while estimating Pb-I-Pb bond angle. It can seen that the average bond angle is lowest for orthorhombic structure and highest for cubic structure which gives an indication that as the temperature decreases the Pb-I-Pb buckling increases especially in the *ab* plane. 3) For C-H and N-H bond lengths, LDA> PBEsol> PBE> PBE+vdW. 4) C-N bond length reduced in the following order, tetragonal < orthorhombic < cubic. Though PBE with van der Waals correction works best for structural and elastic parameter calculations, LDA without van der Waals correction can still be good to calculate phonon modes, IR and Raman intensities[105] and quantum ESPRESSO can only calculate Raman intensity for LDA.

3.4 Results and Discussion

3.4.1 Structure Details

Depending on temperature, MAPI exists in three different phases: orthorhombic at low temperature ($T < 161.4K$), tetragonal at room temperature ($161.4K < T < 330.4K$), and cubic (or pseudo-cubic) at high temperature ($T > 330.4K$). Both orthorhombic and tetragonal MAPI structures are $\sqrt{2} \times \sqrt{2} \times 2$ supercell expansion of the cubic lattice (Figure 3.2).

Orthorhombic MAPI is reported to have D_{2h} point group symmetry[15] whereas the experimental structure of the tetragonal MAPI is reported to have D_{4h} point group[4, 151]. There are previous studies that report most stable structures of orthorhombic and tetragonal MAPIs based on molecular dynamics and DFT calculations[112, 15]. In the

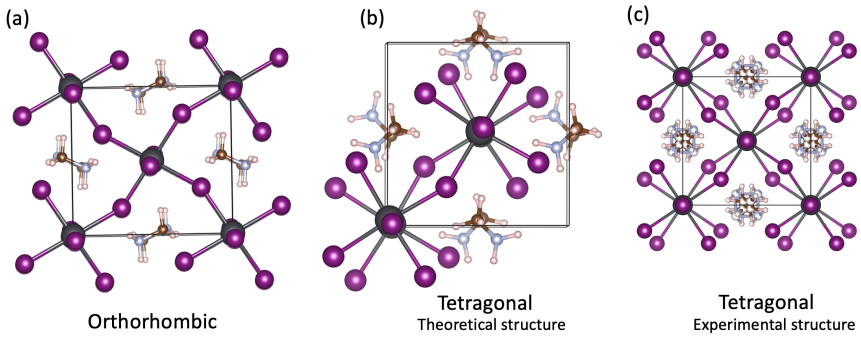

Figure 3.2: Crystal structure of (a) orthorhombic, (b) tetragonal (used in theory), and (c) tetragonal (experimental[4]) MAPIs. All the structures are shown along their largest crystallographic directions.

low temperature phase the alignment of all four MA^+ ions are properly ordered and static. This helps to make the structure exactly symmetric. For room temperature phase, the orientation of MA+ ions are no longer static, it rotates fast (ps) which makes the whole alignment disordered. Although the experiment measures the structure to be exactly symmetric due to the fractional occupation of MA+ ions but for our computational purpose, we have to use the MA+ ion orientation in a particular snapshot of the various possible orientations which brakes all the symmetry of the structure. Quarti et al. have come up with some possible structures of tetragonal MAPIs which are stable.[112] The initial structures for this work are taken from the work of Brivio et al.,[15]. The tetragonal structure is also reported as one of the most stable structures in Quarti et al.[112] Our calculated structural lattice parameters are shown in table (3.1). Our calculated phonon modes are compared with the experimental and theoretical results as shown in figure 3.3.

3.4.2 Crossing mode problem and solution

When the mode frequencies are degenerate or close it becomes harder to understand or predict which mode at one strain corresponds to another mode at another strain. Some modes that looks like they should cross other modes at some point are seemed to bend in a way that that prohibits the crossing. This problem is what we called "crossing mode problem". If we overlook this problem, we might end up getting wrong results. The problem of some crossing modes for orthorhombic MAPI are shown in figure (3.5a). We have looked into this problem with great detail and tried to solve

Table 3.1: Comparison of lattice parameters for tetragonal and orthorhombic structures.

Tetragonal MAPI								
Method	**Lattice parameters in (Å)**			**Bond lengths in (Å)**				**Bond angle in degree**
	a	**b**	**c**	**Pb-I**	**C-H**	**N-H**	**C-N**	**Pb-I-Pb**
LDA	8.520	8.520	12.624	3.145	1.0997	1.0487	1.4679	178.064
				3.104				178.060
				3.143	1.1007	1.0428		153.805
				3.112	1.1009	1.0480	1.4678	144.102
				3.183				152.285
				3.134				146.777
PBE	8.937	8.938	13.188	3.247	1.0930	1.0319	1.4927	150.775
				3.367		1.0391		157.878
				3.245		1.0396		155.737
				3.236	1.0924	1.0398	1.4926	152.984
				3.185	1.0929	1.0393		172.844
				3.304		1.0321		172.854
				3.232				
PBESol	8.709	8.710	12.844	3.176	1.0981	1.0455	1.4808	150.502
				3.169	1.0986	1.0450		154.402
				3.215	1.0985	1.0385		156.137
				3.131	1.0980	1.0446	1.4809	148.199
				3.198	1.0987	1.0449		173.136
				3.236		1.0385		173.119
PBE+vdW	8.674	8.674	12.886	3.132	1.0927	1.0367		152.686
				3.251	1.0942	1.0376		153.818
				3.201	1.0939	1.0333	1.4911	145.133
				3.183	1.0929	1.0380	1.4911	141.863
				3.205	1.0937	1.0392		178.662
				3.243	1.0939	1.0330		178.635
Expt.[6]	8.855	8.855	12.446					
Expt.[151]	8.806	8.806	12.713	3.172				157.920
				3.174				180.000
				3.178				
PBE+vdW-DF[42]	8.940	8.940	12.980					
PBE+vdW-DF[42]	9.060	8.770	12.910					
PBEsol[15]	8.700	8.720	12.830					
Orthorhombic MAPI								
LDA	8.191	12.464	8.841	3.137	1.1004	1.0478	1.469	147.861
				3.133	1.1011	1.0456		167.956
				3.134		1.0456		
PBE	8.572	12.933	9.331	3.255				
				3.265	1.0927	1.0377	1.494	152.586
				3.256	1.0930	1.0371		166.820
				3.265				
PBESol	8.363	12.652	9.073	3.181	1.0986	1.0430	1.482	151.255
				3.188	1.0989	1.0438		167.803
				3.181				
PBE+vdW	8.404	12.757	8.843	3.195	1.0932	1.0334	1.492	145.135
				3.199	1.0937	1.0390		167.434
				3.209				
Expt.[109]	8.861	12.659	8.581					
Expt.[6]	8.836	12.580	8.555					
Expt.[151]	8.866	12.629	8.577	3.197				150.750
				3.187				161.940
				3.187				
PBE+vdW-DF[42]	9.070	12.800	8.770					
DFT/PBEsol[15]	9.040	12.660	8.350					
PZ81/LDA[149]	8.678	12.387	8.318					
optB86b+vdW-DF[149]	8.831	12.648	8.570					

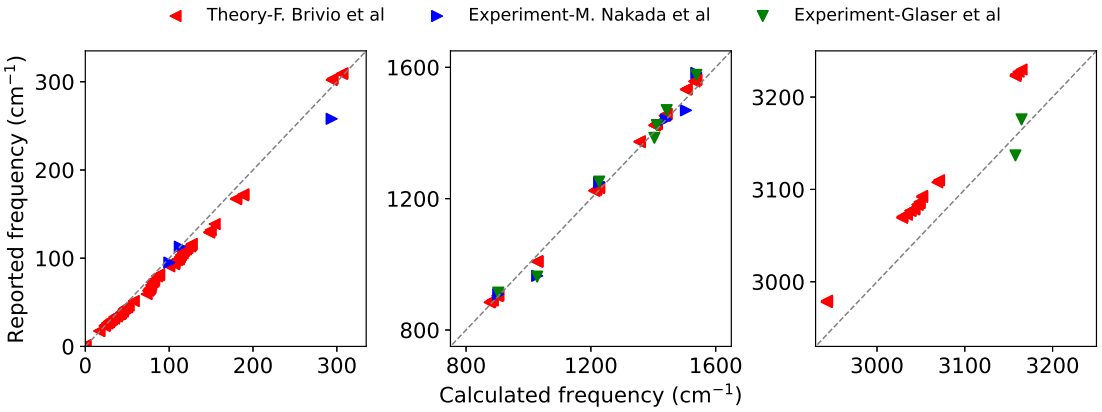

Figure 3.3: Comparison of calculated phonon mode frequencies with experimental Raman[92], IR[48] and theoretical[15] results for tetragonal MAPI.

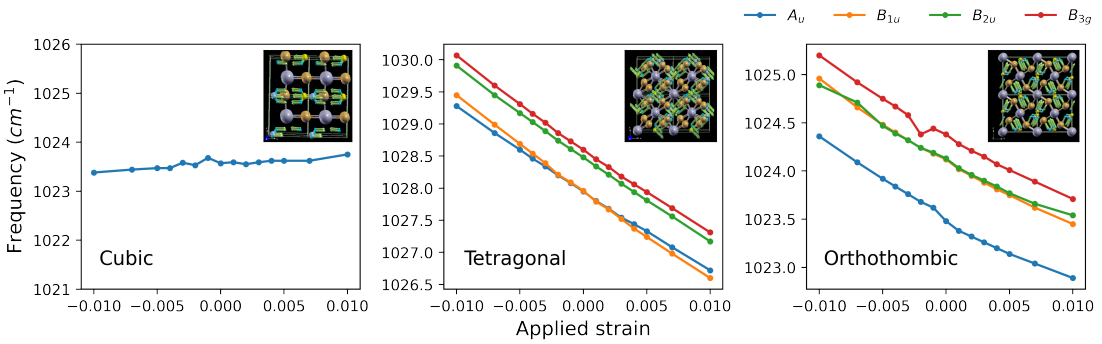

Figure 3.4: Comparison of similar phonon modes for three phases of MAPIs. For tetragonal and orthorhombic they are in a set of 4 for each mode in the cubic for mid and high frequency regions. Symmetric C-N stretch can be seen for A_g and B_{3g} whereas asymmetric C-N stretch for B_{1u} and B_{2u}.

it. As we can see in figure (3.5a) that IR and Raman intensities have suddenly changed by a large amount for some of the modes which indicates that some mode which was IR/Raman active suddenly become IR/Raman inactive and vice versa. This is not the actual situation that happen for these modes when we apply strain and these are the modes that have the crossing mode problem. Because the symmetry of the structure does not change with the range of strains that we used, all the mode symmetries also does not change and hence this sudden activity/inactivity of IR or Raman modes should not happen. This means we should not make certain assumptions without proper understanding of the quantum ESPRESSO ph.x and dynmat.x output.

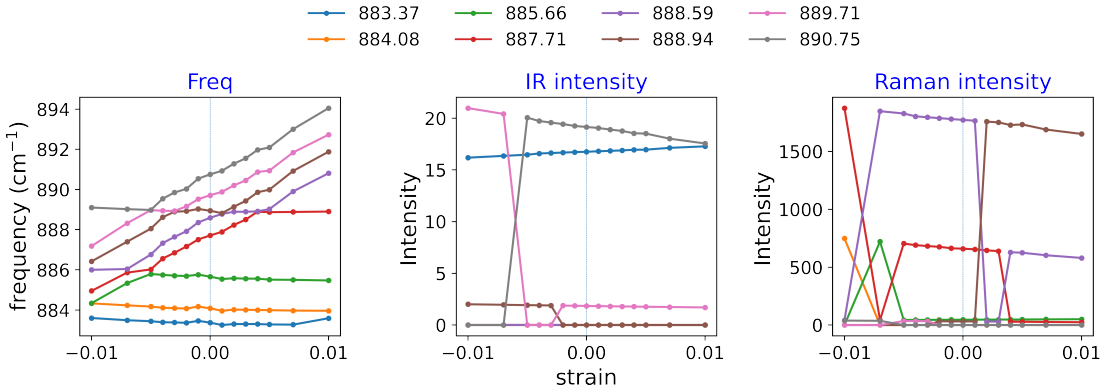

(a) Crossing mode problem assuming modes do not reorder in frequency with strain.

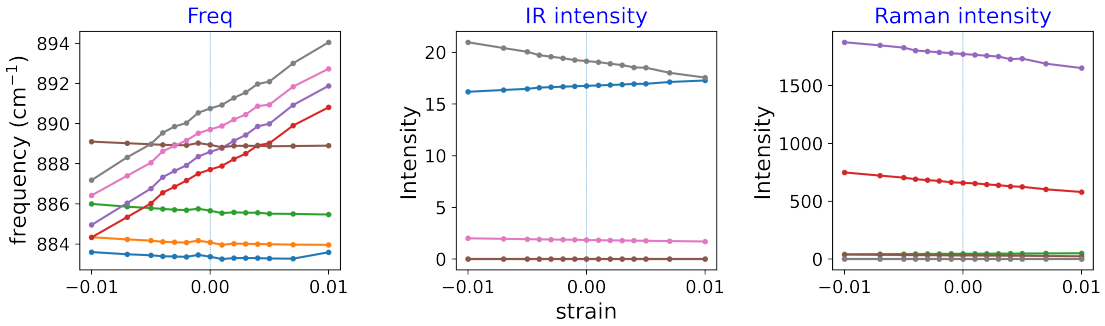

(b) actual crossing modes after using irreducible representations from updated code to connect modes.

Figure 3.5: Crossing mode problem and solution for orthorhombic MAPI structure.

The reason we end up with these crossing mode problem is the wrong understanding of the dynmat.x output. Quantum Espresso uses ph.x to calculate phonon mode frequencies and mode irreducible representations by calculating the dynamical matrix $D_{I\alpha,J\beta}$ and diagonalizing it. In its dynmatrix.f90 code it applies the acoustic sum rule (ASR[12]) to the calculated dynamical matrix and does not recalculate the mode irreducible representations. This process change some of the mode frequencies a little bit and the sorted output makes it difficult to identify which mode shifted up or down as we can see in figure (3.6) for mode 14 and 15. The incorrect assumption is that the mode frequency will be in the same order in the ph.x and dynmat.x output which is not. For a single phonon calculation this does not matter much as all we need are the mode frequencies and the mode eigenvectors but for a special case where the minute change in frequency, and the order matters to identify which mode shifted up or down such as in our case, it is important identify the modes. If we directly use the result form the dynmat.x output for all the modes to check the change in frequency with respect to strain we end up something like figure (3.5a).

(a) ph.x output: after diagonalizing the dynamical matrix

```
     Mode symmetry, D_2h (mmm)  point group:

     freq (  1 -  1) =        -4.8  [cm-1]   --> B_3u            I
     freq (  2 -  2) =        -3.6  [cm-1]   --> B_1u            I
     freq (  3 -  3) =         4.6  [cm-1]   --> B_2u            I
     freq (  4 -  4) =        17.0  [cm-1]   --> A_u
     freq (  5 -  5) =        19.1  [cm-1]   --> A_g             R
     freq (  6 -  6) =        19.5  [cm-1]   --> B_3u            I
     freq (  7 -  7) =        21.6  [cm-1]   --> B_2u            I
     freq (  8 -  8) =        23.8  [cm-1]   --> B_1u            I
     freq (  9 -  9) =        24.1  [cm-1]   --> A_u
     freq ( 10 - 10) =        24.7  [cm-1]   --> B_3u            I
     freq ( 11 - 11) =        26.0  [cm-1]   --> B_1g            R
     freq ( 12 - 12) =        27.2  [cm-1]   --> B_3g            R
     freq ( 13 - 13) =        30.1  [cm-1]   --> A_u
     freq ( 14 - 14) =        31.6  [cm-1]   --> B_1u            I
     freq ( 15 - 15) =        31.8  [cm-1]   --> A_g             R
     freq ( 16 - 16) =        31.9  [cm-1]   --> B_3u            I
     freq ( 17 - 17) =        32.3  [cm-1]   --> B_2u            I
     freq ( 18 - 18) =        34.2  [cm-1]   --> B_2g            R
```

(b) dynmat.x output: after applying acoustic sum rule (ASR)

```
 # mode    [cm-1]    [THz]      IR          Raman    c
     1     -0.00   -0.0000    0.0000         0.0000
     2      0.00    0.0000    0.0000         0.0000
     3      0.00    0.0000    0.0000         0.0000
     4     16.99    0.5094    0.0000         0.0000
     5     19.11    0.5729    0.0000        18.9492
     6     19.64    0.5889    0.0171         0.0000
     7     21.63    0.6485    0.3919         0.0000
     8     23.79    0.7131    0.0790         0.0000
     9     24.12    0.7230    0.0000         0.0000
    10     24.94    0.7478    0.2437         0.0000
    11     26.03    0.7805    0.0000         0.0532
    12     27.23    0.8164    0.0000         9.9779
    13     30.08    0.9018    0.0000         0.0000
    14     31.76    0.9523    0.0000       207.9332
    15     31.87    0.9555    2.2115         0.0000
    16     31.95    0.9578    0.9336         0.0000
    17     32.61    0.9775    0.0557         0.0000
    18     34.19    1.0249    0.0000         0.9694
```

Figure 3.6: Quantum ESPRESSO 6.4.1 code output (first 18 phonon modes) using (a) ph.x and (b) dynmat.x. for orthorhombic MAPI.

This is a problem that can occur not only for perovskites but for any material which has degenerate or close to degenerate modes. There are two ways we can solve this problem. One is, we recalculate the mode characters after the application of ASR in the dynmat.x code and print it on the output for each mode as it is printed in the ph.x output which needs dynmat.f90 code modification. The other solution is to look at the IR and Raman intensity patterns for the entire range of strain and identify the crossing modes

mode	[cm-1]	[THz]	IR	Raman	depol.fact	mode_chr	
1	-0.00	-0.0000	0.0000	0.0000	0.0000	?	
2	0.00	0.0000	0.0000	0.0000	0.0000	?	
3	0.00	0.0000	0.0000	0.0000	0.0000	?	
4	16.99	0.5094	0.0000	0.0000	0.3111	A_u	
5	19.11	0.5729	0.0000	18.9492	0.3924	A_g	R
6	19.64	0.5889	0.0171	0.0000	0.3466	B_3u	I
7	21.63	0.6485	0.3919	0.0000	0.0671	B_2u	I
8	23.79	0.7131	0.0790	0.0000	0.6313	B_1u	I
9	24.12	0.7230	0.0000	0.0000	0.7476	A_u	
10	24.94	0.7478	0.2437	0.0000	0.7031	B_3u	I
11	26.03	0.7805	0.0000	0.0532	0.7500	B_1g	R
12	27.23	0.8164	0.0000	9.9779	0.7500	B_3g	R
13	30.08	0.9018	0.0000	0.0000	0.7288	A_u	
14	31.76	0.9523	0.0000	207.9332	0.6388	A_g	R
15	31.87	0.9555	2.2115	0.0000	0.6909	B_1u	I
16	31.95	0.9578	0.9336	0.0000	0.6406	B_3u	I
17	32.61	0.9775	0.0557	0.0000	0.6353	B_2u	I

Figure 3.7: Quantum ESPRESSO 6.4.1 code output of dynmat.x after implementation of our code modification. Last two columns are the results of our modified code.

manually and update accordingly. The first method will be helpful for all the materials that has a perfect symmetry but for those materials that does not have exact symmetry we have to follow the second solution. We have modified the dynmat.f90 code and implemented our code to solve the crossing mode problem for orthorhombic MAPI. The output of the dynmat.x code after our modification in shown in figure (3.7). We can see that the mode irreducible representations are calculated and printed for each mode which solves the problem discussed above. We can see a "?" for the irreducible representations for the first three modes which is because they are the acoustic modes where each mode eigenvector can be represented by the linear combinations of eigenvectors of the other two modes, so there is no single irreducible representation. We have used the modified version of the code for some other materials and waiting to merge with the main code after some more tests. As the theoretical tetragonal MAPI structure does not have any exact symmetry we have used the other method to do the crossing mode adjustment.

3.4.3 Dynamical matrix analysis

Dynamical matrix for tetragonal and orthorhombic structure are given in figure 3.8. To make it comparable to the cubic one, we have arranged all the atoms for each methylammonium ion together. Now, they look like replica of four times of the cubic one which can be understood from the fact that the unit cell of both the structures are 4 times of the unit cell of cubic structure. Four deep squares in tetragonal and orthorhombic structure represents the 4 $CH_3NH_3^+$ ions. Two MA^+ ions that lies in a plane perpendicular to the largest lattice vectors are put next to each other. It can be

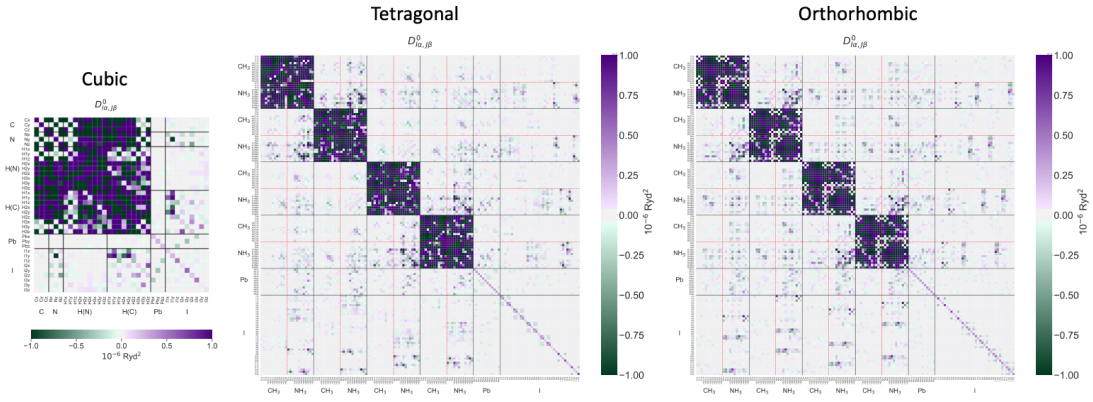

Figure 3.8: Comparison of dynamical matrices between cubic, tetragonal and orthorhombic MAPIs.

seen that the interaction between two $CH_3NH_3^+$ ions in the plane (perpendicular to the largest lattice vector) is more through the NH_3 part of the ion. There is less interaction between two MA^+ ions in different planes (parallel to the largest lattice vector). The interaction between the Pb-I cage and the ion is more through the NH_3 part of the ion. Hydrogens attached to carbon in the MA^+ ion are interacting more with the I than hydrogens that are attached to the nitrogen of the MA^+ ion. I-N interaction is stronger than I-C interaction. The changes in dynamical matrices due to compressive and tensile strains are given in the supplementary information (Fig.3.14, 3.15).

3.4.4 Different patterns of phonon mode shifts under uniaxial strain

The MAPI unit cells for orthorhombic and tetragonal structures are 4 times the cubic structure and both of them has 48 atoms per unit cell which makes 144 phonon modes for each of the structure. The first three of these 144 modes are the acoustic phonon modes. We have calculated all the phonon mode frequencies at Γ point (i.e. $q = 0$) only. We have classified the frequency shift patterns mainly into three categories: linear, parabolic, and non-linear. The perturbation of the dynamical matrix and mode eigenvectors due to strain is responsible for such parabolic and non linear patterns patterns in the frequency shifts.[138] The mode mixing for the parabolic patterns can be seen in figure (3.9). It can be seen that the mode mixing is more for the parabolic modes. To identify the modes with linear, parabolic, and non linear frequency shift patterns we have used linear and parabolic fitting. There are 144 modes in three different directions

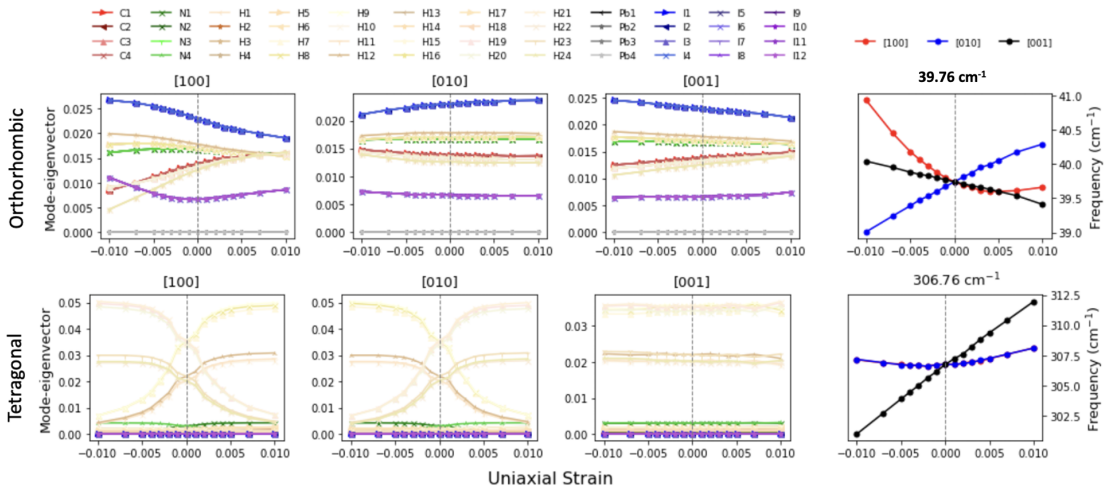

Figure 3.9: Mode mixing for orthorhombic structure can be seen for strain along [100] direction and for tetragonal structure for both [100] and [010] directions.

for two different structures that makes the total of 1728 curve fitting. For the purpose of this work we have calculated the frequency shifts for strain range -0.01 to 0.01 but for the pattern and the slope calculation we considered the strain range from -0.004 to 0.004 so that we can compare the same with the cubic structure. It is not feasible to look at such high number of the fitting manually and check. So, we have calculated relative squared error (RSE) for each fitting and from this we calculated R^2=(1-RSE) as the goodness of fit. Those modes for which the R^2 value for linear fit is greater than 0.99, we considered them as linear and if R^2 >0.99 for parabolic fit and the improvement over the linear fit is greater than 0.005, we marked them as parabolic. In figure 3.10 and figure 3.11 we have shown how we calculated R^2 for orthorhombic and tetragonal MAPIs. It can also be seen that for tetragonal structure the frequency shift patterns are identical for [100] and [010] strains. This is due to the approximate structural symmetry. For each phase we have calculated the number of linear and parabolic modes and the percentages are given in table 3.2. We can see that the number of linear modes are high in the [001] direction for all three structures and the cubic structure has parabolic modes only for the [010] uniaxial strain.

To find out best possible modes for Raman and IR spectroscopy to measure local strain in orthorhombic and tetragonal MAPIs we need to find out modes that are linear with high average slopes and good Raman and IR intensity. For uniaxial strain along three crystallographic axes [100], [010] and [001] we have calculated the slopes

Table 3.2: Percentage of linear and parabolic modes for uniaxial strains along [100], [010], and [001] for cubic, tetragonal and orthorhombic MAPIs.

MAPI Phase	Percentage of linear modes			Percentage of parabolic modes		
	[100]	[010]	[001]	[100]	[010]	[001]
Cubic	41.67	30.56	38.89	0.00	5.56	0.00
Tetragonal	42.36	40.97	68.06	5.56	4.17	2.78
Orthorhombic	36.81	38.89	54.86	4.17	2.08	2.08

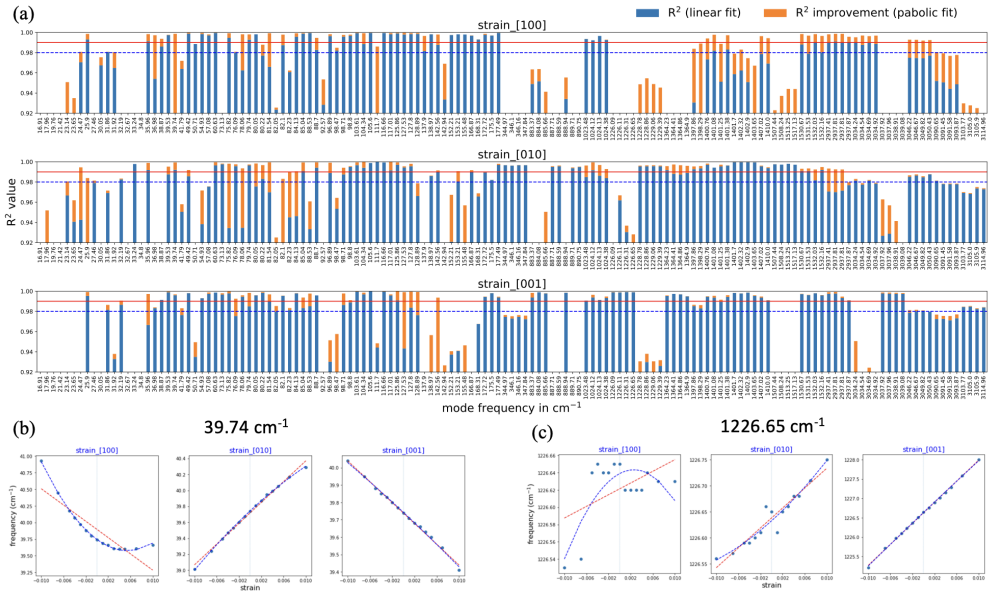

Figure 3.10: Classification of modes into linear, parabolic, and nonlinear based on the R^2 value for uniaxial strains along [100], [010], and [001] direction in orthorhombic MAPI.

for all the three phases and compare (Figure 3.12). We can see that for mid and high frequency regions all the modes of orthorhombic and tetragonal structure comes in a set of 4 (Figure 3.4), as mentioned earlier. To filter out best modes we have used the strain range form -0.004 to +0.004 and for linearity and good slope we choose those modes for which $R^2 > 0.98$ with absolute average slope value greater than 100. These modes are further filtered for good Raman and IR intensities. We select those modes which has Raman intensity greater than 30 Å^4/amu and IR intensity greater than 3 (D/Å)^2/amu. The best modes for all the three phases can be seen in figure 3.13. One good thing for all the best modes is that the slopes are either all positive or all negative which makes the average slope value better.

Table 3.3: Best modes for IR and Raman microscopy to probe local strain in tetragonal MAPI. Absolute IR intensity is in $(D/Å)^2$/amu and Raman intensity in $Å^4$/amu.

Freq. (cm^{-1})	**IR Int.**	**Raman Int.**	**Slope [100]** (cm^{-1})	**Slope [010]** (cm^{-1})	**Slope [001]** (cm^{-1})	**Avg. slope** (cm^{-1})	**Mode Characters**
Best Raman modes							
112.74	0.84	34.59	-255.67	-253.83	-228.33	-245.94	asym. CH_3-NH_3 vibration, libration
147.84	3.15	50.20	-314.17	-320.17	-152.83	-262.39	asym. CH_3-NH_3 vibration, libration
149.61	1.18	228.70	-345.33	-349.50	-193.50	-296.11	asym. CH_3-NH_3 vibration, libration
1027.95	0.71	113.83	-131.33	-130.00	-50.67	-104.00	C-N stretch, sym. CH_3-NH_3 vibration
1027.96	0.19	25.10	-142.33	-144.50	-56.67	-114.50	C-N stretch, sym. CH_3-NH_3 vibration
1028.48	0.63	57.78	-136.50	-135.83	-44.67	-105.67	C-N stretch, sym. CH_3-NH_3 vibration
1028.60	0.32	248.89	-137.83	-137.67	-51.00	-108.83	C-N stretch, sym. CH_3-NH_3 vibration
1531.04	4.14	199.22	90.33	90.83	138.83	106.67	asym. CH_3-NH_3 vibration, large NH_3 vibration
1537.95	0.32	49.03	87.17	87.00	143.50	105.89	asym. CH_3-NH_3 vibration, large NH_3 vibration
Best IR modes							
79.68	8.88	15.75	-244.17	-243.00	-352.17	-279.78	asym. CH_3-NH_3 vibration, libration
81.45	14.68	7.49	-246.00	-245.00	-120.67	-203.89	asym. CH_3-NH_3 vibration, libration
82.19	4.61	4.99	-155.67	-154.17	-457.33	-255.72	asym. CH_3-NH_3 vibration, libration
147.84	3.15	50.20	-314.17	-320.17	-152.83	-262.39	asym. CH_3-NH_3 vibration, libration
1531.04	4.14	199.22	90.33	90.83	138.83	106.67	asym. CH_3-NH_3 vibration, large NH_3 vibration

Table 3.4: Best modes for IR and Raman microscopy to probe local strain in orthorhombic MAPI. Absolute IR intensity is in $(D/Å)^2$/amu and Raman intensity in $Å^4$/amu.

Freq. (cm^{-1})	**IR Int.**	**Raman Int.**	**slope [100]** (cm^{-1})	**slope [010]** (cm^{-1})	**slope [001]** (cm^{-1})	**avg slope** (cm^{-1})	**Mode Characters**
Best Raman modes							
60.63	0.00	423.68	-186.00	-51.67	-139.17	-125.61	Pb-I bend, CH_3-NH_3 libration, translation
105.60	0.00	120.64	-207.33	-109.33	-205.17	-173.94	Pb-I stretch, asym. CH_3-NH_3 vibration, libration
153.21	0.00	20.05	-543.17	-221.83	-152.17	-305.72	CH_3-NH_3 spin, libration
1397.86	0.00	497.04	80.50	172.67	144.67	132.61	asym. CH_3 vibration
1410.00	0.00	2281.33	102.50	113.33	142.67	119.50	sym. NH_3, asym. CH_3 vibration
1531.53	0.00	172.07	90.67	72.50	191.00	118.06	asym. CH_3-NH_3 vibration
Best IR modes							
75.82	5.63	0.00	-256.83	-388.83	-273.67	-306.44	Pb-I-Pb bend, Pb-I stretch, asym. CH_3-NH_3 vibration, libration
79.74	11.29	0.00	-132.00	-342.50	-152.17	-208.89	Pb-I-Pb bend, Pb-I stretch, asym. CH_3-NH_3 libration, translation
80.05	16.32	0.00	-113.00	-633.67	-199.33	-315.33	Pb-I-Pb bend, Pb-I stretch, asym. CH_3-NH_3 vibration, libration
81.54	4.67	0.00	-104.50	-181.00	-144.33	-143.28	Pb-I-Pb bend, Pb-I stretch, asym. CH_3-NH_3 vibration, libration
85.04	6.21	0.00	-292.17	-166.00	-202.67	-220.28	Pb-I-Pb bend, Pb-I stretch, asym. CH_3-NH_3 vibration, libration
1398.29	7.33	0.00	79.50	180.83	144.00	134.78	asym. CH_3 vibration
1407.02	8.13	0.00	100.00	113.00	158.00	123.67	sym. NH_3, asym. CH_3 vibration

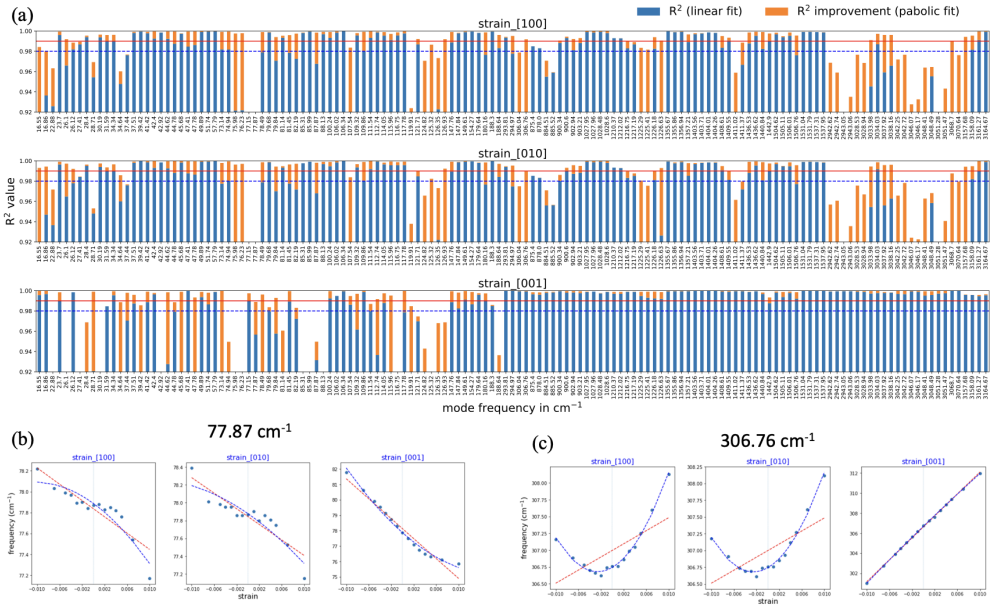

Figure 3.11: Classification of modes into linear, parabolic, and nonlinear based on the R^2 value for uniaxial strains along [100], [010], and [001] direction in tetragonal MAPI.

3.5 Conclusion

We have done a detail study of strain-induced structural changes (Supp info.) and phonon mode shifts under uniaxial strain for orthorhombic and tetragonal MAPI and compared the results with the cubic one. We found that for mid and high frequency phonon modes we get a set of 4 modes in case of ortho- and tetra- MAPIs for each mode in cubic structure. This is also supported by the similarity in their phonon density of states. The degenerate and close to degenerate modes of tetragonal and orthorhombic MAPIs shifts under uniaxial strain and and sometimes cross each other which is confusing from the standard output of Quantum ESPRESSO. For that reason we have modified the code and implemented our modification to resolve crossing mode problem. This modification will be helpful for any material. From dynamical matrix analysis we confirmed that I-N interaction plays major role for mode shifts under uniaxial strain. Analyzing linearity, slopes and intensities for IR and Raman for each mode, we reported the best possible modes for both of these structures that will be helpful to measure local strain in these material using IR and Raman spectroscopy.

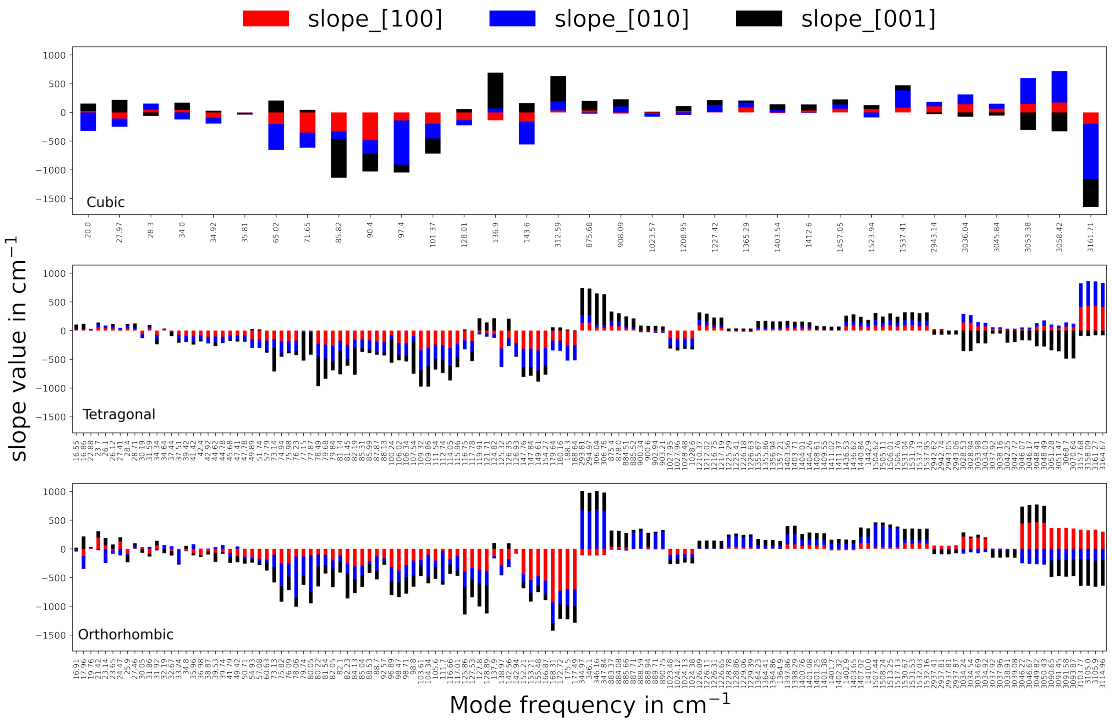

Figure 3.12: Calculated slopes for each mode for three different phases for uniaxial strains along [100], [010], and [001].

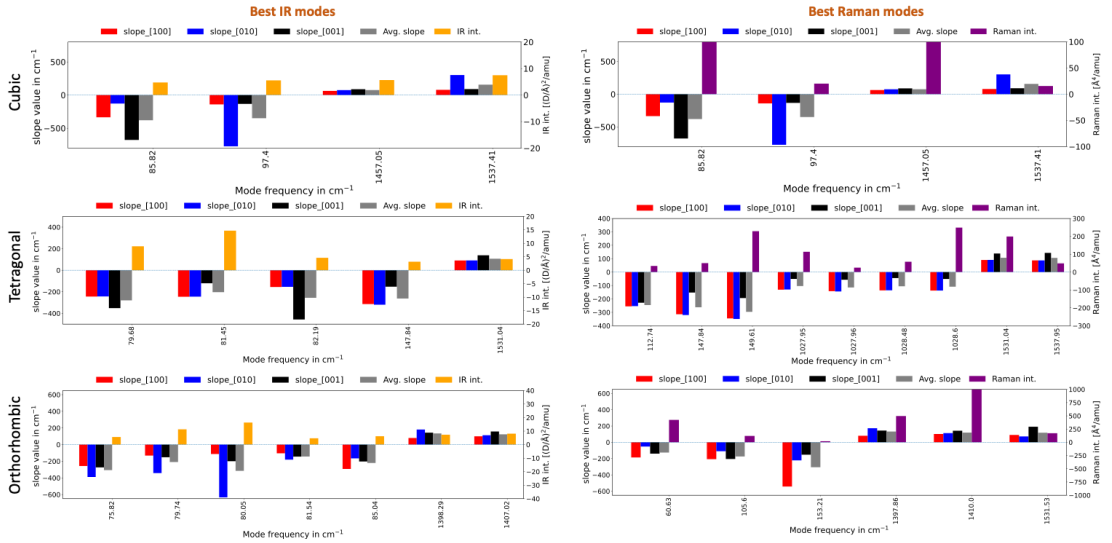

Figure 3.13: Best modes to probe local strain in cubic[138], tetragonal and orthorhombic MAPIs.

3.6 Acknowledgement

This material is based upon work supported by the Air Force Office of Scientific Research under award number FA9550-19-1-0236, and by UC Merced start-up funds. This work used computational resources from the Multi-Environment Computer for Exploration and Discovery (MERCED) cluster at UC Merced, funded by National Science Foundation Grant No. ACI-1429783, and the National Energy Research Scientific Computing Center (NERSC), a U.S. Department of Energy Office of Science User Facility operated under Contract No. DE-AC02-05CH11231.

3.7 Supplementary Information

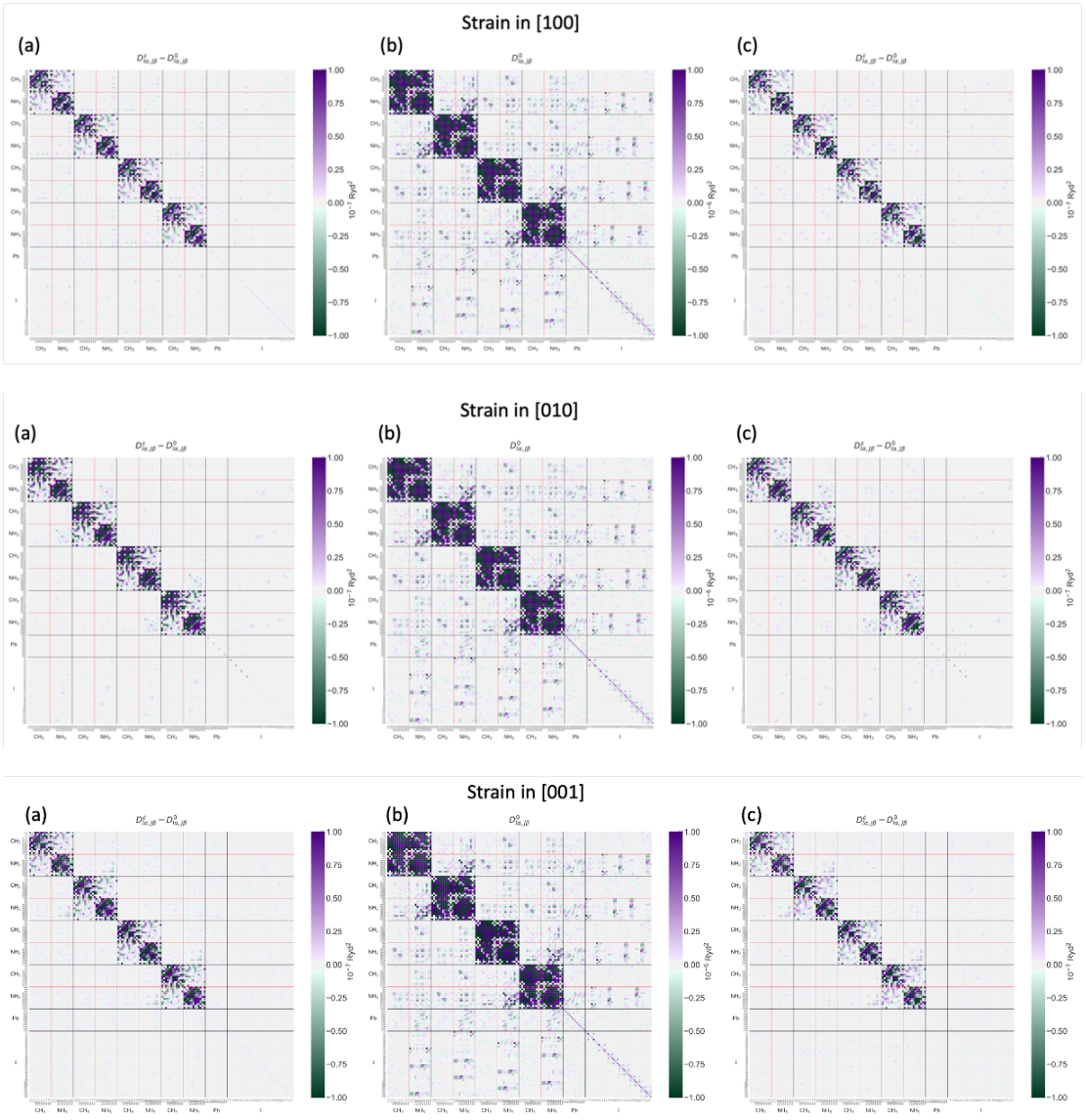

Figure 3.14: Dynamical matrix of orthorhombic MAPI for strain along [100], [010] and [001] directions. (a) Change for compressive strain ($\epsilon = -0.004$). (b) Dynamical matrix at zero strain. (c) Change for tensile strain ($\epsilon = 0.004$). Symbols in both the axes represent atoms and their coordinates. For example, within H(N) block, $H3_z$ denotes the z coordinate of the third H attached to N.

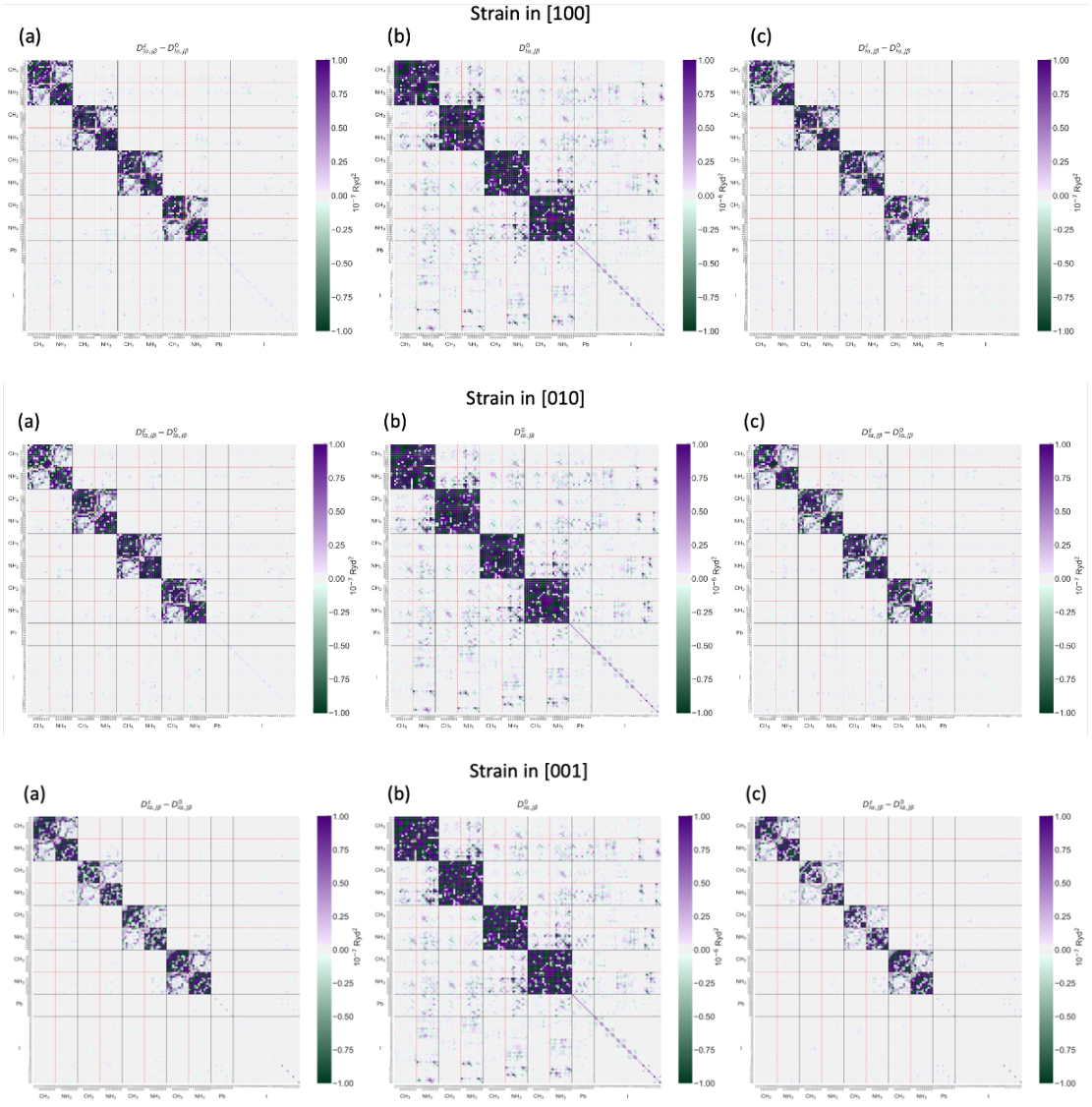

Figure 3.15: Dynamical matrix of tetragonal MAPI for strain along [100], [010] and [001] directions. (a) Change for compressive strain ($\epsilon = -0.004$). (b) Dynamical matrix at zero strain. (c) Change for tensile strain ($\epsilon = 0.004$). Symbols in both the axes represent atoms and their coordinates. For example, within H(N) block, $H3_z$ denotes the z coordinate of the third H attached to N.

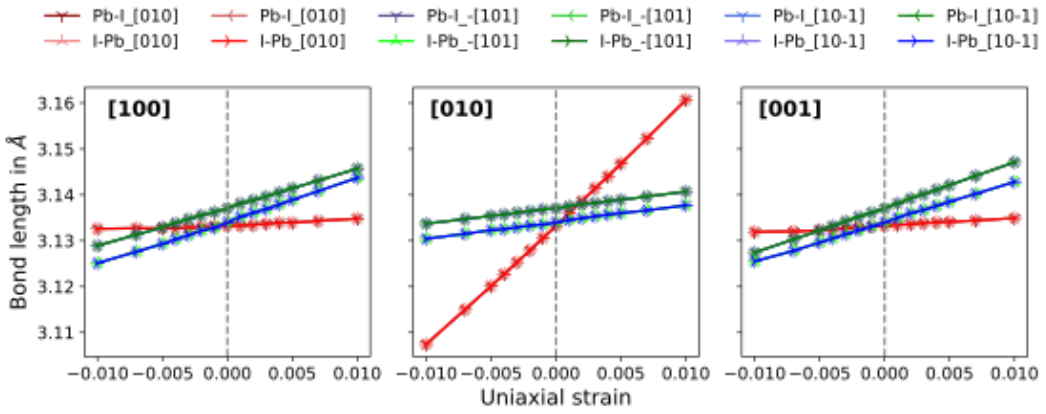

Figure 3.16: Change in Pb-I bond length in orthorhombic MAPI due to uniaxial compressive and tensile strain along [100], [010], and [001] directions.

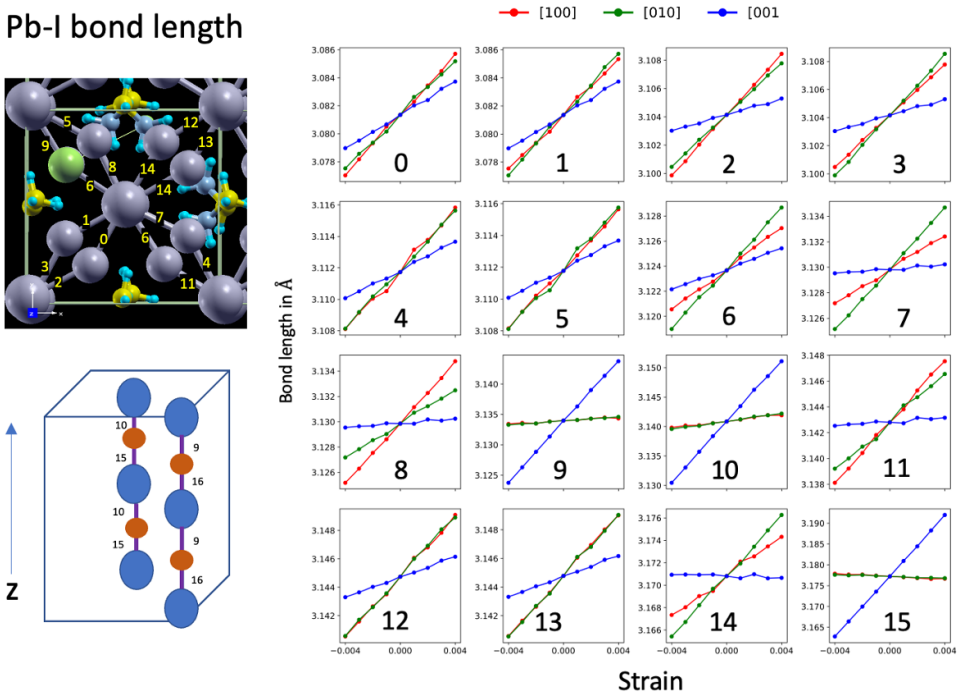

Figure 3.17: Change in Pb-I bond length in tetragonal MAPI due to uniaxial compressive and tensile strain along [100], [010], and [001] directions.

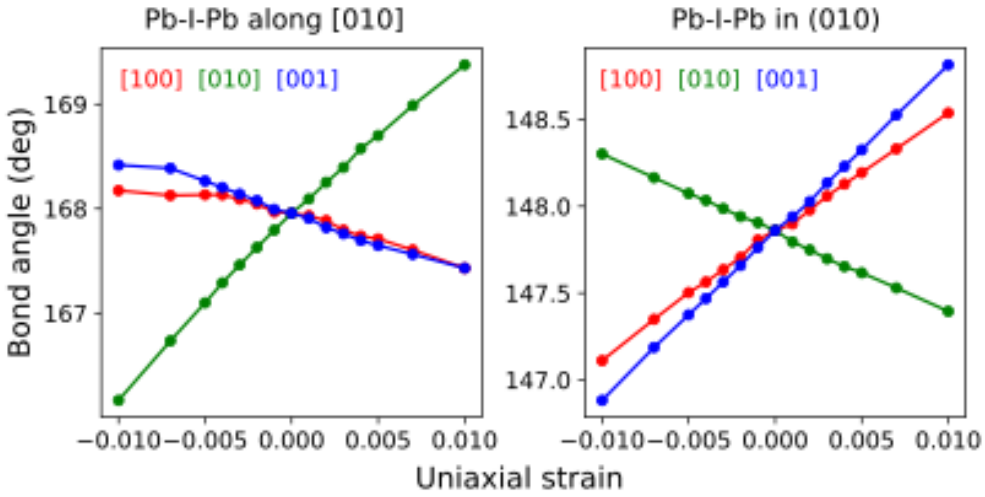

Figure 3.18: Change in Pb-I-Pb bond angle in orthorhombic MAPI due to uniaxial compressive and tensile strain along [100], [010], and [001] directions.

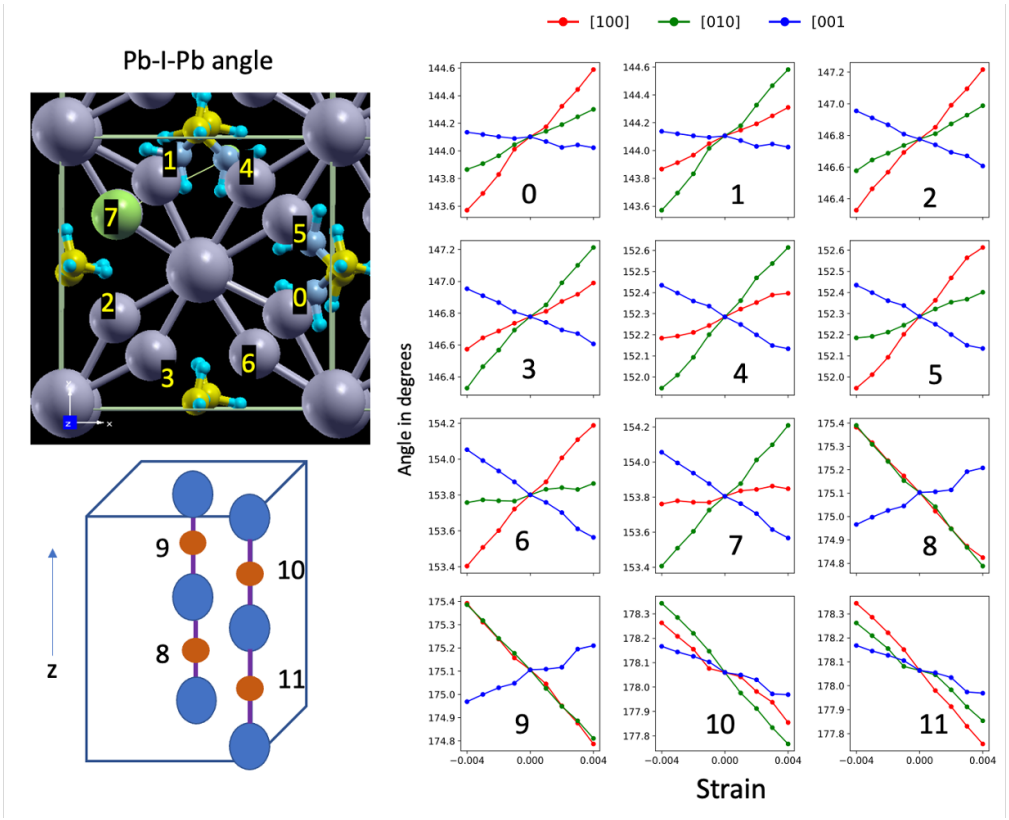

Figure 3.19: Change in Pb-I-Pb bond angle in tetragonal MAPI due to uniaxial compressive and tensile strain along [100], [010], and [001] directions.

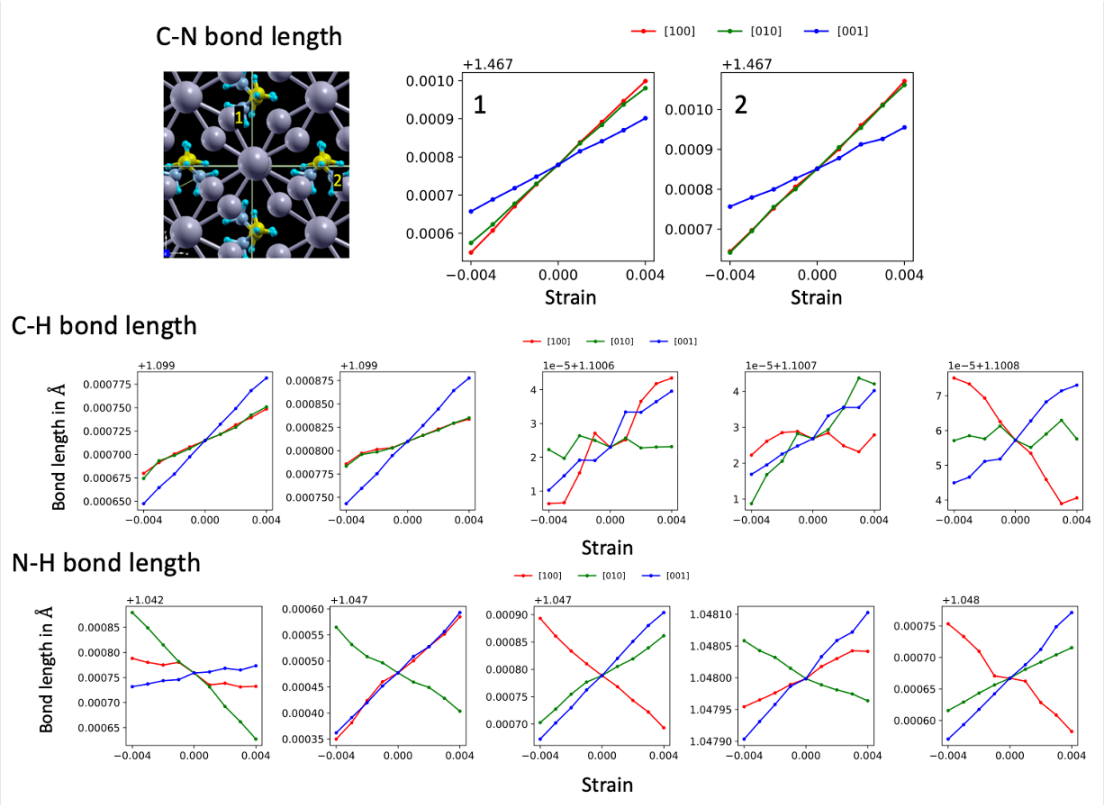

Figure 3.20: Change C-N, C-H, and N-H bond lengths in tetragonal MAPI due to uniaxial compressive and tensile strain along [100], [010], and [001] directions. This figure clearly shows that the methylammonium ions inside the Pb-I cage get affected due to stress.

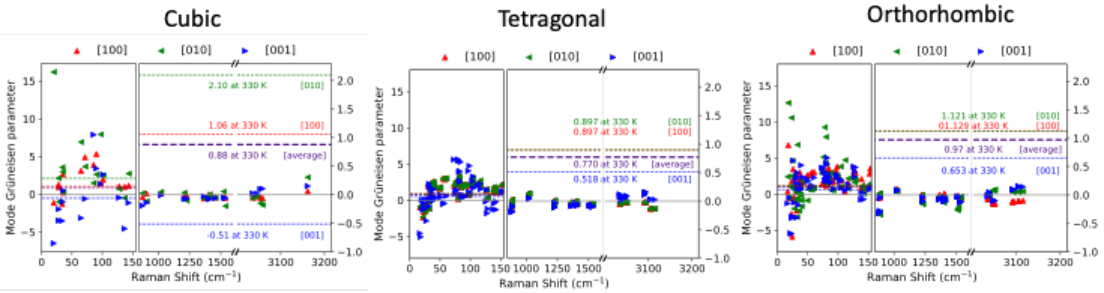

Figure 3.21: Comparison of mode-Grüneisen parameters for uniaxial strain along [100], [010], and [001] directions.

Chapter 4

Probing The Hidden Symmetry in Tetragonal $CH_3NH_3PbI_3$ Perovskite

4.1 Abstract

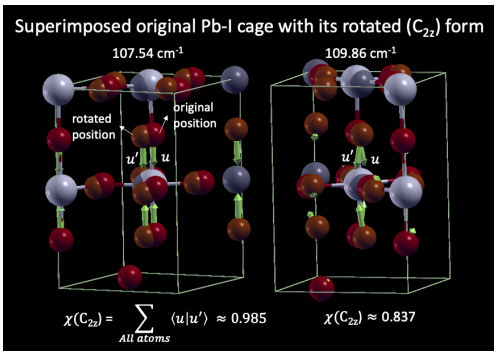

The assignment of exact space group to tetragonal $CH_3NH_3PbI_3$ perovskite structure is experimentally challenging and well debated. In experiment the rotation of the $CH_3NH_3^+$ ions within the Pb-I cage is averaged over space and time to measure symmetry but it is hard to get any exact symmetry of the structure for a static density functional theory calculation. Due to this lack of symmetry, it is not possible to calculate any exact irreducible representation for its vibrational modes. In this work we have developed a methodology to calculate the hidden symmetry of this quasi-symmetric tetragonal structure using group theory which can be helpful for spectroscopic study. We have also shown that the overall symmetry can be better explained with lower symmetry subgroups such as I4cm and C_{2v} of the I4/mcm space group. Our methodology can also be useful to find symmetry and approximate mode irreducible representation for any approximately symmetric material.

4.2 Introduction

Hybrid organometallic perovskites are one of the most researched material for solar cell application in last decade. There are more than sixteen thousand research documents published between 2009 to 2019 regarding perovskite solar cell.[125] A huge amount of research has been done towards low-cost fabrication, increasing the photo-conversion efficiency, making active layer materials etc. But in-depth understanding about some fundamental aspects is still missing. The exact symmetry of tetragonal methylamonium lead iodide (MAPI) is one of them. There is still debate about the space group symmetry of the tetragonal MAPI. Some reports suggest that the structure is ferroelectric or polar having quasi I4cm space group symmetry[132, 155] while others have found tetragonal MAPI structures that are antiferroelectric or anipolar in nature, having quasi I4/mcm space group symmetry[109, 151, 35](figure 4.1) There are also report that identified the space group as I4/m[6]. There are experiment that reports the structure to have space groups I422 and $P4_22_12$ which are subgroups of I4/mcm.[4]

It is important to know the symmetry of the tetragonal structure because two different structures (I4cm and I4/mcm) have different electronic properties. I4/mcm is a centrosymmetric structure with inversion symmetry and theoretically it should not produce Rashba splitting in the bandstructure while I4cm is a non-centrosymmetric structure without the inversion symmetry and it produce significant Rashba splitting.[36] Any reported significant Rashba splitting in case of I4/mcm structure is incorrect and may be it is due to their incorrect structural relaxation.[36] The energy difference between a quasi I4cm and a quasi I4/mcm structure is very small (0.1 eV) and they can coexist in a single crystal with domains of altering tilting directions which can further dynamically interchange into each other at room temperature crossing some energy barrier that caused due to the specific interaction between the MA^+ ion and the inorganic cage[112]. Another reason might be when the material goes through phase transition from cubic to teragonal structure due to temperature changes, it loses some symmetry elements which gives rise to twinning along the lost symmetry element.[14] In experiment, we mainly get the overall symmetry of the whole crystal, but sometimes the unit cell might have different symmetry due to such twinning within the crystal.

In case of the experimental structure, each MA^+ ion is statistically distributed with a fractional occupation of 25% for each of 4 orientation.[4] This arrangement gives the experimental structure proper symmetry. To do any theoretical calculation we must

take a snapshot of multiple possible orientations of the MA^+ ion and at that moment we lose all the symmetry. Quarti et al., has done a detailed study of the tetragonal structure and found that a set of polar structures (I4cm) are more stable than the apolar (I4/mcm) ones.[112] The most stable structure reported in their study is a polar structure with I4cm space group symmetry and this structure is used by other works[15, 30] and incorrectly mentioned as I4/mcm.

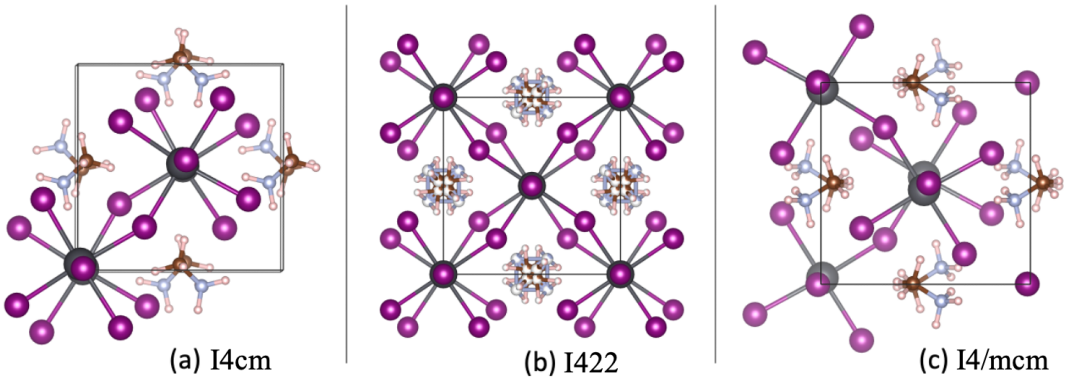

Figure 4.1: Tetragonal MAPI with different spacegroup symmetries: (a) I4cm (C_{4v}) structure, (b) experimental structure (D_4) (c) I4/mcm (D_{4h}), having the full symmetry of the tetragonal structure.

In case of low temperature orthorhombic structure, 4 MA^+ ions in the unit cell are static which gives it a perfect D_{2h} symmetry whereas for high temperature cubic symmetry, the random spinning of the MA^+ ion within the cage makes the structure pseudo-cubic. For room temperature tetragonal structure, the average over space and time of this random spinning makes this structure a quasi-I4cm or quasi-I4/mcm. So, the tetragonal MAPI does not have any exact symmetry. We want to see if symmetries such as I4cm or I4/mcm is enough to explain the structure or there are any low symmetry subgroups that elucidates the symmetry better for this tetragonal structure. To identify the hidden symmetry in the structure we have checked the symmetry from different aspects: (a) symmetry in the structure, (b) symmetry in the vibrational modes, (c) symmetry in the elastic tensor (or stiffness matrix), (d) symmetry in dielectric tensor, (e) symmetry in the electro-optic tensor, (f) symmetry in the dynamical matrix, (g) symmetry in the Born effective charge, and (h) symmetry in the Raman tensor. Depending on the result we classify the lower symmetry subgroups that explains the symmetry in the tetragonal

structure better.

For any crystal structure that has exact symmetry vibrational modes can be classified according to irreducible representations, but this can not be done when the structure does not have any symmetry. In this work, we have developed a method to calculate the approximate irreducible representation of the vibrational modes for an approximately symmetric structure. We use the nearby exact symmetry of the crystal structure and its character table as our input and use group theory to calculate approximate characters in the character table and thereby calculate the irreducible representations of the vibrational modes. We have calculated the contributions of irreducible representations for each phonon mode of tetragonal MAPI which can be helpful for spectroscopic studies. As a test of our methodology, we have also calculated the same for perfectly symmetric orthorhombic MAPI and TiO_2 and it gives correct irreducible representations for both the systems compared with quantum espresso results. Our methodology can be useful to calculate hidden symmetry and approximate mode irreducible representations for any approximately symmetric structure.

4.3 Computational method

We have studied two different tetragonal structures, one is quasi-I4cm[15] and the other is quasi-I4/mcm[77]. We did a full structural relaxation of both the initial structures using local density approximation[101] (LDA) with the Perdew-Wang (PW) parametrization[104] for the exchange correlation potential. We have used scalar relativistic optimized norm-conserving Vanderbilt (ONCV) pseudopotentials[53] from Pseud$\bar{o}$ D$\bar{o}$j$\bar{o}$[146]) (NC SR ONCVPSP v0.4) with standard accuracy. Half shifted 5$\times$ 5$\times$ 4 Monkhorst-Pack grid is used for Brillouin zone sampling along x, y, and z directions of the crystallographic axes with energy cutoff of 80 Ry for the wave functions. Variable-cell relaxation is done using a 0.5 kbar stress convergence threshold keeping total force per atom less than 1 meV/Å. Before deep diving into the symmetry of the tetragonal structure we have compared different functionals and compared the structural parameters. PBE with Van Der Waals corrections using Grimme-D2 gives best result for structural parameters compared to the experimental results but we have chosen LDA because the Raman intensity can only be computed using it in QUANTUM-Espresso and earlier report suggests that LDA without van der Waals correction can still be good to calculate Raman and IR frequency and intensity for orthorhombic MAPI.[105] We

have calculated the stiffness matrix by applying uniaxial strain to these two structure and calculating the stress tensor using quantum ESPRESSO. The method of calculating stiffness tensor is given in detail in chapter 5. The dielectric and the electro-optic tensor is calculated using quantum ESPRESSO ph.x code which uses density functional perturbation theory to calculate these tensors.

4.4 Theory to calculate irreducible representations

Our tetragonal structures in this work does not have any exact symmetry and hence no irreducible representations for their vibrational modes. we can still calculate the approximate mode irreducible representations using help of group theory. The well known formula for decomposition of reducible representation into its corresponding irreducible representations is given in equation (4.1)[54]. The number of times the irreducible representation Γ_j appears in the reducible representation is given by a_j, where h is the order of the point group, C_k denotes a class in the point group, N_k is the number of elements in C_k and $\chi^{(\Gamma_j)}(C_k)$ represents the character of the irreducible representation Γ_j for a symmetry operation in class C_k.

$$a_j = \frac{1}{h}\sum_k N_k[\chi^{(\Gamma_j)}(C_k)]^*\chi(C_k) \tag{4.1}$$

The second orthogonality rule for the columns of the character table is given in equation (4.2)

$$\sum_j [\chi^{(\Gamma_j)}(C_k)]^*\chi^{(\Gamma_j)}(C_{k'}) = \frac{h}{N_k}\delta_{kk'} \tag{4.2}$$

For $k = E$ (identity operation), $N_k = 1$. So we can rewrite equation (4.2) as

$$\sum_j [\chi^{(\Gamma_j)}(E)]^*\chi^{(\Gamma_j)}(C_{k'}) = h\delta_{Ek'} \tag{4.3}$$

$\chi^{(\Gamma_j)}(E) = 1$ for A or B (non degenerate) irreducible representation, $\chi^{(\Gamma_j)}(E) = 2$ for E (doubly degenerate) and $\chi^{(\Gamma_j)}(E) = 3$ for T (triply degenerate) irreducible representations.

Multiplying equation (4.1) with $\chi^{(\Gamma_j)}(E)$ and summing over j we get

$$\begin{aligned}\sum_j \chi^{(\Gamma_j)}(E)a_j &= \frac{1}{h}\sum_k \sum_j \chi^{(\Gamma_j)}(E)[\chi^{(\Gamma_j)}(C_k)]^*\chi(C_k) \\ &= \frac{1}{h}\sum_k h\delta_{Ek'}\chi(C_k) \\ &= \chi(E)\end{aligned} \tag{4.4}$$

It is interesting to note that when we sum over the contributions (a_j) of all irreducible representations for any mode, it turns out exactly 1 for non degenerate mode, 2 for doubly degenerate, and 3 for triply degenerate modes. To make the sum 1 for all the modes we have to divide $\chi(E)$ by 2 for for doubly degenerate, and by 3 for triply degenerate modes.We have used equation 4.1 to calculate a_j and then use equation 4.4 to find out the proportion of irreducible representations for each mode.

4.5 Results and Discussion

4.5.1 Symmetry in the crystal structures

To check the initial symmetry of the structures we have used FINDSYM[131, 130]. The result is given in table 4.1. As we already know that the theoretical structure does not have any symmetry due to the different orientations of the MA^+ ions within the structure, we have removed all the MA^+ ions from the I4cm structure and checked the symmetry of the Pb-I cage only structure. With some tolerance with respect to the lattice and the atomic positions, we found that the Pb-I cage still holds the D_{4h} point group symmetry. One thing to notice here is that the Pb-I cage and the whole structure both have symmetry C_s which is a subgroup of D_{4h}, even with low tolerance values. We will come back to this point while explaining phonon mode symmetries. For the I4/mcm structure, even with low tolerance values, the predicted symmetry by FINDSYM is C_{2v} which is a symmetry of an orthorhombic structure and lower in symmetry than D_{4h}. This gives an indication that the tetragonal symmetry may be well explained using some lower symmetry subgroups of D_{4h}.

4.5.2 Symmetry in elastic tensors

We have calculated the full stiffness tensor for both of our quasi-I4cm and the quasi-I4/mcm structures. The results are shown in figure 4.2. For tetragonal (I) crystal

Table 4.1: Tetragonal (I4cm) MAPI symmetry of the entire structure and only the Pb-I cage, calculated using FINDSYM[131, 130].

Tetragonal MAPI	Tolerance in lattice (Å)	Tolerance in atomic positions (Å)	Calculated symmetry
Complete Structure	0.001	0.001	no symm.
	0.2	0.2	C_s
	0.5	0.5	C_s
Pb-I cage only	0.01	0.01	C_s
	0.01	0.1	C_s
	0.1	0.1	C_s
	0.1	0.2	C_{2h}
	0.1	0.3	C_{2v}
	0.1	0.4	D_{4h}

system[89] we should have $C_{11} = C_{22}$, C_{33}, $C_{44} = C_{55}$, C_{66}, C_{12}, and $C_{13} = C_{23}$. The stiffness tensor for quasi-I4cm structure is closely following the tetragonal (I) symmetry, except there are small off diagonal values because the structure is not exactly symmetric. For stiffness tensor of I4/mcm structure all the diagonal values are different and C_{13} is not same as C_{23}. This is not even close to tetragonal (I) symmetry, it is more like orthorhombic symmetry as can be seen in figure 4.2. Applying symmetry rotations that belongs to D$_4h$ point group to the stiffness matrix it is possible to quantify how each symmetry is obeyed by the stiffness matrix of both the structures. The method for applying such rotations to the stiffness matrix is explained in chapter 5.

4.5.3 Symmetry in dielectric tensors

We have calculated the electronic (ϵ_∞) and electronic+ionic contribution (ϵ_0) of the dielectric tensor for our tetragonal MAPI structures (Fig. 4.3). For a perfectly symmetric tetragonal structure we should have only the diagonal values with ($\epsilon_{11} = \epsilon_{22}$). These off-diagonal values are also an indication that the structure is not properly symmetric. Although, the off diagonal are close to zero for I4/mcm structure, I4cm structure obeying the tetragonal symmetry better than I4/mcm. The dielectric tensor for the I4cm structure also obeys S_4, D_{2d}, C_4, C_{4v}, D_4 and D_{4h} point group symmetries and for I4/mcm structure, the dielectric tensor obeys C_{2v}, D_2, and D_{2h} point group symmetries.

Stiffness tensor (calculated values are in GPa)

$$\begin{pmatrix} C_{11} & C_{12} & C_{13} & & & \\ . & C_{11} & C_{13} & & & \\ . & . & C_{33} & & & \\ & & & C_{44} & & \\ & & & & C_{44} & \\ & & & & & C_{66} \end{pmatrix} \qquad \begin{pmatrix} 28.95 & 19.98 & 10.27 & -0.71 & 0.00 & 0.34 \\ 19.92 & 28.94 & 10.27 & 0.01 & -0.71 & 0.34 \\ 10.27 & 10.27 & 44.15 & 0.44 & 0.49 & 0.75 \\ -0.71 & -0.01 & 0.46 & 3.84 & 0.40 & 0.40 \\ -0.03 & -0.72 & 0.49 & 0.40 & 3.84 & 0.40 \\ 0.34 & 0.32 & 0.76 & 0.40 & 0.41 & 12.34 \end{pmatrix}$$

tetragonal-(I) I4cm

$$\begin{pmatrix} C_{11} & C_{12} & C_{13} & & & \\ & C_{22} & C_{23} & & & \\ & & C_{33} & & & \\ & & & C_{44} & & \\ & & & & C_{55} & \\ & & & & & C_{66} \end{pmatrix} \qquad \begin{pmatrix} 29.24 & 20.24 & 10.73 & 0.00 & 0.00 & -0.02 \\ 20.20 & 27.90 & 10.14 & 0.01 & 0.00 & -0.02 \\ 10.68 & 10.18 & 43.32 & -0.01 & 0.00 & 0.01 \\ 0.00 & 0.00 & 0.00 & 4.10 & 0.00 & 0.00 \\ 0.00 & 0.00 & 0.00 & 0.00 & 2.88 & 0.00 \\ 0.00 & 0.00 & 0.00 & 0.00 & 0.00 & 12.26 \end{pmatrix}$$

orthorhombic I4/mcm

Figure 4.2: Stiffness matrix calcuculated for quasi-I4cm and quasi-I4/mcm structures and compared with the tetragonal-(I)[89] and orthorhombic symmetry.

4.5.4 Symmetry in electro-optic tensor

We have calculated the non-linear electro-optic tensors $\chi^{(2)}$[36] for both quasi-I4cm and quasi-I4/mcm structures. The calculated values are in Rydberg atomic units. Our structures are not perfectly symmetric, so it is not guaranteed that electro-optic tensors will vanish. For quasi-I4/mcm structure all the values are close to zero except high value at $\chi^{(2)}_{zzz}$, ≈ 30.19. For I4cm structure it does not vanish, which is a clear indication that our quasi-I4cm structure is non-centrosymmetric and we have further checked all the symmetries that $\chi^{(2)}$ for a non-centrosymmetric structure should obey[123]. We see that $\chi^{(2)}_{zzz} = 22.73$ is large compared to other values. $\chi^{(2)}_{xxx} \approx \chi^{(2)}_{yyy} \approx 3.125$ which are supposed to be zero for all tetragonal symmetries. Doing some further analysis we found that C_s, C_4 and C_{4v}, and D_{4h} point groups are compatible with nonzero $\chi^{(2)}_{zzz}$.

4.5.5 Symmetry in Born Effective Charge

The Born effective charge $Z_{\alpha ij}$ is calculated for both I4cm and I4/mcm structures using quantum espresso. The detail of the theory is given in chapter 1. Here α is

$$\text{I4cm}: \quad \epsilon_\infty = \begin{pmatrix} 5.941 & 0.037 & -0.013 \\ 0.037 & 5.941 & -0.013 \\ -0.013 & -0.013 & 5.978 \end{pmatrix} \quad \epsilon_0 = \begin{pmatrix} 18.065 & 0.173 & -0.146 \\ 0.173 & 18.066 & -0.146 \\ -0.146 & -0.146 & 16.513 \end{pmatrix}$$

$$\text{I4/mcm}: \quad \epsilon_\infty = \begin{pmatrix} 5.962 & 0.000 & 0.000 \\ 0.000 & 5.932 & 0.000 \\ 0.000 & 0.000 & 6.071 \end{pmatrix} \quad \epsilon_0 = \begin{pmatrix} 18.257 & 0.000 & 0.000 \\ 0.000 & 18.152 & 0.001 \\ 0.000 & 0.001 & 16.613 \end{pmatrix}$$

Figure 4.3: Dielectric tensor (ϵ_∞) which is static with only electronic contribution and (ϵ_0) which is static with electronic and ionic contribution, for quasi-I4cm and quasi-I4/mcm structures.

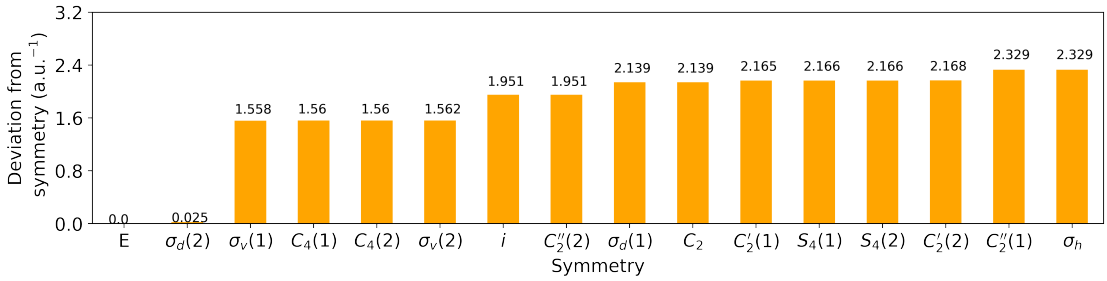

(a) I4cm

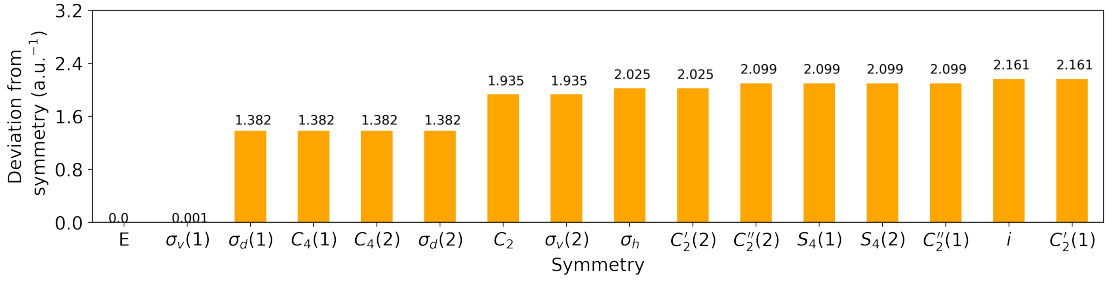

(b) I4/mcm

Figure 4.4: Born effective charge tensor symmetry

the atom index and i, j represents the x, y, and z coordinates. If the structure obeys the symmetry perfectly then equation 4.5 returns zero because the born effective charge also obeys the symmetry. We have calculated the deviation from symmetry of born effective

charge tensor (figure 4.4). Here we can see that the symmetries that belongs to the same class gave same value for the deviation of symmetry. This can be understood from the fact that those symmetries are related σ_d for I4cm and σ_v for I4/mcm which obeyed almost perfectly.

$$\sqrt{(\sum_{\alpha ij} |Z_{\alpha ij} - \sum_{\alpha' i' j'} M_{ii'} M_{jj'} M_{\alpha\alpha'} Z_{\alpha' i' j'}|^2)} \tag{4.5}$$

4.5.6 Symmetry in Raman Tensor

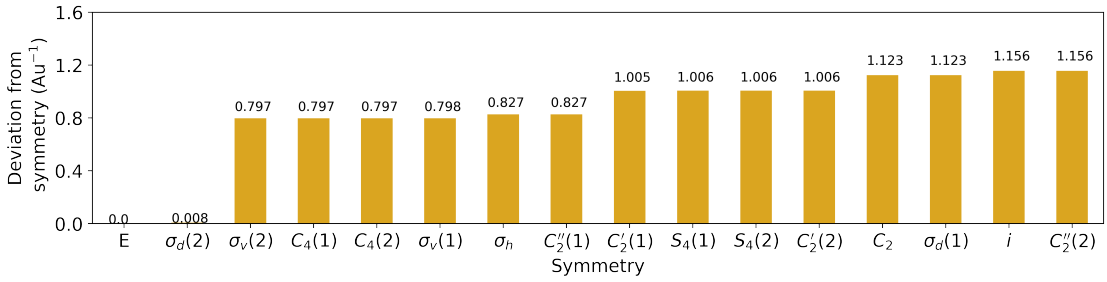

(a) I4cm

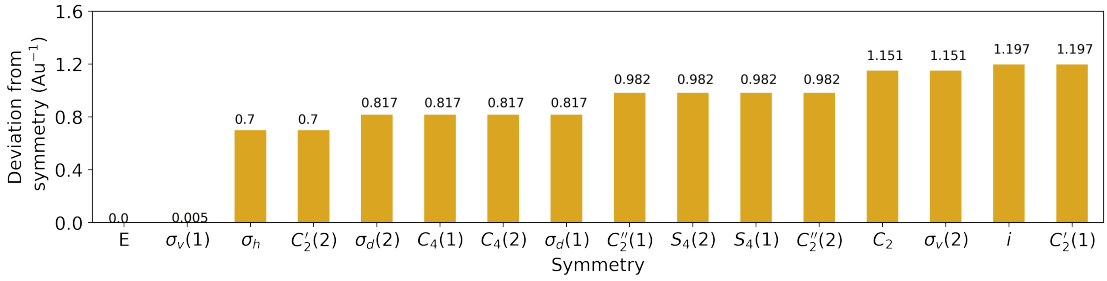

(b) I4/mcm

Figure 4.5: Raman tensor symmetry

Raman tensor $R_{ijk\alpha}$ is calculated using density functional perturbation theory as implemented in quantum ESPRESSO. The theory is explained in chapter 1. Here we have checked how much symmetry is obeyed by the Raman tensor for each structure by calculating the deviation from symmetry using equation 4.6. The result is plotted in sorted order for both I4cm and I4/mcm structures. Here also, we can see that the symmetries that belongs to the same class gave same result. The reason is same as explained for Born effective charge symmetry.

$$\sqrt{(\sum_{ijk\alpha} |R_{ijk\alpha} - \sum_{i'j'k'\alpha'} M_{ii'}M_{jj'}M_{kk'}M_{\alpha\alpha'}R_{\alpha'i'j'k'}|^2)} \tag{4.6}$$

4.5.7 Symmetry in Dynamical Matrix

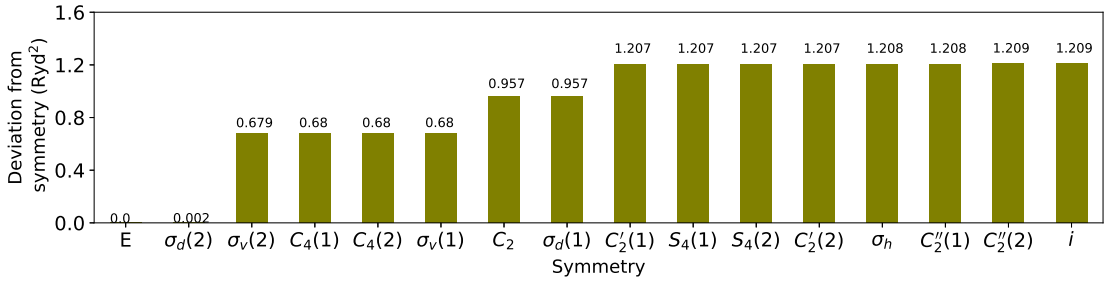

(a) I4cm

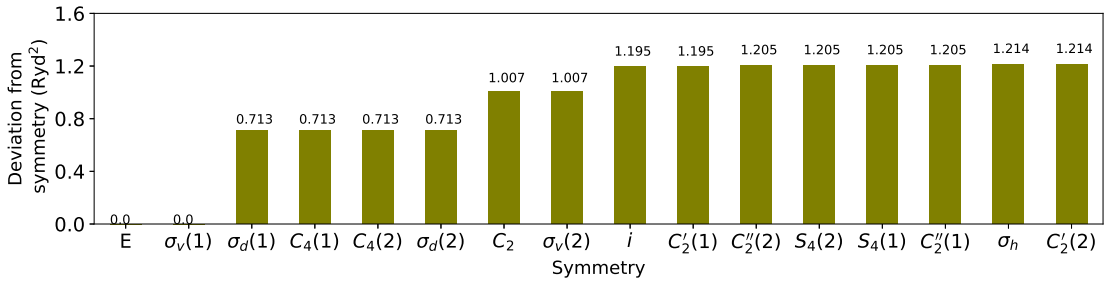

(b) I4/mcm

Figure 4.6: dynamical matrix symmetry

The dynamical matrix $D^s_{i\alpha j\beta}$ is calculated using the density functional perturbation theory as discussed in chapter 1. To check the symmetry of the dynamical matrix with respect to all the symmetry operations we have calculated the deviation of symmetry using equation 4.7. The result shown in figure 4.6. Similar trend that the symmetries that belongs to the same class gave same result is also true in this case.

$$\sqrt{(\sum_{ij\alpha\beta} |D^s_{i\alpha j\beta} - \sum_{i'j'\alpha'\beta'} M_{ii'}M_{\alpha\alpha'}M_{jj'}M_{\beta\beta'}D^s_{\alpha'i'j'\beta'}|^2)} \tag{4.7}$$

4.6 Symmetry in Vibrational Modes

We have built a methodology using group theory that will help us to calculate approximate vibrational mode symmetries for a crystal structure that is not perfectly

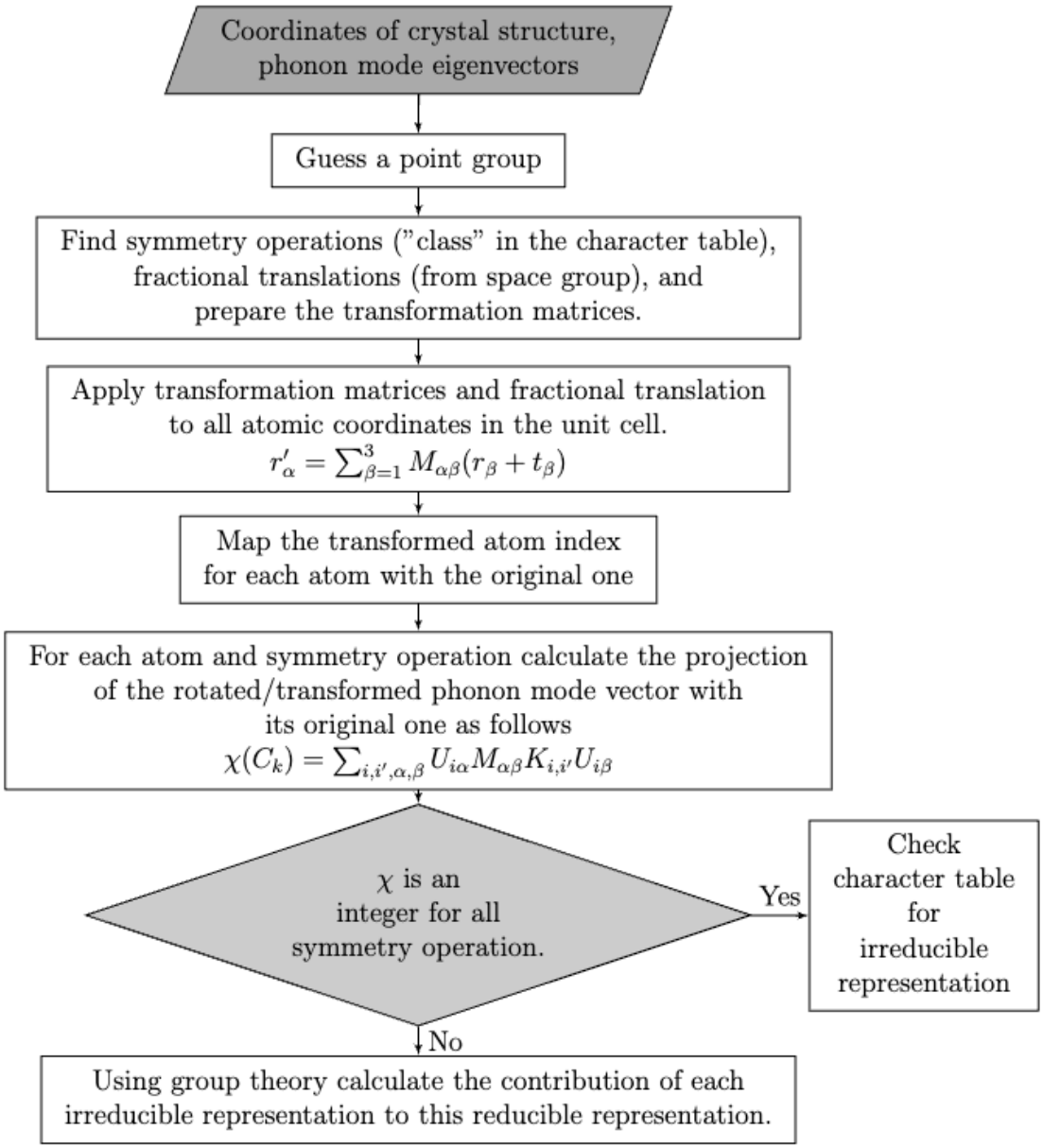

Figure 4.7: Approximate phonon mode symmetry calculation flow chart.

symmetric but a close one. The main process is explained in the form of a simple flow chart (Fig. 4.7). We started with the I4cm structure. We have relaxed the structure using as mentioned in the computational method section. Density functional perturbation theory (DFPT) is used to calculate the phonon modes at q=0. Acoustic sum rule (ASR) is applied using the dynmat.x code as implemented in quantum ESPRESSO. We have taken the position coordinates of the relaxed structure and its calculated phonon mode

vectors as input. The closest symmetry of the structure we considered is I4/mcm (or D_{4h} point group), because this is the highest symmetry in tetragonal structure and if we calculate this once, we can always get results for I4cm as it is a subgroup of I4/mcm. From the character table of D_{4h}, we get all the symmetry operations (16 in our case) and the target irreducible representations[41]. From the space group we find all the fractional translations that are involved. We have constructed all the 3×3 rotational matrices ($M_{\alpha\beta}$) and the fractional translation vector ($\vec{t}$) to apply on the original atomic positions ($\vec{r}$) of the crystal unit cell as $r'_\alpha = \sum_{\beta=1}^{3} M_{\alpha\beta}(r_\beta + t_\beta)$ where α and β denotes the x, y, and z directions. To make the calculations simple, we started with the Pb-I cage only. Because the orientation of the MA^+ ions in the structure breaks the symmetry. and Pb-I cage still holds the D_{4h} point group symmetry within certain tolerance values (table 4.1). After removing the MA^+ ion from the structure, we have applied all the symmetry operations on the structure and find out the swapped atoms. When we apply rotation to the crystal structure, if for example, a carbon atom (C1) take place of another carbon atom (C2), we say C1 and C2 are swapped atoms of each other with respect to that rotation. Vibration modes should obey certain symmetry operations based on the symmetry of the crystal structure. We apply the symmetry transformation to the vibrational mode Cartesian vectors and calculate the projection of the transformed mode vector to the original one for each atom and the value will give us the character value χ corresponding to that symmetry class for that mode. The equation for calculating the projection is

$$\chi(C_k) = \sum_{i,i',\alpha,\beta} U_{i\alpha} M_{\alpha\beta}(C_k) K_{i,i'}(C_k) U_{i\beta} \tag{4.8}$$

where i and i' denotes the atom index of the original and transformed atoms respectively, $K_{i,i'}(C_k)$ denotes the matrix that transforms i to i' and $U_{i\alpha}$ denotes the mode vector for atom i in direction α, C_k denotes the symmetry class for which χ is been calculated.

To calculate the character we need the mode eigenvector for that particular mode. Its important to note that the phonon mode vectors that directly come out of the Quantum ESPRESSO dynmat.x code output is normalized to 0.1 and not normalized with the corresponding atomic masses and hence are not orthogonal to each other, they are just mode displacement vectors. To make these modes orthogonal mode eigenvectors we need to normalize them with corresponding atomic masses. This means we need to multiply each mode eigenvector with the corresponding mass of the atom and then normalize them to 1. Our method should work fine even if we do not normalize

these modes with respect to mass but we normalized them properly before doing further calculations because this will help up later to find the degeneracy in the modes later. Once we remove the MA^+ ions we need to re-normalize the mode vectors ($\vec{U_i}$) for Pb and I as $\vec{U_i}(normalized) = \frac{\vec{U_i}}{\sqrt{(\sum_{i=1}^{N}|\vec{U_i}|^2)}}$ where i is the atom index and N is the total number of atom after removing all the MA^+ ions. We calculated the value of χ for all symmetry classes and for each mode of the tetragonal MAPI. As our structure is not exactly symmetric, we did not expect to get integer values for χ for all the symmetry classes, in fact our calculated values are in fractions. So, we need to find a different way rather than checking character table for a direct match as we have already mentioned in the flowchart(Fig.4.7).

For each phonon mode we have calculated $\chi(C_k)$ for all symmetry class C_k belonging to the point group D_{4h} and prepared a table which we call calculated character of modes because it is like a character table but with character values in fractions rather than in integers as we normally see in a character table. Each row of this calculated character of mode table is treated as a reducible representation and we decompose them into the irreducible representations using group theory (Eqn. 4.1).

We noticed that the sum of contributions of all the irreducible representations become 1 for all the modes. We gave a theoretical explanation why this occurs using group theory (Eqn. 4.4). If we just sum up the contributions (a_j) for all irreducible representations we end up getting sum as 2's and 3's for doubly degenerate or triply degenerate modes which is a problem because in that case the contribution of irreducible representations for each mode does not sum up to one, which makes it hard to compare between all the modes. We have studied it further by decomposing the degenerate modes into a possible combination of two symmetrized non-degenerate modes by looking at how the basis function (x,y) transforms with different symmetry operations and repeated the same calculations for calculating a_j and this time it gave the sum as 1 but our symmetrized combination is just one of the many possible permutations of how (x,y) basis can transform under the symmetry operations. It become even harder when the character value become imaginary in some cases, for example, in the character table for C_3 point group the degenerate irreducible representation is a symmetrized combination of 1, $e^{\frac{i2\pi}{3}}$, and $e^{-\frac{i2\pi}{3}}$. The above problem is known as the doubling problem[17]. In our formulation of equation (4.4) we just have to divide the sum by 2 for the doubly degenerate mode as $\chi^{(\Gamma_j)}(C_E) = 2$ and this makes the sum of all the irreducible representations for each

mode (including the degenerate ones) as 1. So, we decided not to split the degenerate mode.

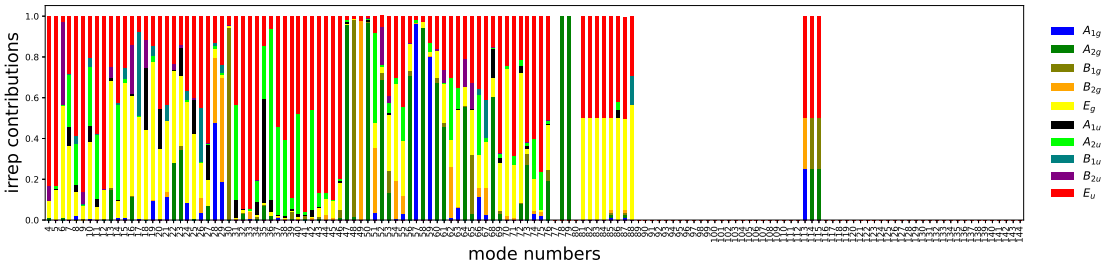

(a) I4cm (Pb-I cage only)

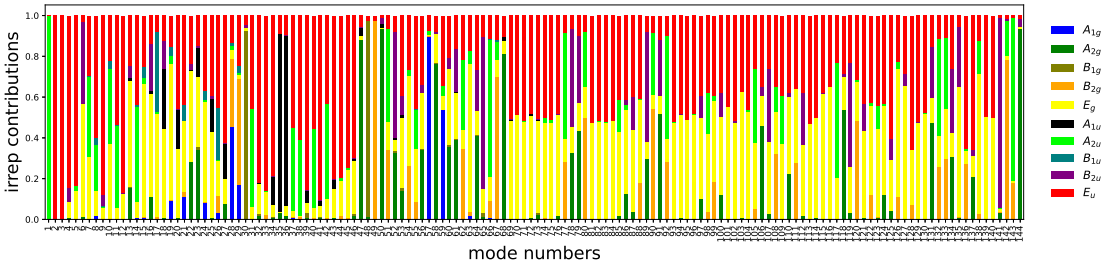

(b) I4cm complete sructure

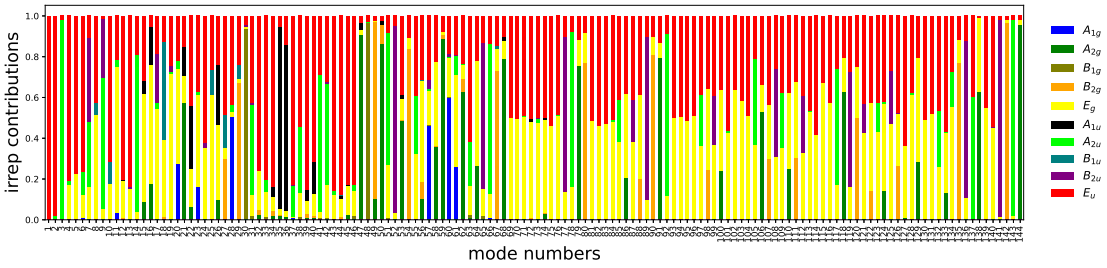

(c) I4/mcm complete structure

Figure 4.8: Contributions of different irreducible representations for each mode in (a) Pb-I cage only structure of I4cm symmetry, (b) full I4cm structure, and (c) full I4/mcm structure calculated considering the highest symmetry D_{4h} of the tetragonal structure.

The contribution of irreducible representations for each mode of Pb-I cage is shown in figure 4.8(a). Because the mid and high frequency modes does not have much Pb-I vibrations its not enough to get irreducible representations for all the modes of tetragonal MAPI just using only Pb-I cage. It also indicates that the high frequency modes are purely molecular modes. We need to consider the molecular vibrations if we want to calculate the irreducible representations correctly for mid and high frequency

modes. We decided to keep the C and N of the MA^+ ion with the Pb-I cage and not consider the H atoms which are randomly oriented anyway and hard to track after the rotational symmetry operation on the structure as they are more in number and close to each other in space. So, swapped H atoms is very hard to calculate or identify. Our reason of not considering H is also supported by the idea that, for orthorhombic MAPI we are able to calculate exact irreducible representations for each mode even without considering the H atoms in the structure and we have also checked that the contribution of the H atoms in each mode eigenvectors for both orthorhombic and tetragonal structure looks similar and the H mainly affects the high frequency modes (figure 4.9). We followed the same process as we mentioned earlier for Pb-I cage and calculated the contributions of the irreducible representations for phonon modes of both I4cm and I4/mcm tetragonal MAPIs. The result is given in figure 4.8(b,c). We can see that for low frequency modes, both Pb-I cage-only calculation and the entire structure (except H) give similar result, for mid frequency region the molecular modes change the irreducible representations that are coming from Pb-I only. It can be also seen that some modes obey the symmetry better than the others.

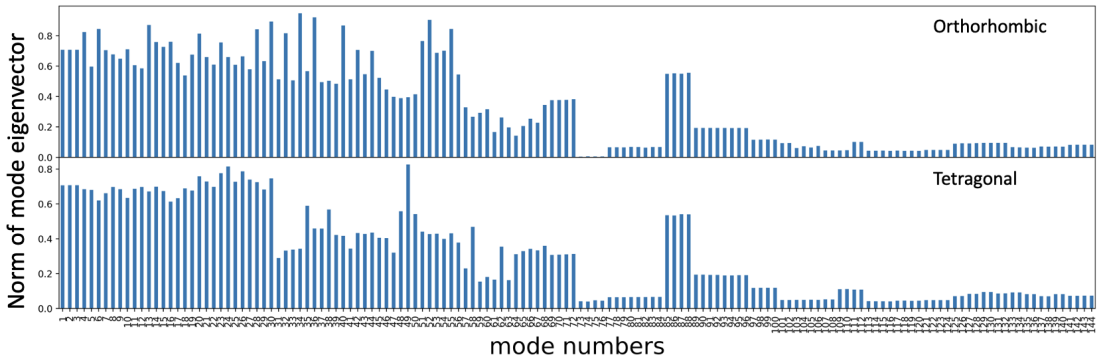

Figure 4.9: Contribution of norm of the vibrational mode eigenvectors for orthorhombic and tetragonal MAPIs.

Almost all the modes have some contributions from E_g and E_u representations. These are the degenerate representations. we have to identify which modes are purely degenerate. to do this we make a criteria where the sum of the contributions from E_g and E_u is greater than 80% of the total representations for any mode, and if the mode frequency are close to each other we considered those pair of consecutive modes as degenerate. The squared sum of the mode irreducible representation (χ^2) for any

particular class C_k should be equal to the total number of modes ($\sum_1^N \chi_{C_k}^2 = N$), in our case that is 144. For doubly degenerate modes, instead of χ^2 we need to take the sum of $2 \times (|\chi_1 + \chi_2| - 1)^2$ because in the symmetrized combination of degenerate mode it is possible that for a particular class C_k the $\chi(C_k)$ can be 1 and -1 which makes the total as zero in degenerate representation. The result is given in figure 4.10. For a symmetry operation, that the structure perfectly follow, the squared sum will be 144 (=the total number of modes). We can see that some of the symmetry operations such as C_4, C_2', S_4, σ_v, and σ_d are followed better over others. To avoid the arbitrary criterion of 80% and need to use D_{4h}, we can use some sophisticated mathematical techniques. We can construct the overlap matrix $S_{\mu,\nu} =< u_\mu | u_\nu >$ (This is basically the matrix we constructed for E) and use it to make things orthogonal. $P =< u_\mu | S^{-1} M | u_\nu >$ now is the matrix that we can use. Here M is the rotational matrix for a symmetry operation. For non degenerate modes we will get only diagonal values in P whereas for degenerate modes we can see off diagonal values which will indicate which modes are degenerate to each other. But this method is having some issues when we remove hydrogen atom from the structure. We are working on it to see if there are any other way we can calculate this.

To consider whether the vibrational modes of the ostensibly I4/mcm structure in fact obey the I4/mcm symmetry or some other subgroup, we have looked into the symmetry operations that are followed better by the structure and based on that we can get an idea. For example, we can see that σ_d is obeyed better than rest of the operations. So subgroup C_s can be a better fit. To check it even more rigorously, we have calculated the contribution of irreducible representations of vibrational modes based on each subgroup. We ranked each subgroup based on a value (RG) as given in equation 4.9.

$$RG = \sum_{modes(\nu)} \sum_{irrep(i)} \mu_{\nu,i}^2 \tag{4.9}$$

Here $\mu_{\nu,i}^2$ is the contribution of the irreducible representation i for mode ν. The sum should be equal to or less than the total number of modes, which is 144 in our case but will be less as our structure is not properly symmetric. This is because for a perfect irreducible representation of a mode, the maximum value of $\mu_{\nu,i}$ can be 1.

As a test case of our analytical method, we checked orthorhombic MAPI whose modes are all non degenerate and TiO_2 which has some doubly degenerate modes. Our

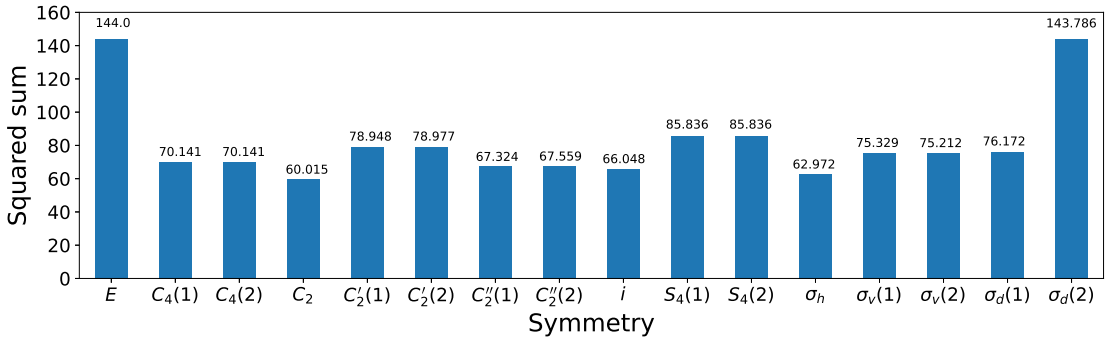

(a) I4cm

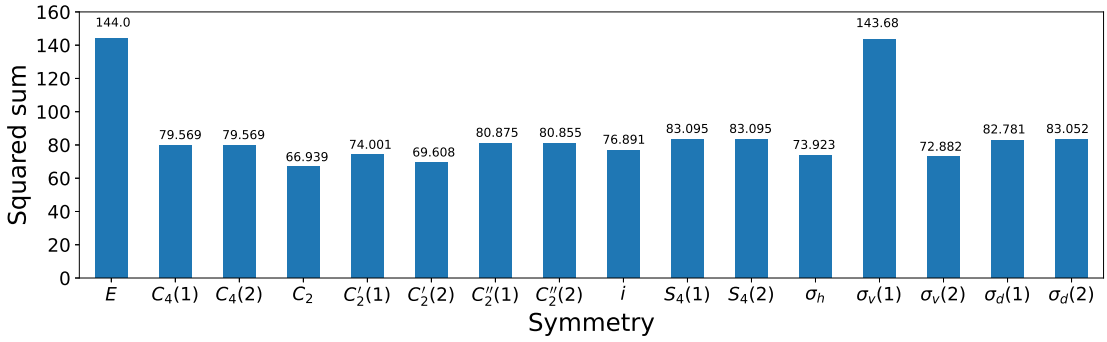

(b) I4/mcm

Figure 4.10: The squared sum of the mode characters (χ^2 for non degenerate modes and $2 \times (|\chi_1 + \chi_2| - 1)^2$ for doubly degenerate modes for each symmetry class over all the phonon modes of tetragonal MAPI.

method is able to calculate the mode irreducible representations for these two exactly symmetric structure (Figure 4.12) comparable to the quantum ESPRESSO ph.x output of the more irreducible representations. We are able to calculate the irreducible representations exactly even without considering the hydrogen atoms in the structure. Our result for orthorhombic structure also suggests that we should be able to calculate mode irreducible representation of tetragonal structures without considering the H atoms.

4.7 Conclusion

In this work we tried to find out the hidden symmetry in tetragonal MAPI structure which otherwise mainly known to be either quasi-I4cm or quasi-I4/mcm in theoretical calculations. Looking at different aspects of the symmetry, we find that the

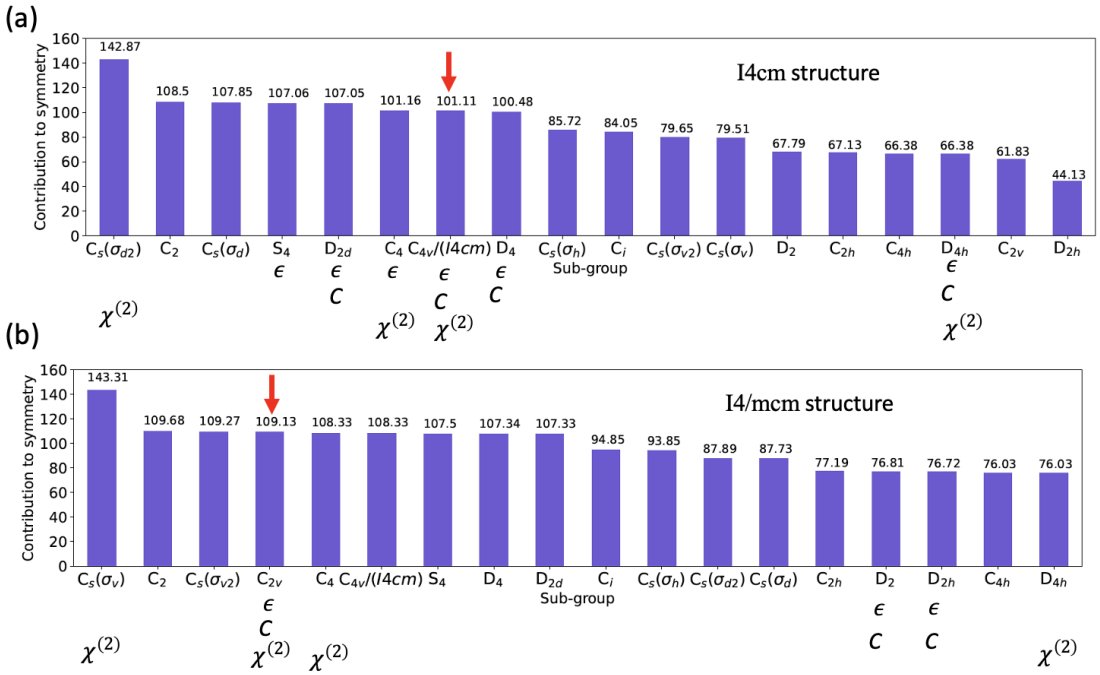

Figure 4.11: Rank of subgroups based on obeyed symmetry operation.

quasi-I4cm structure obeys I4cm symmetry better than other subgroups of I4/mcm but the quasi-I4/mcm structure obeys C_{2v} subgroup symmetry better compared to other subgroups of I4/mcm. We developed a methodology to calculate irreducible representations of the vibrational modes for these quasi structures which otherwise would not have been possible to calculate. Our methodology can be useful to calculate irreducible representations for any quasi symmetric material, for example doped structure, polycrystalline material or even amorphous material and be helpful to understand IR and Raman spectroscopy. Our detailed analysis of each symmetry operations that belongs to the highest tetragonal symmetry (D_{4h}) reveals that there is not much difference between these two structures with respect to centrosymmetricity. After considering all possible lower symmetry subgroups of I4/mcm, we found that C_{4v} or I4cm is the symmetry that represents tetragonal (I) structure and can be used to compare with the experimental structure.

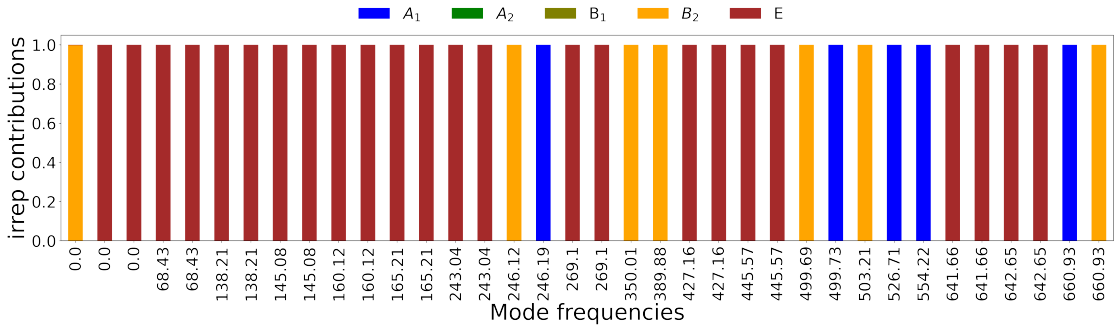

(a) TiO_2

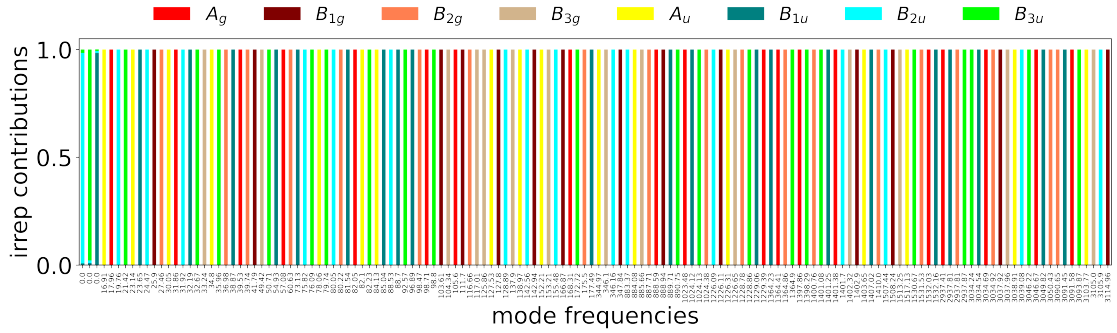

(b) Orthorhombic MAPI

Figure 4.12: Contribution of irreducible representations for (a) TiO_2 and (b) orthorhombic MAPI without considering the H atoms in the structure, calculated using our analytical method. All the mode frequencies are in $cm^{-}1$

4.8 Acknowledgement

This material is based upon work supported by the Air Force Office of Scientific Research under award number FA9550-19-1-0236. This work used computational resources from the Multi-Environment Computer for Exploration and Discovery (MERCED) cluster at UC Merced, funded by National Science Foundation Grant No. ACI-1429783, and the National Energy Research Scientific Computing Center (NERSC), a U.S. Department of Energy Office of Science User Facility operated under Contract No. DE-AC02-05CH11231.

Chapter 5

Mechanical Properties of Orthorhombic, Tetragonal, and Cubic $CH_3NH_3PbI_3$ Hybrid Perovskites: A Comparative Study

5.1 Abstract

The mechanical properties of hybrid perovskite materials are important for the behavior of flexible devices, resistance to fracture, epitaxial growth, surface energetics of quantum dots, and induction or relief of stress in thin films due to thermal expansion and phase changes. These issues are particularly salient for solar cells in space applications. Nonetheless few studies are available on the mechanical properties of $CH_3NH_3PbI_3$ (MAPI). Experimental results are only available for the room-temperature tetragonal phase, which have significant variation. Results from density functional theory (DFT) are available for all three phases but have even larger discrepancies from each other and from experiments. To bring order to the confusion in the literature, we have studied the elastic properties of all three phases in detail with DFT calculations. We have examined the effect of different aspects such as structure, exchange-correlation

functionals, van der Waals corrections, pseudopotentials, and other considerations in calculation methodology. Our results provide accurate reference values and an appropriate general methodology for elastic properties of metal halide perovskites.

5.2 Introduction

Recent research in hybrid organometallic perovskites have created a new avenue for making low cost, low temperature, easy to make photovoltaic devices with photoconversion efficiencies (PCE=25.7%[97]) comparable to its rival silicon. One hand suitable optoelectronic properties such as direct bandgap [36, 145], high absorption coefficient,[126] long diffusion length[133, 156] and high carrier mobility[150] make perovskites a promising candidate for solar cell, but on the other hand they suffer from serious degradation problems[96, 21, 62] which hinder their commercialization as solar cells. Mainly, the presence of oxygen[5] and moisture[96] rapidly accelerates the degradation in perovskites. However, these factors are not a concern in the vacuum of space. On top of that, high specific power (23 kW/kg)[63], low temperature easy in-situ fabrication in space[86], high defect tolerance[129] and lower cost per payload[86] are the prime reasons perovskite has gained attention for space applications.[144, 159] Beside having such benefits, it has to face some extra challenges in space. For example, it has to go through rapid temperature changes (roughly 300 K) within few hours, withstand high energy charged particle radiation[74], and face heavy mechanical damage due to space debris travelling at a speed of 10 km/s.[91]

Lots of research has been done to improve its photo conversion efficiency and stability but few research is available related to its mechanical properties which is utmost important for making a commercial solar cell for Earth or for space applications. Out of that few available research on mechanical properties, there are disagreements between theoretical as well as experimental results (table 5.1). There are many reasons that may affect the values of C_{ij} parameters of the stiffness matrix and thereby the elastic properties calculated based on it. Method of calculation, exchange correlation functionals, k-point sampling, energy cutoff for the plane wave, lattice parameters etc. can affect the values of C_{ij} in many ways. But there is a possibility of another reason behind such discrepancy which is wrong calculation. For example, most of the C_{ij} values and calculated elastic modulus as reported by Diao et al.[24] are far away from other reported calculations. They used supersoft pseudopotential which is supposed to be wrong. They

have also used increased number of empty bands and smearing to accelerate structural optimization which is not necessary. Their reported lattice parameter for orthorhombic structure seems same as reported in Feng et al., paper[31] and it appears they have not optimized the structure correctly which is also visible with the negative value reported for C_{66}. Their reported tetragonal structure parameter also same as cubic which is wrong. Young's modulus calculated in this paper differ more than 5 times as reported in other papers. Another paper by Ali et al.,[1] reports the formula wrong for calculating shear modulus G_V using Voigt approximation. Although the reported value for G_V appears to be correct using correct formula. When we calculated the Young's modulus (Using Hill approx. [56]) based on the C_{ij} parameters reported in Feng et al., paper, we found the result little different (reported 15 GPa, calculated 11.29 GPa). With all these reports its worth to dig deeper into the issue and before going any further it is most important that we use correct formula to calculate all these parameters and report clearly.

As part of our research, we have studied the mechanical properties of all three phases of MAPI in detail to find an agreement and root cause for the disagreement between different theoretical as well as experimental results (table 5.1). There is no experimental result available so far for cubic and orthorhombic structures reporting mechanical properties except high temperature tetragonal phase.[117, 113, 79, 20] Mainly nanoindentation technique has been used to calculate Young's modulus at different crystal surfaces. We have found one study that uses AFM to measure elastic modulus.[79] Theoretical results are available for all three phases but differ widely amongst each other and with experiments.[117, 31, 24, 65, 1, 119] We are doing a systematic study to understand and point out the reasons behind such discrepancy of earlier published results. We have done DFT calculations on all the three phases and calculated the whole stiffness C_{ij} and compliance matrices S_{ij}. With the help of compliance matrix and the matrix rotation method[140] we have calculated elastic modulus at certain directions which are reported in the experiments.[117, 136, 113, 79, 20, 117]

5.3 Methods

5.3.1 Computational Details

We have investigated mainly three different structures, pseudo-cubic[138], tetragonal and orthorhombic[15]. The orthorhombic structure is exactly symmetric having

Table 5.1: Calculated values of polycrystalline averages of bulk modulus K (GPa), shear modulus G (GPa), Young's modulus Y (GPa) and values of Young's modulus at crystallographic directions [100], [010], and [001]. Comparison with previously reported experimental and theoretical results.

Structure	**Polycrystalline average (Hill approx.)**			**Young's Modulus [100] GPa**	**Young's Modulus [110] GPa**	**Young's Modulus [112] GPa**	**Method**
	Bulk Modulus GPa	**Shear Modulus GPa**	**Young's Modulus GPa**				
Orthorhombic	20.22	7.69	20.48	20.18	14.25	16.31	DFT-LDA
	14.76	6.45	16.88	15.33	12.92	13.89	DFT-PBE
	17.072	7.136	18.79	17.981	13.478	14.672	DFT-PBEsol
	16.70	6.59	17.48	14.96	13.55	14.54	DFT-PBE+vdW-GD2
	16.70	6.87	18.13	14.95	13.71	14.99	DFT-PBE+vdW+HK
	15.87	6.64	17.48	17.95	12.91	13.93	DFT-PBE+vdW-GD3
	15.41	6.58	17.27	15.92	13.33	14.42	DFT-PBE-TM
	18.10	3.60	15.00	-	-	-	DFT-PBE+vdW[31]
	40.42	49.10	104.85	-	-	-	DFT-PBE-supersoft[24]
	16.76	7.32	19.17	-	-	-	DFT-PBEsol[1]
	15.45	6.59	17.31	-	-	-	DFT-PBE[1]
Tetragonal	20.33	6.84	18.45	14.80	31.61	15.84	DFT-LDA
	13.14	5.33	14.08	10.39	23.62	14.75	DFT-PBE
	17.07	5.76	15.53	14.90	24.79	13.02	DFT-PBE+vdW-GD2
	13.20	7.00	17.70	-	-	-	DFT-PBE[117]
	12.20	3.70	12.80	9.27	22.67	7.60	DFT-PBE+vdW[31]
	36.07	6.32	-	22.63	20.86	20.86	DFT-PBE[24]
	25.61	11.91	30.94	79.91	79.89	79.83	DFT-PBE[65]
	-	-	-	10.4±0.08	-	10.7±0.05	Nanoindentation[136]
	13.90	5.40	-	14.3±1.7	-	14.0±2.0	Nanoindentation[113]
	-	-	-	15.14	-	-	SPM/AFM[79]
	-	-	16.5±1.973	-	-	-	Nanoindentation[117]
	-	-	-	20±1.5	-	-	Nanoindentation[20]
Cubic	18.90	6.05	16.40	-	-	-	DFT-LDA
	16.40	16.40	22.20	-	-	-	DFT-PBE+vdW[31]
	54.08	2.93	-	-	-	-	DFT-PBE-supersoft[24]
	14.70	7.00	18.10	-	-	-	DFT-PBE-ultrasoft[119]

D_{2h} point group symmetry but the tetragonal structure does not have any symmetry on an atomistic level, though experimental measurement can show D_{4h} point group symmetry as discussed in chapter 4. We checked the effect of different exchange correlation functionals (LDA[104], PBE[102], and PBEsol[103]) and used scalar relativistic optimized norm-conserving Vanderbilt (ONCV) pseudopotentials[53] from Pseud$\bar{o}$ D$\bar{o}$j$\bar{o}$[146]) (NC SR ONCVPSP v0.4) with standard accuracy. We have also used a Troullier-Martins[142] pseudopotential for PBE to compare with the ONCV result. Different half-shifted Monkhorst-Pack grid (depending on the structure) is used for Brillouin zone sampling with energy cutoff of 80-100 Ry for the wave functions. Variable-cell relaxation is done using a 0.5 kbar stress convergence threshold keeping total force per atom less than 1 meV/Å. We have compared different Van der Waals correction schemes (Grimme-D2[50], Grimme-D3[51], TS[141]) as available in Quantum ESPRESSO. The applied strain range for this calculation is between -0.1 to +0.1.

5.3.2 Theoretical Frame-work

Idea of Calculating Stiffness Constants

As we have mentioned in the introduction section about large discrepancies in reported mechanical properties of $CH_3NH_3PbI_3$ hybrid perovskites, it is important that we clearly mention all the formulas and techniques that we have used to calculate them. A very well known formula to calculate stiffness constants is Hooke's law which states that within elastic limit, stress is proportional to strain and mathematically expressed as $\sigma_{ij} = C_{ijkl}\epsilon_{kl}$. Here σ_{ij} is the stress and ϵ_{kl} is the strain and C_{ijkl} is the stiffness constant, $i, j, k,$ and l represents the Cartesian directions $x, y,$ and z. C_{ijkl} is a 4^{th} rank tensor and has 81 elements but due to the symmetry in stress ($C_{ijkl} = C_{jikl}$) and symmetry in strain ($C_{ijkl} = C_{ijlk}$) it reduces to 36 elements which further reduces to 21 due to the equivalence of the partial derivative ($C_{ijkl} = \frac{\partial^2 E}{\partial\epsilon_{kl}\partial\epsilon_{ij}} = \frac{\partial^2 E}{\partial\epsilon_{ij}\partial\epsilon_{kl}} = C_{klij}$). Due to the symmetry in the crystal system, the independent components of the stiffness tensor even further reduce from 21 to 3 for cubic, 9 for orthorhombic and 6 for tetragonal-(I) crystal system. To calculate the elastic and mechanical properties for different MAPI structures we need to calculate all the independent components of the stiffness tensor first. There are two different methodology by which this can be done: (a) by calulating the stress tensors directly using quantum ESPRESSO code for different applied strains and using a linear fit, (b) by calculating the change in energy density of the system for

applied strains and doing a quadratic fit. We have done both and give a comparison of result in our result and discussion section. For the purpose of this work we used the second method, (change in energy density) as most of the previously published paper have reported their calculated values of elastic properties using this method.

The Taylor expansion of total internal energy E of a crystal can be written as

$$E(V,\epsilon) = E(V_0) + V_0\Big(\sum_i \frac{\partial E}{\partial \epsilon_i}\epsilon_i + \frac{1}{2}\sum_{i,j}\frac{\partial^2 E}{\partial \epsilon_i \partial \epsilon_j}\epsilon_i\epsilon_j\Big) + \mathcal{O}(\epsilon^3) \quad (5.1)$$

Here V_0 and V denotes the volume of the unstained and strained crystal respectively. ϵ_i is the strain in the i^{th} direction. $\frac{\partial^2 E}{\partial \epsilon_i \partial \epsilon_j}$ is also known as stiffness constant C_{ij} of the crystal. The change in energy density can be expressed as $U = \frac{E(V,\epsilon)-E(V_0)}{V_0}$. The idea behind calculating C_{ij} coefficients is that we will strain the structure in some specific directions and calculate the change in energy density. From the quadratic fitting of the change in energy density vs ϵ graph we can calculate the stiffness constant. The values for i and j ranges between 1 to 6 where indices defined as: $1 \equiv xx, 2 \equiv yy, 3 \equiv zz, 4 \equiv yz, 5 \equiv zx, 6 \equiv xy$ in Voigt notation.

How to Strain the Crystal: Strain Tensors

Every crystal structure has its own lattice parameters (i.e. lattice vectors $\vec{a} = a_x\hat{i} + a_y\hat{j} + a_z\hat{k}$, $\vec{b} = b_x\hat{i} + b_y\hat{j} + b_z\hat{k}$, and $\vec{c} = c_x\hat{i} + c_y\hat{j} + c_z\hat{k}$) and all the atoms in the unit cell can be expressed in the coordinates of the crystal lattice vectors. So, any strain to the lattice vectors automatically applies to the entire system including the atoms. The way we applied strain to the structure is given in the equation below. Different strain tensors used for the calculation are given in figure (5.1).

$$\begin{pmatrix} \epsilon_{xx} & \epsilon_{xy} & \epsilon_{xz} \\ \epsilon_{yx} & \epsilon_{yy} & \epsilon_{yz} \\ \epsilon_{zx} & \epsilon_{zy} & \epsilon_{zz} \end{pmatrix} \begin{pmatrix} a_x & b_x & c_x \\ a_y & b_y & c_y \\ a_z & b_z & c_z \end{pmatrix} = \begin{pmatrix} a'_x & b'_x & c'_x \\ a'_y & b'_y & c'_y \\ a'_z & b'_z & c'_z \end{pmatrix} \quad (5.2)$$

Calculation of different elastic parameters

After each structure is deformed using the strain tensor as discussed above, we need to relax the ions of these deformed structures keeping the lattice parameter fixed. This process is done using Quantum ESPRESSO. Each deformed, relaxed structure is

$$\begin{pmatrix} 1+\eta & 0 & 0 \\ 0 & 1 & 0 \\ 0 & 0 & 1 \end{pmatrix} \quad \begin{pmatrix} 1 & 0 & 0 \\ 0 & 1+\eta & 0 \\ 0 & 0 & 1 \end{pmatrix} \quad \begin{pmatrix} 1 & 0 & 0 \\ 0 & 1 & 0 \\ 0 & 0 & 1+\eta \end{pmatrix}$$

(a) (b) (c)

$$\begin{pmatrix} 1 & 0 & 0 \\ 0 & 1 & \eta/2 \\ 0 & \eta/2 & 1 \end{pmatrix} \quad \begin{pmatrix} 1 & 0 & \eta/2 \\ 0 & 1 & \\ \eta/2 & 0 & 1 \end{pmatrix} \quad \begin{pmatrix} 1 & \eta/2 & 0 \\ \eta/2 & 1 & 0 \\ 0 & 0 & 1 \end{pmatrix}$$

(e) (f) (g)

$$\begin{pmatrix} 1+\eta & 0 & 0 \\ 0 & 1-\eta & 0 \\ 0 & 0 & 1 \end{pmatrix} \quad \begin{pmatrix} 1+\eta & 0 & 0 \\ 0 & 1 & 0 \\ 0 & 0 & 1-\eta \end{pmatrix} \quad \begin{pmatrix} 1 & 0 & 0 \\ 0 & 1+\eta & 0 \\ 0 & 0 & 1-\eta \end{pmatrix}$$

(h) (i) (j)

Figure 5.1: Different strain tensors used to calculate the full stiffness tensor and other mechanical properties. Out of these nine strain tensors a,b and c represent uniaxial strain, e,f, and g represent shear strain and h, i, and j represent biaxial strain.

used to calculate total energy of the system. Once we have it, we can calculate the change in energy density (U) using equation (5.1) which in short can be written as

$$U = \frac{1}{2} \sum_{i=1}^{6} \sum_{j=1}^{6} C_{ij} \epsilon_i \epsilon_j \tag{5.3}$$

Using the 9 different strain tensors as mentioned in Figure (5.1) we can calculate 9 independent stiffness constants (C_{ij}) using equation (5.3). For C_{11}, C_{22}, and C_{33} we can use uniaxial strains as shown in figure 5.1(a, b, c) and directly use quadratic fitting to the equation. To calculate C_{44}, C_{55}, and C_{66} we need to apply shear strain as shown in figure 5.1(e, f, g). We purposefully used $\frac{\eta}{2}$ instead of η for the cross terms of ϵ because there will be 4 terms in the summation and it keeps the final equation simple as $U = \frac{1}{2} C_{ii} \eta^2$. For C_{12}, C_{13}, and C_{23} we need to apply biaxial strain as given in figure 5.1(h, i, j). Applying these strains will make the energy density equation as $U = \frac{1}{2}(C_{ii} + C_{jj} - 2C_{ij})\eta^2$, values of i, j are 1,2, and 3. Using the quadratic fitting and with previously calculated results of C_{ii} and C_{jj} we can calculate the values of C_{ij}. Once we calculate all the independent components of the stiffness tensor for orthorhombic and tetragonal MAPIs, we can calculate the compliance tensor which is nothing but the inverse of the stiffness matrix. Using the stiffness and compliance matrix we can calculate elastic properties

such as Young's modulus (E), bulk modulus (K), shear modulus (G), Poission's ratio (ν) using Voigt, Reuss, and Hill approximations[56] which give macroscopic averages for polycrystalline materials. All the corresponding formulas are mentioned below.

Voigt approximation:

$$K_V = \frac{1}{9}(C_{11} + C_{22} + C_{33}) + \frac{2}{9}(C_{12} + C_{13} + C_{23}) \tag{5.4}$$

$$G_V = \frac{1}{15}(C_{11} + C_{22} + C_{33} - C_{12} - C_{13} - C_{23}) + \frac{1}{5}(C_{44} + C_{55} + C_{66}) \tag{5.5}$$

$$\nu_V = \frac{3K_V - 2G_V}{6K_V + 2G_V} \tag{5.6}$$

$$E_V = \frac{9K_V G_V}{3K_V + G_V} \tag{5.7}$$

Reuss approximation:

$$K_R = \frac{1}{(S_{11} + S_{22} + S_{33}) + 2(S_{12} + S_{23} + S_{13})} \tag{5.8}$$

$$G_R = \frac{15}{4(S_{11} + S_{22} + S_{33}) - 4(S_{12} + S_{23} + S_{13}) + 3(S_{44} + S_{55} + S_{66})} \tag{5.9}$$

$$\nu_R = \frac{3K_R - 2G_R}{6K_R + 2G_R} \tag{5.10}$$

$$E_R = \frac{9K_R G_R}{3K_R + G_R} \tag{5.11}$$

Hill approximation:

$$G_H = \frac{1}{2}(G_V + G_R) \tag{5.12}$$

$$K_H = \frac{1}{2}(K_V + K_R) \tag{5.13}$$

$$E_H = \frac{9K_H G_H}{3K_H + G_H} \tag{5.14}$$

Universal anisotropic index[114]:

$$A^U = 5\frac{G_V}{G_R} + \frac{K_V}{K_R} - 6 \geq 0 \tag{5.15}$$

Calculation of elastic modulus at different crystallographic directions

To calculate Young's modulus (E) at any given direction [hkl], we can use the compliance matrix and equation 5.16[98] for orthorhombic structure. sometimes it can be seen as used with little mistake[118] where S_{11} is missing from the equation. For cubic symmetry, equation 5.16 will reduce to equation 5.17[58].

$$\frac{1}{E_{hkl}} = l_1^4 S_{11} + 2l_1^2 l_2^2 S_{12} + 2l_1^2 l_3^2 S_{13} + l_2^4 S_{22} + 2l_2^2 l_3^2 S_{23} + l_3^4 S_{33} + l_1^2 l_3^2 S_{44} + l_1^2 l_3^2 S_{55} + l_1^2 l_2^2 S_{66} \tag{5.16}$$

$$\frac{1}{E_{hkl}} = S_{11} - 2\left(S_{11} - S_{12} - \frac{1}{2}S_{44}\right)(l_1^2 l_2^2 + l_1^2 l_3^2 + l_2^2 l_3^2) \tag{5.17}$$

There is another way in which we do not need such formulas (eqn. 5.16, 5.17) for any particular crystal system instead we can use the stiffness matrix and transform it accordingly using some orthogonal transformation matrices as given in equation (5.18).

$$C^*_{ijkl} = \Omega_{ip}\Omega_{jq}\Omega_{kr}\Omega_{ls}C_{pqrs} \tag{5.18}$$

These orthogonal transformation matrices (Ω) can be simple rotation matrices. It is to keep in mind that this transformation rule applies to C_{pqrs} which is a $3\times3\times3\times3$ matrix but we have already made it a $C_{\alpha\beta}$ matrix which is a 6×6 matrix. So, this transformation rule is not directly applicable to our calculated stiffness tensor. The transformation law is derived in detail for $C_{\alpha\beta}$ in [140]. We have used the methodology given in this book to calculate rotated stiffness matrix. We constructed a general rotation matrix

$$\Omega = \begin{pmatrix} 1 & 0 & 0 \\ 0 & \cos\psi & -\sin\psi \\ 0 & \sin\psi & \cos\psi \end{pmatrix} \begin{pmatrix} \cos\beta & 0 & \sin\beta \\ 0 & 1 & 0 \\ -\sin\beta & 0 & \cos\beta \end{pmatrix} \begin{pmatrix} \cos\theta & -\sin\theta & 0 \\ \sin\theta & \cos\theta & 0 \\ 0 & 0 & 1 \end{pmatrix} \tag{5.19}$$

To transform the stiffness matrix we have done the below mathematical operation[140]

$$\mathbf{C}^* = \mathbf{K}\mathbf{C}\mathbf{K}^T \tag{5.20}$$

where

$$K = \begin{pmatrix} K_1 & 2K_2 \\ K_3 & K_4 \end{pmatrix} \tag{5.21}$$

$$K_1 = \begin{pmatrix} \Omega_{11}^2 & \Omega_{12}^2 & \Omega_{13}^2 \\ \Omega_{21}^2 & \Omega_{22}^2 & \Omega_{23}^2 \\ \Omega_{31}^2 & \Omega_{32}^2 & \Omega_{33}^2 \end{pmatrix} \tag{5.22}$$

$$K_2 = \begin{pmatrix} \Omega_{12}\Omega_{13} & \Omega_{13}\Omega_{11} & \Omega_{11}\Omega_{12} \\ \Omega_{22}\Omega_{23} & \Omega_{23}\Omega_{21} & \Omega_{21}\Omega_{22} \\ \Omega_{32}\Omega_{33} & \Omega_{33}\Omega_{31} & \Omega_{31}\Omega_{32} \end{pmatrix} \tag{5.23}$$

$$K_3 = \begin{pmatrix} \Omega_{21}\Omega_{31} & \Omega_{22}\Omega_{32} & \Omega_{23}\Omega_{33} \\ \Omega_{31}\Omega_{11} & \Omega_{32}\Omega_{12} & \Omega_{33}\Omega_{13} \\ \Omega_{11}\Omega_{21} & \Omega_{12}\Omega_{22} & \Omega_{13}\Omega_{23} \end{pmatrix} \tag{5.24}$$

$$K_4 = \begin{pmatrix} \Omega_{22}\Omega_{33} + \Omega_{23}\Omega_{32} & \Omega_{23}\Omega_{31} + \Omega_{21}\Omega_{33} & \Omega_{21}\Omega_{32} + \Omega_{22}\Omega_{31} \\ \Omega_{32}\Omega_{13} + \Omega_{33}\Omega_{12} & \Omega_{33}\Omega_{11} + \Omega_{31}\Omega_{13} & \Omega_{31}\Omega_{12} + \Omega_{32}\Omega_{11} \\ \Omega_{12}\Omega_{23} + \Omega_{13}\Omega_{22} & \Omega_{13}\Omega_{21} + \Omega_{11}\Omega_{23} & \Omega_{11}\Omega_{22} + \Omega_{12}\Omega_{21} \end{pmatrix} \tag{5.25}$$

Once we have the rotated stiffness tensor, we calculate the compliance matrix and thereby calculate the elastic modulus along the rotated crystallographic direction.

5.4 Results and Discussion

There are discrepancies in reports about calculated and measured mechanical properties as mentioned earlier in the introduction section. In the beginning of our investigation we have checked the difference in elastic properties calculated using two different methods: (a) by calculating the energy density and quadratic fit (b) by calculating the stress tensor and linear fit. PBE exchange correlation functional with ONCV pseudopotential is used for calculation of method comparison. The Brillouin zone is sampled using $5 \times 4 \times 5$ half-shifted Monkhorst-Pack grid with energy cutooff of 100 Ry for the wave functions. The methods are clearly explained in the theoretical framework. We have calculated the full stiffness tensors and the elastic modulus such as Young's modulus, bulk modulus, and shear modulus using Voigt-Reuss-Hill approximations for orthorhombic MAPI and the results are shown in Fig. (5.2). The calculation of stiffness constant C_{11} is given in Fig. (5.2(a,b)). The difference for all the 9 independent stiffness constant for orthorhombic MAPI is given in Fig. (5.2(c)). It can be seen that the calculated elastic parameters directly from the stress tensor are little higher for most of the

cases but the differences between two methods are much smaller than experimental error bar and theory discrepancies. So, the difference in calculation methodology for elastic properties calculation does not matter much. For the rest of our calculation, we have used the change in energy density method to compare with previously published results.

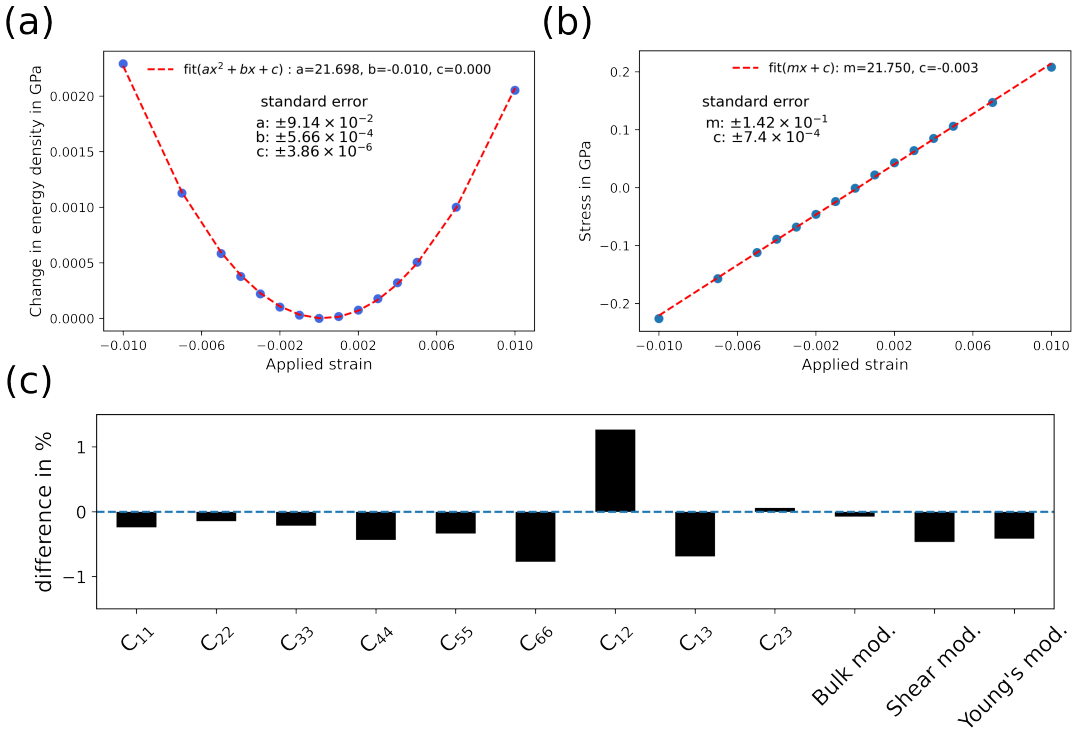

Figure 5.2: Elastic properties calculated for orthorhombic MAPI structure using two different methodologies. (a) Calculation of C_{11} using the change in energy density method. (b) Calculation of C_{11} using the full stress tensor method. (c) comparison of different parameters calculated using two different methods as mentioned in (a) and (b).

We have mentioned in our theoretical framework how to calculate Young's modulus at a particular crystallographic direction in two different ways. The reason we choose to transform the stiffness matrix first and then calculate the elastic modulus on the rotated stiffness matrix is that we do not need to know the exact formula for any particular crystal system. An incorrect assumption of cubic symmetry where the structure is not exactly cubic but a pseudo cubic (as we have seen in chapter 2), simplification of equation 5.16 to equation 5.17 will end up giving wrong result as can be seen in figure 5.3(a). We can get the compliance matrix from the transformed stiffness matrix

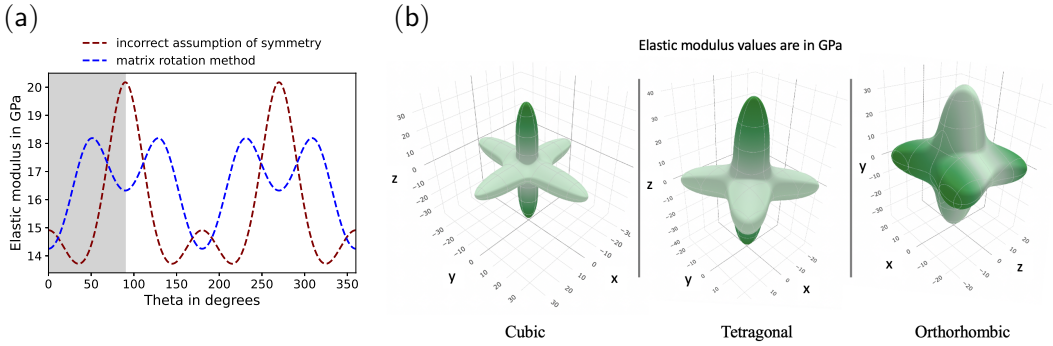

Figure 5.3: (a) Calculation of elastic modulus in (110) plane for orthorhombic MAPI using the general stiffness matrix rotation method and using formula for wrongly assumed symmetry of the structure. (b) 3D profile of the elastic modulus for cubic, tetragonal and orthorhombic MAPIs using ELATE.[37]

and calculate the elastic modulus just using general formula ($E_{11} = 1/S_{11}$) where E_{11} is the elastic modulus along the rotated x axis of the crystal system. This general method works for any system. It is even more helpful when we have an approximately symmetric structure rather than an exact one. Using the general method we also lower the chance of using wrong formula for the incorrect assumption of symmetry as in some works. We have calculated the elastic modulus profile in the (110) plane of orthorhombic MAPI using the general method and then used the general formula (Eqn. 5.16) but with cubic symmetry. The result can be seen in Fig. 5.3(a). The incorrect assumption of symmetry may lead to a very different, wrong result. One more thing to be noticed in this figure is that it is symmetric in 4 quadrants of the (110) plane and $0\text{-}90^0$ is enough to understand the elastic modulus profile in the plane. For rest of our results we have shown variation of elastic modulus data for this range only. Once we have the stiffness tensor for a system we can draw a 3D profile of the elastic modulus using ELATE[37]. It can be seen that the Young's modulus is higher parallel to the Pb-I-Pb bond and highest along the largest lattice parameter. Tetragonal MAPI has highest value of Young's modulus among the three phases.

To investigate different aspects of calculating elastic parameters we choose orthorhombic MAPI as it has exact symmetry (for theoretical calculation). The outcome is similar for cubic and tetragonal structures. The effect of different functionals and pseudopotentials on the orthorhombic MAPI structure and on its elastic modulus is shown in Fig.5.4(a). We can see that lattice parameters and Pb-I bond lengths are un-

derestimated by LDA and overestimated by PBE and the corresponding elastic modulus profile in (110) plane (Fig. 5.4a(ii)) shows the opposite which is expected. PBEsol stays in-between in both the cases. The exchange correlation functionals play a major role in calculating the correct structure. Bokdam et al. has done a detailed study based on RPA and find that strongly constrained and appropriately normed (SCAN) functional is the best for calculating correct structures for hybrid perovskites.[11] We have not studied SCAN functionals in this work but this can be good point to check in the future work. We also looked at effect of different pseudopotentials. We compared the results between

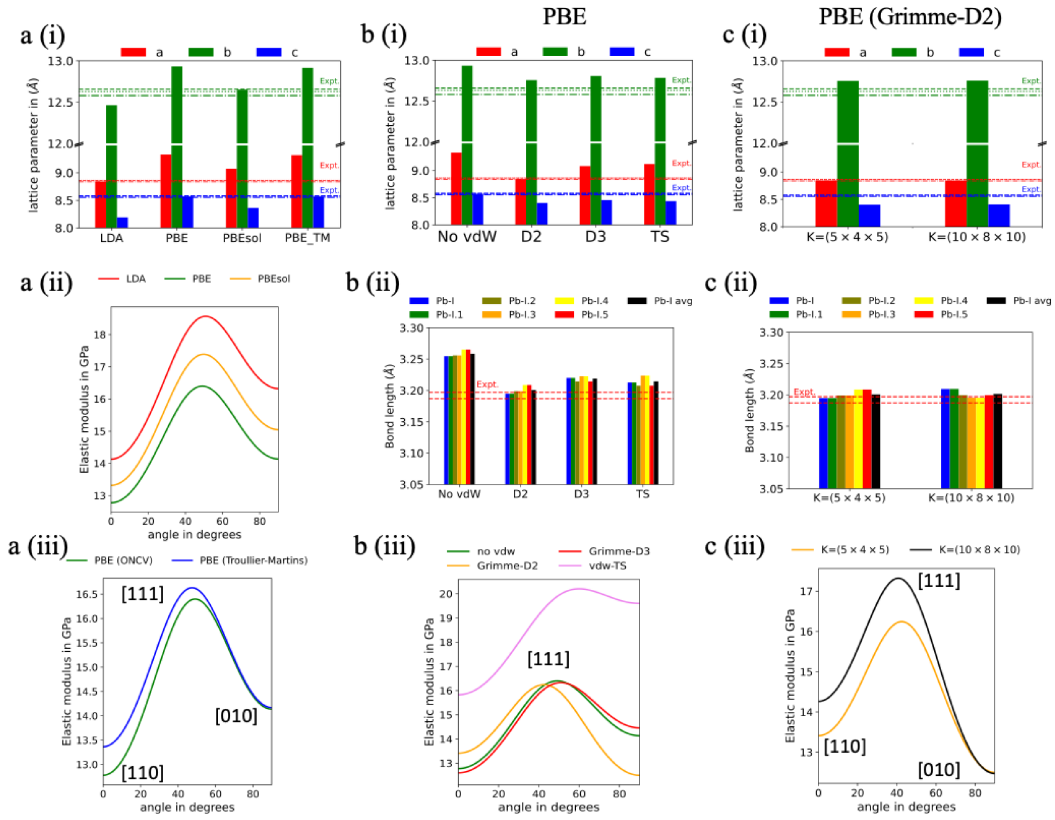

Figure 5.4: Effect of (a(i,ii)) different functionals , (a(iii)) pseudopotentials , (b) Van der Waals schemes, and (c) k-point sampling on structural parameters and elastic modulus for orthorhombic MAPI. The lines that compare the theoretical calculations with the experimental results are from [109, 6, 151]

ONCV (from pseudodojo[146]) and Troullier-Martin (from Quantum Espresso[45]). The result looks similar, only slight difference in the elastic properties but that can be under-

stood from their calculated structures which are slightly different too. (Fig. 5.4a(i,iii)). The effect of Van der Waals correction to the exchange correlation functional improve the structural parameters. It affects the elastic modulus mostly along [110] and [010] as shown in figure 5.4b(iii). The alignment of the MA^+ ion are in the (110) plane in the orthorhombic structure, this makes all the H atoms are out of this plane and along [110]. The interaction of the H atoms attached to the N of the MA^+ ion interacts more with the I of the Pb-I cage. This interaction affects most due to the Van der Waals correction. Among different available schemes of Van der Waals correction, Tkatchenko-Scheffler (TS) calculates the Young's modulus higher than average values. Grimme-D3 does not improve the elastic modulus much from the normal PBE one and Grimme-D2 affects most along the largest direction $< 010 >$ of the crystal. The many body dispersion (MBD) correction is by construction more accurate than pairwise Van der Waals interactions. This can be studied and checked as a future work. k-point sampling plays a crucial role in calculating elastic modulus at particular directions (Fig. 5.4c). We have seen that high k-point sampling ($10 \times 8 \times 10$) makes a difference around 1 GPa in elastic modulus along [110] and [111] directions and no change along [010]. Although high k-point sampling has significant effect in calculating elastic modulus at a particular direction, it does not have much effect on lattice parameters calculated using ($5 \times 4 \times 5$) k-point grid which is sufficient for converging the total energy by usual criteria. High k-point sampling also does not affect the poly crystalline averages of the elastic modulus (Fig. 5.5a). One hand, we know that PBE with Van der Waals correction (Grimme-D2) gives good result, but we need to have high k-point sampling along with high energy cutoff which needs more computation time, on the other hand if we use ultrasoft pseudopotential we can use lower energy cutoff values for planewave basis set. It will be useful to check the effect of ultrasoft pseudopotential on mechanical properties and to see if it can save some computation time without sacrificing the accuracy. In addition to that, some different methodology such as projector augmented wave (PAW) and all-electron methods should also be useful to check as they affects the mechanical properties of hybrid perovskites. The spin orbit coupling does not effect the structural parameter and hence expected not to make any difference in the calculation of elastic properties but it will be good to check that.

Our calculated results for both orthorhombic and tetragonal MAPI structures are summarized in figure 5.5. We can see that some of the reported elastic parameters

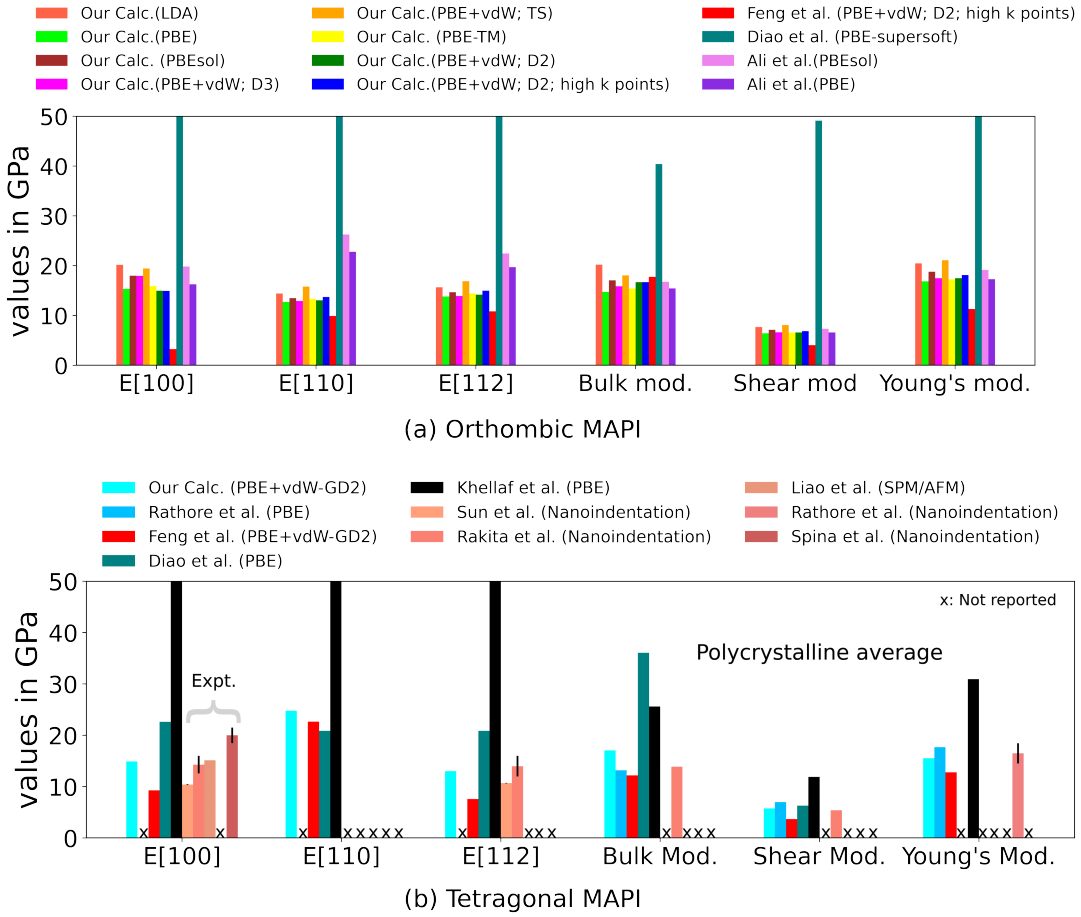

Figure 5.5: Comparison of our calculated elastic properties with the published theoretical results: Feng et al.[31], Diao et al.[24], Ali et al.[1], Khellaf et al.[65], and experimental results: Sun et al.[136], Rakita et al.[113], Liao et al.[79], Rathore et al.[117], Spina et al.[20]

are way higher than the rest of the values which may very well happen for wrong structure or wrong structural optimization. It can be seen that LDA overestimates and PBE underestimates all the elastic properties. PBEsol gives better values for elastic modulus but PBE with Grimme-D2 Van der Waals correction gives the best result. With high k-points elastic modulus improves in certain directions but it does not improve that much for the poly-crystalline averages. We can also see that no experimental results are available in case of orthorhombic structure to validate the result. Since PBE with Grimme-D2 vdw correction with high k-point works best, we used the same for tetragonal structure and validate our results with the experimentally available results (Figure

5.5(b)). Although, we used the same parameters as used by Feng et al., our results looks better in agreement with the experimental one.

5.5 Conclusion

Research about elastic properties of perovskites are very important for applications at large scale. It is strange that after a decade of perovskite research for solar cell applications we have very few reports available that studied the elastic properties of MAPIs and they too have discrepancies among their results. In this study we have done a detail analysis about different aspects of the theoretical calculation to understand the root cause of this discrepancy. We found that elastic properties are sensitive to the initial structure. Van der Waals correction to the exchange correctional functional plays a key role for orthorhombic and tetragonal structure. PBE with Grimme-D2 Van der Waals correction with high k-points works best for calculating elastic properties. One thing to note here is that use of high k-points does not affect the poly-crystalline averages that much but takes a lot of computational time. We have to keep in mind about the trade off between computation time and accuracy and high k-points should be used only in case of elastic modulus calculation at some specific direction.

5.6 Acknowledgement

Merced nAnomaterials Center for Energy and Sensing (MACES), a NASA-funded research and education center, under award NNH18ZHA008CMIROG6R. This work used computational resources from the Multi-Environment Computer for Exploration and Discovery (MERCED) cluster at UC Merced, funded by National Science Foundation Grant No. ACI-1429783, and the National Energy Research Scientific Computing Center (NERSC), a U.S. Department of Energy Office of Science User Facility operated under Contract No. DE-AC02-05CH11231.

Chapter 6

Summary and Outlook

Methylammonium lead iodide (MAPI) is the most studied material for next generation solar cell applications. A lot of research has been focused to improve its photo conversion efficiency (PCE), and stability. As part of my research, I studied local strain, symmetry and elastic properties of MAPI using density functional theory.

We have systematically studied the structural and vibrational properties of low temperature orthorhombic phase, room temperature tetragonal phase and high temperature cubic phase of $CH_3NH_3PbI_3$ under uniaxial strain. We identify those atomic interactions that are mostly responsible for frequency changes due to uniaxial strain by analyzing the dynamical matrix. Our perturbative analysis of the dynamical matrix with mode eigenvector explains the reason behind different frequency change patterns due to uniaxial strains. Our analysis about the change in the bond length and bond angles due to strain explains the behavior and stability of these phases under strain. Calculated mode-Grüneisen parameter and its thermodynamic average gives an idea of anharmonicity in each phase of this material. Our calculation identifies the best possible IR and Raman modes for all three phases which can serve as a guide for measuring local strain using experiment. This work opens the way for standard bench-top characterization method to be usable for analyzing the critical role of local strain in hybrid perovskite photovoltaics.

While studying the frequency shifts under uniaxial strain for the degenerate and close to degenerate modes of tetragonal and orthorhombic MAPIs we noticed that sometimes they cross each other which is confusing to resolve by just looking at the standard quantum ESPRESSO output. We have done a little modification of the code

that enables such calculations with much ease and without any confusion. This modified code can be helpful for any other phonon mode calculation under strain.

Among the three phases of MAPI perovskite, room temperature tetragonal phase is the most studied material for solar cell applications and yet the actual symmetry is well debated. In theoretical calculations there are possibility of different quasi symmetric structures (quasi-I4cm or quasi-I4/mcm). Since the structure is not exactly symmetric, its not possible to calculate the the irreducible representations for its vibrational modes. We developed a methodology using group theory that is able to prove the hidden symmetry in the teragonal MAPI structure and can be useful to calculate irreducible representations for any quasi symmetric material. This method can be helpful for spectroscopic study for other materials with approximate symmetry.

In last one decade, there has been a huge amount of research done to improve the photo conversion efficiency and stability of perovskite material for solar cell application but the mechanical properties which are crucial for commercial large scale applications, seems understudied. Among the very few reports that are available for mechanical properties of $CH_3NH_3PbI_3$, there are discrepancies among their results. Our detail theoretical calculation of elastic and mechanical properties of $CH_3NH_3PbI_3$ shed light on some specific problems that might have caused such discrepancies. It also gives calculated values of different elastic paramers that can be used as a benchmark for future theoretical and experimental research.

Bibliography

[1] Ali Ibrahim Omer A, Daniel P Joubert, and Mohammed SH Suleiman. A theoretical investigation of structural, mechanical, electronic and thermoelectric properties of orthorhombic $CH_3NH_3PbI_3$. *Eur. Phys. J. B*, 91(10):1–8, 2018.

[2] E Anastassakis, A Cantarero, and M Cardona. Piezo-raman measurements and anharmonic parameters in silicon and diamond. *Phys. Rev. B*, 41(11):7529, 1990.

[3] E Anastassakis, A Pinczuk, E Burstein, FH Pollak, and M Cardona. Effect of static uniaxial stress on the raman spectrum of silicon. *Solid State Commun.*, 88(11-12):1053–1058, 1993.

[4] Alla Arakcheeva, Dmitry Chernyshov, Massimo Spina, László Forró, and Endre Horváth. $CH_3NH_3PbI_3$: precise structural consequences of water absorption at ambient conditions. *Acta. Crystallogr. B. Struct. Sci. Cryst. Eng. Mater.*, 72(5):716–722, 2016.

[5] Nicholas Aristidou, Irene Sanchez-Molina, Thana Chotchuangchutchaval, Michael Brown, Luis Martinez, Thomas Rath, and Saif A Haque. The role of oxygen in the degradation of methylammonium lead trihalide perovskite photoactive layers. *Angew. Chem.*, 127(28):8326–8330, 2015.

[6] Tom Baikie, Yanan Fang, Jeannette M Kadro, Martin Schreyer, Fengxia Wei, Subodh G Mhaisalkar, Michael Graetzel, and Tim J White. Synthesis and crystal chemistry of the hybrid perovskite ($CH_3NH_3PbI_3$) for solid-state sensitised solar cell applications. *J. Mater. Chem. A*, 1(18):5628–5641, 2013.

[7] Colin D Bailie, M Greyson Christoforo, Jonathan P Mailoa, Andrea R Bowring, Eva L Unger, William H Nguyen, Julian Burschka, Norman Pellet, Jungwoo Z Lee, Michael Grätzel, et al. Semi-transparent perovskite solar cells for tandems with silicon and CIGS. *Energy Environ. Sci*, 8(3):956–963, 2015.

[8] S Baroni, A Dal Corso, S De Gironcoli, P Giannozzi, C Cavazzoni, G Ballabio, S Scandolo, G Chiarotti, P Focher, A Pasquarello, et al. Quantum espresso: open-source package for research in electronic structure, simulation, and optimization. *Code available from http://www. quantum-espresso. org*, 2005.

[9] Stefano Baroni, Stefano de Gironcoli, Andrea Dal Corso, and Paolo Giannozzi. Phonons and related crystal properties from density-functional perturbation theory. *Rev. Mod. Phys.*, 73:515–562, Jul 2001.

[10] Jonathon S Bechtel and Anton Van der Ven. Octahedral tilting instabilities in inorganic halide perovskites. *Phys. Rev. Mater.*, 2(2):025401, 2018.

[11] Menno Bokdam, Jonathan Lahnsteiner, Benjamin Ramberger, Tobias Schäfer, and Georg Kresse. Assessing density functionals using many body theory for hybrid perovskites. *Phys. Rev.lett.*, 119(14):145501, 2017.

[12] Nicola Bonini, Jivtesh Garg, and Nicola Marzari. Acoustic phonon lifetimes and thermal transport in free-standing and strained graphene. *Nano Lett.*, 12(6):2673–2678, 2012.

[13] Nicola Bonini, Michele Lazzeri, Nicola Marzari, and Francesco Mauri. Phonon anharmonicities in graphite and graphene. *Phys. Rev. Lett.*, 99(17):176802, 2007.

[14] Joachim Breternitz, Michael Tovar, and Susan Schorr. Twinning in $MAPbI_3$ at room temperature uncovered through laue neutron diffraction. *Sci. Rep.*, 10(1):1–8, 2020.

[15] Federico Brivio, Jarvist M Frost, Jonathan M Skelton, Adam J Jackson, Oliver J Weber, Mark T Weller, Alejandro R Goni, Aurélien MA Leguy, Piers RF Barnes, and Aron Walsh. Lattice dynamics and vibrational spectra of the orthorhombic, tetragonal, and cubic phases of methylammonium lead iodide. *Phys. Rev. B*, 92(14):144308, 2015.

[16] P Brüesch. Phonons: Theory and experiments II, of springer series in solid-state sciences vol. 65, chap. 2, 1986.

[17] Robert L Carter. Representations with imaginary characters: The doubling problem. *J. Chem. Educ.*, 70(1):17, 1993.

[18] Qiong Chen, Henan Liu, Hui-Seon Kim, Yucheng Liu, Mengjin Yang, Naili Yue, Gang Ren, Kai Zhu, Shengzhong Liu, Nam-Gyu Park, and Yong Zhang. Multiple-stage structure transformation of organic-inorganic hybrid perovskite $CH_3NH_3PbI_3$. *Phys. Rev. X*, 6:031042, 2016.

[19] Yimu Chen, Yusheng Lei, Yuheng Li, Yugang Yu, Jinze Cai, Ming-Hui Chiu, Rahul Rao, Yue Gu, Chunfeng Wang, Woojin Choi, et al. Strain engineering and epitaxial stabilization of halide perovskites. *Nature*, 577(7789):209–215, 2020.

[20] L Ćirić, K Ashby, T Abadie, M Spina, M Duchamp, B Náfrádi, M Kollár, L Forró, and E Horváth. Mechanical response of $CH_3NH_3PbI_3$ nanowires. *Appl. Phys. Lett.*, 112(11):111901, 2018.

[21] Bert Conings, Jeroen Drijkoningen, Nicolas Gauquelin, Aslihan Babayigit, Jan D'Haen, Lien D'Olieslaeger, Anitha Ethirajan, Jo Verbeeck, Jean Manca, Edoardo Mosconi, et al. Intrinsic thermal instability of methylammonium lead trihalide perovskite. *Adv. Energy Mater.*, 5(15):1500477, 2015.

[22] Ingrid De Wolf. Micro-raman spectroscopy to study local mechanical stress in silicon integrated circuits. *Semicond. Sci. Technol.*, 11(2):139, 1996.

[23] Volker L. Deringer, Ralf P. Stoffel, and Richard Dronskowski. Vibrational and thermodynamic properties of gese in the quasiharmonic approximation. *Phys. Rev. B*, 89:094303, Mar 2014.

[24] Xin-Feng Diao, Yan-lin Tang, Tian-yu Tang, Quan Xie, Kun Xiang, and Gao-fu Liu. Study on the stability of organic–inorganic perovskite solar cell materials based on first principle. *Mol. Phys.*, 118(8):e1665200, 2020.

[25] Mildred S Dresselhaus, Gene Dresselhaus, and Ado Jorio. Applications of group theory to the physics of solids, 2008.

[26] Giles E. Eperon, Tomas Leijtens, Kevin A. Bush, Rohit Prasanna, Thomas Green, Jacob Tse-Wei Wang, David P. McMeekin, George Volonakis, Rebecca L. Milot, Richard May, Axel Palmstrom, Daniel J. Slotcavage, Rebecca A. Belisle, Jay B. Patel, Elizabeth S. Parrott, Rebecca J. Sutton, Wen Ma, Farhad Moghadam, Bert Conings, Aslihan Babayigit, Hans-Gerd Boyen, Stacey Bent, Feliciano Giustino, Laura M. Herz, Michael B. Johnston, Michael D. McGehee, and Henry J. Snaith. Perovskite-perovskite tandem photovoltaics with optimized band gaps. *Science*, 354(6314):861–865, 2016.

[27] J. Even. Pedestrian guide to symmetry properties of the reference cubic structure of 3d all-inorganic and hybrid perovskites. *J. Phys. Chem. Lett.*, 6(12):2238–2242, Jun 2015.

[28] Douglas H Fabini, Ram Seshadri, and Mercouri G Kanatzidis. The underappreciated lone pair in halide perovskites underpins their unusual properties. *MRS Bulletin*, 45(6):467–477, 2020.

[29] Mahdi Faghihnasiri, Morteza Izadifard, and Mohammad Ebrahim Ghazi. DFT study of mechanical properties and stability of cubic methylammonium lead halide perovskites ($CH_3NH_3PbI_3$, X= I, Br, Cl). *J. Phys. Chem. C*, 121(48):27059–27070, 2017.

[30] Zhen Fan, Juanxiu Xiao, Kuan Sun, Lei Chen, Yating Hu, Jianyong Ouyang, Khuong P Ong, Kaiyang Zeng, and John Wang. Ferroelectricity of $CH_3NH_3PbI_3$ perovskite. *J. Phys. Chem. Lett.*, 6(7):1155–1161, 2015.

[31] Jing Feng. Mechanical properties of hybrid organic-inorganic $CH_3NH_3BX_3$ (B=Sn, Pb; X=Br, I) perovskites for solar cell absorbers. *APL Mater.*, 2(8):081801, 2014.

[32] Craig J. Fennie and Karin M. Rabe. Structural and dielectric properties of Sr_2TiO_4 from first principles. *Phys. Rev. B*, 68:184111, Nov 2003.

[33] Richard Phillips Feynman. Forces in molecules. *Phys. Rev.*, 56(4):340, 1939.

[34] Marina R. Filip, Carla Verdi, and Feliciano Giustino. Gw band structures and carrier effective masses of $CH_3NH_3PbI_3$ and hypothetical perovskites of the type $APbI_3$: A = NH_4, PH_4, AsH_4, and SbH_4. *J. Phys. Chem. C*, 119(45):25209–25219, 2015.

[35] Alexandra Franz, Daniel M Többens, and Susan Schorr. Interaction between cation orientation, octahedra tilting and hydrogen bonding in methylammonium lead triiodide. *Cryst. Res. Technol.*, 51(9):534–540, 2016.

[36] Kyle Frohna, Tejas Deshpande, John Harter, Wei Peng, Bradford A. Barker, Jeffrey B. Neaton, Steven G. Louie, Osman M. Bakr, David Hsieh, and Marco Bernardi. Inversion symmetry and bulk Rashba effect in methylammonium lead iodide perovskite single crystals. *Nat. Commun.*, 9(1):1829, 2018.

[37] Romain Gaillac, Pluton Pullumbi, and François-Xavier Coudert. Elate: an open-source online application for analysis and visualization of elastic tensors. *J. Condens. Matter Phys.*, 28(27):275201, 2016.

[38] S Ganesan, AA Maradudin, and J Oitmaa. A lattice theory of morphic effects in crystals of the diamond structure. *Ann. Physics*, 56(2):556–594, 1970.

[39] Wenxiu Gao, Yi Zhu, Yaojin Wang, Guoliang Yuan, and Jun-Ming Liu. A review of flexible perovskite oxide ferroelectric films and their application. *J Materiomics*, 6(1):1–16, 2020.

[40] Chunyu Ge, Mingyu Hu, Peng Wu, Qi Tan, Zhizhong Chen, Yiping Wang, Jian Shi, and Jing Feng. Ultralow thermal conductivity and ultrahigh thermal expansion of single-crystal organic–inorganic hybrid perovskite $CH_3NH_3PbX_3$ (X= Cl, Br, I). *J. Phys. Chem. C*, 122(28):15973–15978, 2018.

[41] Achim Gelessus, Walter Thiel, and Wolfgang Weber. Multipoles and symmetry. *J. Chem. Educ.*, 72(6):505, 1995.

[42] Wei Geng, Le Zhang, Yan-Ning Zhang, Woon-Ming Lau, and Li-Min Liu. First-principles study of lead iodide perovskite tetragonal and orthorhombic phases for photovoltaics. *J. Phys. Chem. C*, 118(34):19565–19571, 2014.

[43] Paolo Giannozzi, Oliviero Andreussi, Thomas Brumme, Oana Bunau, M Buongiorno Nardelli, Matteo Calandra, Roberto Car, Carlo Cavazzoni, Davide Ceresoli, Matteo Cococcioni, et al. Advanced capabilities for materials modelling with quantum espresso. *J. Phys. Condens. Matter.*, 29(46):465901, 2017.

[44] Paolo Giannozzi, Stefano Baroni, Nicola Bonini, Matteo Calandra, Roberto Car, Carlo Cavazzoni, Davide Ceresoli, Guido L Chiarotti, Matteo Cococcioni, Ismaila Dabo, Andrea Dal Corso, Stefano de Gironcoli, Stefano Fabris, Guido Fratesi, Ralph Gebauer, Uwe Gerstmann, Christos Gougoussis, Anton Kokalj, Michele Lazzeri, Layla Martin-Samos, Nicola Marzari, Francesco Mauri, Riccardo Mazzarello, Stefano Paolini, Alfredo Pasquarello, Lorenzo Paulatto, Carlo Sbraccia, Sandro Scandolo, Gabriele Sclauzero, Ari P Seitsonen, Alexander Smogunov, Paolo Umari, and Renata M Wentzcovitch. Quantum ESPRESSO: a modular and open-source software project for quantum simulations of materials. *J. Phys. Condens. Matter.*, 21(39):395502, sep 2009.

[45] Paolo Giannozzi, Stefano Baroni, Nicola Bonini, Matteo Calandra, Roberto Car, Carlo Cavazzoni, Davide Ceresoli, Guido L Chiarotti, Matteo Cococcioni, Ismaila

Dabo, et al. Quantum espresso: a modular and open-source software project for quantum simulations of materials. *J. Phys. Condens. Matter*, 21(39):395502, 2009.

[46] Giacomo Giorgi, Jun-ichi Ichi Fujisawa, Hiroshi Segawa, and Koichi Yamashita. Small photocarrier effective masses featuring ambipolar transport in methylammonium lead iodide perovskite: A density functional analysis. *J. Phys. Chem. Lett.*, 4(24):4213–4216, 2013.

[47] Feliciano Giustino. *Materials modelling using density functional theory: properties and predictions*. Oxford University Press, 2014.

[48] Tobias Glaser, Christian Müller, Michael Sendner, Christian Krekeler, Octavi E Semonin, Trevor D Hull, Omer Yaffe, Jonathan S Owen, Wolfgang Kowalsky, Annemarie Pucci, et al. Infrared spectroscopic study of vibrational modes in methylammonium lead halide perovskites. *J. Phys. Chem. Lett.*, 6(15):2913–2918, 2015.

[49] M. A. Green, A. Ho-Baillie, and H. J. Snaith. The emergence of perovskite solar cells. *Nat. Photon.*, 8:506–514, 2014.

[50] Stefan Grimme. Semiempirical GGA-type density functional constructed with a long-range dispersion correction. *J. Comput. Chem*, 27(15):1787–1799, 2006.

[51] Stefan Grimme, Jens Antony, Stephan Ehrlich, and Helge Krieg. A consistent and accurate ab initio parametrization of density functional dispersion correction (DFT-D) for the 94 elements H-Pu. *J. Chem. Phys*, 132(15):154104, 2010.

[52] Materials Design Group. Initial MAPI structures were taken from the wmd group. *https://github.com/WMD-group/hybrid-perovskites*, 2005.

[53] D. R. Hamann. Optimized norm-conserving vanderbilt pseudopotentials. *Phys. Rev. B*, 88:085117, Aug 2013.

[54] Daniel C Harris and Michael D Bertolucci. *Symmetry and spectroscopy: an introduction to vibrational and electronic spectroscopy*. Courier Corporation, 1989.

[55] Ralf Heiderhoff, Tobias Haeger, Neda Pourdavoud, Ting Hu, Mine Al-Khafaji, Andre Mayer, Yiwang Chen, Hella-Christin Scheer, and Thomas Riedl. Thermal conductivity of methylammonium lead halide perovskite single crystals and thin films: A comparative study. *J. Phys. Chem. C*, 121(51):28306–28311, 2017.

[56] Richard Hill. The elastic behaviour of a crystalline aggregate. *Proc. Phys. Soc. A*, 65(5):349, 1952.

[57] Pierre Hohenberg and Walter Kohn. Inhomogeneous electron gas. *Phys. Rev.*, 136(3B):B864, 1964.

[58] Matthew A Hopcroft, William D Nix, and Thomas W Kenny. What is the young's modulus of silicon? *J. Microelectromechanical Syst.*, 19(2):229–238, 2010.

[59] Jinsong Huang, Yongbo Yuan, Yuchuan Shao, and Yanfa Yan. Understanding the physical properties of hybrid perovskites for photovoltaic applications. *Nat. Rev. Mater.*, 2(7):17042, 2017.

[60] Ajay Kumar Jena, Ashish Kulkarni, and Tsutomu Miyasaka. Halide perovskite photovoltaics: background, status, and future prospects. *Chem. Rev.*, 119(5):3036–3103, 2019.

[61] Timothy W Jones, Anna Osherov, Mejd Alsari, Melany Sponseller, Benjamin C Duck, Young-Kwang Jung, Charles Settens, Farnaz Niroui, Roberto Brenes, Camelia V Stan, et al. Lattice strain causes non-radiative losses in halide perovskites. *Energy Environ. Sci*, 12(2):596–606, 2019.

[62] Pranav H Joshi, Liang Zhang, Istiaque M Hossain, Hisham A Abbas, Ranjith Kottokkaran, Satyapal P Nehra, Mahendra Dhaka, Max Noack, and Vikram L Dalal. The physics of photon induced degradation of perovskite solar cells. *AIP Advances*, 6(11):115114, 2016.

[63] Martin Kaltenbrunner, Getachew Adam, Eric Daniel Głowacki, Michael Drack, Reinhard Schwödiauer, Lucia Leonat, Dogukan Hazar Apaydin, Heiko Groiss, Markus Clark Scharber, Matthew Schuette White, et al. Flexible high power-per-weight perovskite solar cells with chromium oxide–metal contacts for improved stability in air. *Nat. Mater.*, 14(10):1032–1039, 2015.

[64] Byungkyun Kang and Koushik Biswas. Preferential $CH_3NH_3^+$ alignment and octahedral tilting affect charge localization in cubic phase $CH_3NH_3PbI_3$. *J. Phys. Chem. C*, 121(15):8319–8326, 2017.

[65] Abdallah Khellaf, Khellaf, and D'Silva. *Advances in Renewable Hydrogen and Other Sustainable Energy Carriers*. Springer, 2021.

[66] H. Kim, L. Zhao, J. S. Price, A. J. Grede, K. Roh, A. N. Brigeman, M. Lopez, B. P. Rand, and N. C. Giebink. Hybrid perovskite light-emitting diodes under intense electrical excitation. *Nat. Commun.*, 9:4893, 2018.

[67] Charles Kittel. *Introduction to solid state physics*. Wiley, 1953.

[68] RC Knechtli, RY Loo, and GS Kamath. High-efficiency gaas solar cells. *IEEE Trans. Electron Devices*, 31(5):577–588, 1984.

[69] Walter Kohn and Lu Jeu Sham. Self-consistent equations including exchange and correlation effects. *Phys. Rev.*, 140(4A):A1133, 1965.

[70] Akihiro Kojima, Kenjiro Teshima, Yasuo Shirai, and Tsutomu Miyasaka. Organometal halide perovskites as visible-light sensitizers for photovoltaic cells. *J. Am. Chem. Soc*, 131(17):6050–6051, May 2009.

[71] Michele Lazzeri and Francesco Mauri. First-principles calculation of vibrational Raman spectra in large systems: Signature of small rings in crystalline SiO_2. *Phys. Rev. Lett.*, 90(3):036401, 2003.

[72] Martin Ledinský, Philipp Löper, Bjoern Niesen, Jakub Holovský, Soo-Jin Moon, Jun-Ho Yum, Stefaan De Wolf, Antonín Fejfar, and Christophe Ballif. Raman spectroscopy of organic–inorganic halide perovskites. *J. Phys. Chem. Lett.*, 6(3):401–406, 2015.

[73] Jin-Wook Lee, Deok-Hwan Kim, Hui-Seon Kim, Seung-Woo Seo, Sung Min Cho, and Nam-Gyu Park. Formamidinium and cesium hybridization for photo-and moisture-stable perovskite solar cell. *Adv. Energy Mater.*, 5(20):1501310, 2015.

[74] YH Lee, LJ Cheng, PM Mooney, and JW Corbett. Solar cell high efficiency and radiation damage. In *NASA Conf. Publ*, volume 2020, page 179, 1977.

[75] Aurelien MA Leguy, Jarvist Moore Frost, Andrew P McMahon, Victoria Garcia Sakai, W Kockelmann, ChunHung Law, Xiaoe Li, Fabrizia Foglia, Aron Walsh, Brian C O'Regan, et al. The dynamics of methylammonium ions in hybrid organic–inorganic perovskite solar cells. *Nat. Commun.*, 6:7124, 2015.

[76] Aurélien MA Leguy, Alejandro R Goñi, Jarvist M Frost, Jonathan Skelton, Federico Brivio, Xabier Rodríguez-Martínez, Oliver J Weber, Anuradha Pallipurath, M Isabel Alonso, Mariano Campoy-Quiles, et al. Dynamic disorder, phonon lifetimes, and the assignment of modes to the vibrational spectra of methylammonium lead halide perovskites. *Phys. Chem. Chem. Phys.*, 18(39):27051–27066, 2016.

[77] Linn Leppert, Sebastian E Reyes-Lillo, and Jeffrey B Neaton. Electric field-and strain-induced Rashba effect in hybrid halide perovskites. *J. Phys. Chem. Lett.*, 7(18):3683–3689, 2016.

[78] Xiong Li, Manuel Tschumi, Hongwei Han, Saeed Salem Babkair, Raysah Ali Alzubaydi, Azhar Ahmad Ansari, Sami S Habib, Mohammad Khaja Nazeeruddin, Shaik M Zakeeruddin, and Michael Grätzel. Outdoor performance and stability under elevated temperatures and long-term light soaking of triple-layer mesoporous perovskite photovoltaics. *Energy Technol.*, 3(6):551–555, 2015.

[79] Wan-Ci Liao, Bernard Haochih Liu, and Ching-Chich Leu. Photodegradation pathways of $CH_3NH_3PbI_3$ organic perovskite polycrystalline film observed by in-situ scanning probe microscopy. *Appl. Surf. Sci.*, 545:149081, 2021.

[80] Qianqian Lin, Ardalan Armin, Ravi Chandra Raju Nagiri, Paul L Burn, and Paul Meredith. Electro-optics of perovskite solar cells. *Nat. Photon.*, 9(2):106, 2015.

[81] Dongjue Liu, Qiqi Lin, Zhigang Zang, Ming Wang, Peihua Wangyang, Xiaosheng Tang, Miao Zhou, and Wei Hu. Flexible all-inorganic perovskite $CsPbBr_3$ nonvolatile memory device. *ACS applied materials & interfaces*, 9(7):6171–6176, 2017.

[82] Mengyu Luan, Junling Song, Xiangfeng Wei, Fang Chen, and Jiehua Liu. Controllable growth of bulk cubic-phase $CH_3NH_3PbI_3$ single crystal with exciting room-temperature stability. *CrystEngComm*, 18:5257–5261, 2016.

[83] Bosai Lyu, Hongyuan Li, Lili Jiang, Wanfei Shan, Cheng Hu, Aolin Deng, Zhe Ying, Lele Wang, Yiran Zhang, Hans A Bechtel, et al. Phonon polariton-assisted infrared nanoimaging of local strain in hexagonal boron nitride. *Nano Lett.*, 19(3):1982–1989, 2019.

[84] K Matsuishi, T Ishihara, S Onari, YH Chang, and CH Park. Optical properties and structural phase transitions of lead-halide based inorganic–organic 3d and 2d perovskite semiconductors under high pressure. *Phys. Status Solidi B*, 241(14):3328–3333, 2004.

[85] Scott McKechnie, Jarvist M. Frost, Dimitar Pashov, Pooya Azarhoosh, Aron Walsh, and Mark Van Schilfgaarde. Dynamic symmetry breaking and spin splitting in metal halide perovskites. *Phys. Rev. B*, 98(8):085108, 2018.

[86] Lyndsey McMillon-Brown, Joseph M Luther, and Timothy J Peshek. What would it take to manufacture perovskite solar cells in space? *ACS Energy Lett.*, 7(3):1040–1042, 2022.

[87] Jeremiah McNatt. Nasa's photovoltaic energy research plans and programs. In *Interagency Advanced Power Group Renewable Energy Conversion Working Group Annual Meeting*, 2021.

[88] Lei Meng, Jingbi You, and Yang Yang. Addressing the stability issue of perovskite solar cells for commercial applications. *Nat. commun.*, 9(1):1–4, 2018.

[89] Félix Mouhat and François-Xavier Coudert. Necessary and sufficient elastic stability conditions in various crystal systems. *Phys. Rev. B*, 90(22):224104, 2014.

[90] N. Mounet. Structural, vibrational and thermodynamic properties of carbon allotropes from first-principles: diamond, graphite, and nanotubes. *Masters Thesis, MIT*, 2005.

[91] A Moussi, G Drolshagen, JAM McDonnell, J-C Mandeville, AT Kearsley, and H Ludwig. Hypervelocity impacts on hst solar arrays and the debris and meteoroids population. *Advances in Space Research*, 35(7):1243–1253, 2005.

[92] Kousuke Nakada, Yuki Matsumoto, Yukihiro Shimoi, Koji Yamada, and Yukio Furukawa. Temperature-dependent evolution of raman spectra of methylammonium lead halide perovskites, $CH_3NH_3PbI_3$ (X= I, Br). *Molecules*, 24(3):626, 2019.

[93] NASA. Building solar panels in space might be as easy as clicking print, link available at. *https://www.nasa.gov/feature/glenn/2019/building-solar-panels-in-space-might-be-as-easy-as-clicking-print*, 2020.

[94] Wanyi Nie, Jean-Christophe Blancon, Amanda J Neukirch, Kannatassen Appavoo, Hsinhan Tsai, Manish Chhowalla, Muhammad A Alam, Matthew Y Sfeir, Claudine Katan, Jacky Even, et al. Light-activated photocurrent degradation and self-healing in perovskite solar cells. *Nat. commun.*, 7(1):1–9, 2016.

[95] Katerina Nikolaidou, Som Sarang, Christine Hoffman, Benaz Mendewala, Hidetaka Ishihara, Jennifer Q Lu, Boaz Ilan, Vincent Tung, and Sayantani Ghosh. Hybrid perovskite thin films as highly efficient luminescent solar concentrators. *Adv. Opt. Mater.*, 4(12):2126–2132, 2016.

[96] Guangda Niu, Xudong Guo, and Liduo Wang. Review of recent progress in chemical stability of perovskite solar cells. *J. Mater. Chem. A*, 3(17):8970–8980, 2015.

[97] NREL. Best research-cell efficiency chart from national renewable energy laboratory. *https://www.nrel.gov/pv/assets/pdfs/cell-pv-eff-emergingpv-rev211214.pdf*, 2021.

[98] John Frederick Nye et al. *Physical properties of crystals: their representation by tensors and matrices*. Oxford university press, 1985.

[99] Khuong P Ong, Teck Wee Goh, Qiang Xu, and Alfred Huan. Structural evolution in methylammonium lead iodide $CH_3NH_3PbI_3$. *J. Phys. Chem. A*, 119(44):11033–11038, 2015.

[100] JH Parker Jr, DW Feldman, and M Ashkin. Raman scattering by silicon and germanium. *Phys. Rev.*, 155(3):712, 1967.

[101] J. P. Perdew and Alex Zunger. Self-interaction correction to density-functional approximations for many-electron systems. *Phys. Rev. B*, 23:5048–5079, 1981.

[102] John P Perdew, Kieron Burke, and Matthias Ernzerhof. Generalized gradient approximation made simple. *Phys. Rev. Lett*, 77(18):3865, 1996.

[103] John P. Perdew, Adrienn Ruzsinszky, Gábor I. Csonka, Oleg A. Vydrov, Gustavo E. Scuseria, Lucian A. Constantin, Xiaolan Zhou, and Kieron Burke. Restoring the density-gradient expansion for exchange in solids and surfaces. *Phys. Rev. Lett.*, 100:136406, Apr 2008.

[104] John P Perdew and Yue Wang. Accurate and simple analytic representation of the electron-gas correlation energy. *Phys. Rev. B*, 45(23):13244, 1992.

[105] Miguel A Pérez-Osorio, Qianqian Lin, Richard T Phillips, Rebecca L Milot, Laura M Herz, Michael B Johnston, and Feliciano Giustino. Raman spectrum of the organic–inorganic halide perovskite $CH_3NH_3PbI_3$ from first principles and high-resolution low-temperature raman measurements. *J. Phys. Chem. C*, 122(38):21703–21717, 2018.

[106] Miguel A Pérez-Osorio, Rebecca L Milot, Marina R Filip, Jay B Patel, Laura M Herz, Michael B Johnston, and Feliciano Giustino. Vibrational properties of the organic–inorganic halide perovskite $CH_3NH_3PbI_3$ from theory and experiment: factor group analysis, first-principles calculations, and low-temperature infrared spectra. *J. Phys. Chem. C*, 119(46):25703–25718, 2015.

[107] Yuan Ping and Jin Zhong Zhang. Spin-optotronic properties of organometal halide perovskites. *J. Phys. Chem. Lett.*, 9(20):6103–6111, 2018.

[108] Paul Pistor, Alejandro Ruiz, Andreu Cabot, and Victor Izquierdo-Roca. Advanced raman spectroscopy of methylammonium lead iodide: Development of a non-destructive characterisation methodology. *Sci. Rep.*, 6:35973, 2016.

[109] Albrecht Poglitsch and Daniel Weber. Dynamic disorder in methylammoniumtrihalogenoplumbates (ii) observed by millimeter-wave spectroscopy. *J. Chem. Phys*, 87(11):6373–6378, 1987.

[110] Rajendra Prasad. *Electronic structure of materials*. CRC Press, 2013.

[111] Jijun Qiu, Lance L McDowell, and Zhisheng Shi. Room-temperature cubic perovskite thin films by three-step all-vapor conversion from pbse to $MAPbI_3$. *Crystal Growth & Design*, 19(3):2001–2009, 2019.

[112] Claudio Quarti, Edoardo Mosconi, and Filippo De Angelis. Interplay of orientational order and electronic structure in methylammonium lead iodide: implications for solar cell operation. *Chem. Mater.*, 26(22):6557–6569, 2014.

[113] Yevgeny Rakita, Sidney R Cohen, Nir Klein Kedem, Gary Hodes, and David Cahen. Mechanical properties of $APbX_3$ (A= Cs or CH_3NH_3; X= I or Br) perovskite single crystals. *Mrs Communications*, 5(4):623–629, 2015.

[114] Shivakumar I Ranganathan and Martin Ostoja-Starzewski. Universal elastic anisotropy index. *Phys Rev. Lett.*, 101(5):055504, 2008.

[115] Rahul Rao, Ahmad E Islam, Simranjeet Singh, Rajiv Berry, Roland K Kawakami, Benji Maruyama, and Jyoti Katoch. Spectroscopic evaluation of charge-transfer doping and strain in graphene/MoS_2 heterostructures. *Phys. Rev. B*, 99(19):195401, 2019.

[116] Jörg Rappich, Felix Lang, Viktor V Brus, Oleksandra Shargaieva, Thomas Dittrich, and Norbert H Nickel. Light-induced defect generation in $CH_3NH_3PbI_3$ thin films and single crystals. *Solar RRL*, 4(2):1900216, 2020.

[117] Sudharm Rathore, Guifang Han, Anshuman Kumar, Wei Lin Leong, and Aparna Singh. Elastic modulus tailoring in $CH_3NH_3PbI_3$ perovskite system by the introduction of two dimensionality using (5-AVA) $2PbI_4$. *Solar Energy*, 224:27–34, 2021.

[118] P Ravindran, Lars Fast, P A_ Korzhavyi, B Johansson, J Wills, and Os Eriksson. Density functional theory for calculation of elastic properties of orthorhombic crystals: Application to $TiSi_2$. *J. Appl. Phys.*, 84(9):4891–4904, 1998.

[119] Md Roknuzzaman, Kostya Ken Ostrikov, Kimal Chandula Wasalathilake, Cheng Yan, Hongxia Wang, and Tuquabo Tesfamichael. Insight into lead-free organic-inorganic hybrid perovskites for photovoltaics and optoelectronics: A first-principles study. *Organic Electronics*, 59:99–106, 2018.

[120] Cristina Roldán-Carmona, Olga Malinkiewicz, Alejandra Soriano, Guillermo Mínguez Espallargas, Ana Garcia, Patrick Reinecke, Thomas Kroyer, M Ibrahim Dar, Mohammad Khaja Nazeeruddin, and Henk J Bolink. Flexible high efficiency perovskite solar cells. *Energy Environ. Sci*, 7(3):994–997, 2014.

[121] Nicholas Rolston, Kevin A Bush, Adam D Printz, Aryeh Gold-Parker, Yichuan Ding, Michael F Toney, Michael D McGehee, and Reinhold H Dauskardt. Engineering stress in perovskite solar cells to improve stability. *Adv. Energy Mater.*, 8(29):1802139, 2018.

[122] Som Sarang, Sara Bonabi Naghadeh, Binbin Luo, Parveen Kumar, Edwin Betady, Vincent Tung, Michael Scheibner, Jin Z Zhang, and Sayantani Ghosh. Stabilization of the cubic crystalline phase in organometal halide perovskite quantum dots via surface energy manipulation. *J. Phys. Chem. Lett.*, 8(21):5378–5384, 2017.

[123] Yuen-Ron Shen. *Principles of nonlinear optics*. Wiley-Interscience, New York, NY, USA, 1984.

[124] Rui Sheng, Anita Ho-Baillie, Shujuan Huang, Sheng Chen, Xiaoming Wen, Xiaojing Hao, and Martin A Green. Methylammonium lead bromide perovskite-based solar cells by vapor-assisted deposition. *J. Phys. Chem. C*, 119(7):3545–3549, 2015.

[125] Ali Sephar Shikoh and Alexander Polyakov. A quantitative analysis of the research trends in perovskite solar cells in 2009–2019. *Phys. Status Solidi A*, 217(23):2000441, 2020.

[126] Masaki Shirayama, Hideyuki Kadowaki, Tetsuhiko Miyadera, Takeshi Sugita, Masato Tamakoshi, Masato Kato, Takemasa Fujiseki, Daisuke Murata, Shota Hara, Takurou N. Murakami, Shohei Fujimoto, Masayuki Chikamatsu, and Hiroyuki Fujiwara. Optical transitions in hybrid perovskite solar cells: Ellipsometry, density functional theory, and quantum efficiency analyses for $CH_3NH_3PbI_3$. *Phys. Rev. Appl.*, 5(1):014012, 2016.

[127] Daniel J Slotcavage, Hemamala I Karunadasa, and Michael D McGehee. Light-induced phase segregation in halide-perovskite absorbers. *ACS Energy Lett.*, 1(6):1199–1205, 2016.

[128] KA Smith, EA Nowadnick, Shiyu Fan, Omar Khatib, Seong Joon Lim, Bin Gao, NC Harms, SN Neal, JK Kirkland, MC Martin, et al. Infrared nano-spectroscopy of ferroelastic domain walls in hybrid improper ferroelectric $Ca_3Ti_2O_7$. *Nat. Commun.*, 10(1):1–9, 2019.

[129] K Xerxes Steirer, Philip Schulz, Glenn Teeter, Vladan Stevanovic, Mengjin Yang, Kai Zhu, and Joseph J Berry. Defect tolerance in methylammonium lead triiodide perovskite. *ACS Energy Lett.*, 1(2):360–366, 2016.

[130] Harold T Stokes and Dorian M Hatch. Findsym: program for identifying the space-group symmetry of a crystal. *J. Appl. Crystallogr.*, 38(1):237–238, 2005.

[131] HT Stokes, DM Hatch, and BJ Campbell. Findsym. *ISOTROPY Software Suite, iso. byu. edu*, 2017.

[132] Constantinos C Stoumpos, Christos D Malliakas, and Mercouri G Kanatzidis. Semiconducting tin and lead iodide perovskites with organic cations: phase transitions, high mobilities, and near-infrared photoluminescent properties. *Inorg. Chem.*, 52(15):9019–9038, 2013.

[133] Samuel D. Stranks, Giles E. Eperon, Giulia Grancini, Christopher Menelaou, Marcelo J. P. Alcocer, Tomas Leijtens, Laura M. Herz, Annamaria Petrozza, and Henry J. Snaith. Electron-hole diffusion lengths exceeding 1 micrometer in an organometal trihalide perovskite absorber. *Science*, 342(6156):341–344, 2013.

[134] David A. Strubbe, Eric C. Johlin, Timothy R. Kirkpatrick, Tonio Buonassisi, and Jeffrey C. Grossman. Stress effects on the raman spectrum of an amorphous material: Theory and experiment on *a*-Si:H. *Phys. Rev. B*, 92:241202(R), 2015.

[135] Weitao Su, Naresh Kumar, Ning Dai, and Debdulal Roy. Nanoscale mapping of intrinsic defects in single-layer graphene using tip-enhanced raman spectroscopy. *Chem. Commun.*, 52(53):8227–8230, 2016.

[136] Shijing Sun, Yanan Fang, Gregor Kieslich, Tim J White, and Anthony K Cheetham. Mechanical properties of organic–inorganic halide perovskites, $CH_3NH_3PbX_3$ (X= I, Br and Cl), by nanoindentation. *J. Mater. Chem. A*, 3(36):18450–18455, 2015.

[137] Brandon R Sutherland and Edward H Sargent. Perovskite photonic sources. *Nat. Photon*, 10(5):295–302, 2016.

[138] Kuntal Talit and David A Strubbe. Stress effects on vibrational spectra of a cubic hybrid perovskite: A probe of local strain. *J. Phys. Chem. C*, 124(50):27287–27299, 2020.

[139] Zhi-Kuang Tan, Reza Saberi Moghaddam, May Ling Lai, Pablo Docampo, Ruben Higler, Felix Deschler, Michael Price, Aditya Sadhanala, Luis M Pazos, Dan Credgington, et al. Bright light-emitting diodes based on organometal halide perovskite. *Nat. Nanotechnol.*, 9(9):687–692, 2014.

[140] Thomas Chi-tsai Ting and Thomas Chi-tsai Ting. *Anisotropic elasticity: theory and applications*. Number 45. Oxford University Press on Demand, 1996.

[141] Alexandre Tkatchenko and Matthias Scheffler. Accurate molecular van der waals interactions from ground-state electron density and free-atom reference data. *Phys. rev. Lett.*, 102(7):073005, 2009.

[142] Norman Troullier and José Luís Martins. Efficient pseudopotentials for plane-wave calculations. *Phys. Rev. B*, 43(3):1993, 1991.

[143] Hsinhan Tsai, Reza Asadpour, Jean-Christophe Blancon, Constantinos C Stoumpos, Olivier Durand, Joseph W Strzalka, Bo Chen, Rafael Verduzco, Pulickel M Ajayan, Sergei Tretiak, et al. Light-induced lattice expansion leads to high-efficiency perovskite solar cells. *Science*, 360(6384):67–70, 2018.

[144] Yongguang Tu, Jiang Wu, Guoning Xu, Xiaoyu Yang, Rong Cai, Qihuang Gong, Rui Zhu, and Wei Huang. Perovskite solar cells for space applications: progress and challenges. *Adv. Mater.*, 33(21):2006545, 2021.

[145] Paolo Umari, Edoardo Mosconi, and Filippo De Angelis. Relativistic gw calculations on $CH_3NH_3PbI_3$ and $CH_3NH_3SnI_3$ perovskites for solar cell applications. *Sci. Rep.*, 4:4467, 2014.

[146] MJ Van Setten, Matteo Giantomassi, Eric Bousquet, Matthieu J Verstraete, Don R Hamann, Xavier Gonze, and G-M Rignanese. The pseudodojo: Training and

grading a 85 element optimized norm-conserving pseudopotential table. *Comput. Phys. Commun.*, 226:39–54, 2018.

[147] N. L. Vočadlo and Geoffrey D. Price. The Grüneisen parameter - computer calculations via lattice dynamics. *Phys. Earth Planet. Inter.*, 82(3-4):261–270, 1994.

[148] Jingying Wang, Chuang Zhang, Haoliang Liu, Ryan McLaughlin, Yaxin Zhai, Shai R Vardeny, Xiaojie Liu, Stephen McGill, Dmitry Semenov, Hangwen Guo, et al. Spin-optoelectronic devices based on hybrid organic-inorganic trihalide perovskites. *Nat. Commun.*, 10(1):1–6, 2019.

[149] Yun Wang, Tim Gould, John F Dobson, Haimin Zhang, Huagui Yang, Xiangdong Yao, and Huijun Zhao. Density functional theory analysis of structural and electronic properties of orthorhombic perovskite $CH_3NH_3PbI_3$. *Phys. Chem. Chem. Phys.*, 16(4):1424–1429, 2014.

[150] Christian Wehrenfennig, Giles E. Eperon, Michael B. Johnston, Henry J. Snaith, and Laura M. Herz. High charge carrier mobilities and lifetimes in organolead trihalide perovskites. *Adv. Mater.*, 26(10):1584–1589, Mar 2014.

[151] Mark T. Weller, Oliver J. Weber, Paul F. Henry, Antonietta M. Di Pumpo, and Thomas C. Hansen. Complete structure and cation orientation in the perovskite photovoltaic methylammonium lead iodide between 100 and 352 K. *Chem. Commun.*, 51(20):4180–4183, 2015.

[152] Lucy D Whalley, Jarvist M Frost, Young-Kwang Jung, and Aron Walsh. Perspective: Theory and simulation of hybrid halide perovskites. *J. Chem. Phys.*, 146(22):220901, 2017.

[153] C Wu, K Chen, DY Guo, SL Wang, and PG Li. Cations substitution tuning phase stability in hybrid perovskite single crystals by strain relaxation. *RSC Adv.*, 8(6):2900–2905, 2018.

[154] Wei Wu, Jin Wang, Peter Ercius, Nicomario C Wright, Danielle M Leppert-Simenauer, Robert A Burke, Madan Dubey, Avinash M Dogare, and Michael T Pettes. Giant mechano-optoelectronic effect in an atomically thin semiconductor. *Nano Lett.*, 18(4):2351–2357, 2018.

[155] Junjie Xie, Yan Liu, Jianjun Liu, Lei Lei, Qianqian Gao, Jiaqing Li, and Songwang Yang. Study on the correlations between the structure and photoelectric properties of $CH_3NH_3PbI_3$ perovskite light-harvesting material. *Journal of Power Sources*, 285:349–353, 2015.

[156] Guichuan Xing, Nripan Mathews, Shuangyong Sun, Swee Sien Lim, Yeng Ming Lam, Michael Grätzel, Subodh Mhaisalkar, and Tze Chien Sum. Long-range balanced electron- and hole-transport lengths in organic-inorganic $CH_3NH_3PbI_3$. *Science*, 342(6156):344–347, 2013.

[157] Ding-Jiang Xue, Yi Hou, Shun-Chang Liu, Mingyang Wei, Bin Chen, Ziru Huang, Zongbao Li, Bin Sun, Andrew H Proppe, Yitong Dong, et al. Regulating strain in

perovskite thin films through charge-transport layers. *Nat. Commun.*, 11(1):1–8, 2020.

[158] Dong Yang, Ruixia Yang, Shashank Priya, and Shengzhong (Frank) Liu. Recent advances in flexible perovskite solar cells: Fabrication and applications. *Angew. Chem. Int. Ed.*, 58(14):4466–4483, 2019.

[159] Jianming Yang, Qinye Bao, Liang Shen, and Liming Ding. Potential applications for perovskite solar cells in space. *Nano Energy*, 76:105019, 2020.

[160] Hua Zhang, Xianfeng Qiao, Yan Shen, Thomas Moehl, Shaik M Zakeeruddin, Michael Grätzel, and Mingkui Wang. Photovoltaic behaviour of lead methylammonium triiodide perovskite solar cells down to 80 K. *J. Mater. Chem. A*, 3(22):11762–11767, 2015.

[161] Le Zhang, Wei Geng, Chuan Jia Tong, Xueguang Chen, Tengfei Cao, and Mingyang Chen. Strain induced electronic structure variation in methyl-ammonium lead iodide perovskite. *Sci. Rep.*, 8(1):7760, 2018.

[162] Haiguang Zhao, Ruijia Sun, Zhaofen Wang, Kaifang Fu, Xun Hu, and Yuhai Zhang. Zero-dimensional perovskite nanocrystals for efficient luminescent solar concentrators. *Advanced Functional Materials*, 29(30):1902262, 2019.

[163] Jingjing Zhao, Yehao Deng, Haotong Wei, Xiaopeng Zheng, Zhenhua Yu, Yuchuan Shao, Jeffrey E Shield, and Jinsong Huang. Strained hybrid perovskite thin films and their impact on the intrinsic stability of perovskite solar cells. *Sci. Adv.*, 3(11):eaao5616, 2017.

[164] Cheng Zhu, Xiuxiu Niu, Yuhao Fu, Nengxu Li, Chen Hu, Yihua Chen, Xin He, Guangren Na, Pengfei Liu, Huachao Zai, et al. Strain engineering in perovskite solar cells and its impacts on carrier dynamics. *Nat. Commun.*, 10(1):1–11, 2019.

[165] Taishan Zhu and Elif Ertekin. Mixed phononic and non-phononic transport in hybrid lead halide perovskites: glass-crystal duality, dynamical disorder, and anharmonicity. *Energy & Environmental Science*, 12(1):216–229, 2019.